MECHANICAL PROPERTIES AND RADIATION TOLERANCE OF METALLIC MULTILAYERS

A Dissertation

by

NAN LI

Submitted to the Office of Graduate Studies of
Texas A&M University
in partial fulfillment of the requirements for the degree of

DOCTOR OF PHILOSOPHY

May 2010

Major Subject: Materials Science and Engineering

MECHANICAL PROPERTIES AND RADIATION TOLERANCE OF METALLIC MULTILAYERS

A Dissertation

by

NAN LI

Submitted to the Office of Graduate Studies of
Texas A&M University
in partial fulfillment of the requirements for the degree of

DOCTOR OF PHILOSOPHY

Approved by:

Chair of Committee,	Xinghang Zhang
Committee Members,	Haiyan Wang
	Lin Shao
	Karl T. Hartwig
Intercollegiate Faculty Chair,	Tahir Cagin

May 2010

Major Subject: Materials Science and Engineering

ABSTRACT

Mechanical Properties and Radiation Tolerance of Metallic Multilayers.

(May 2010)

Nan Li, B.E., Beijing University of Chemical Engineering;

M.E., Institute of Metal Research, Chinese Academy of Science

Chair of Advisory Committee: Dr. Xinghang Zhang

High energy neutron and proton radiation can induce serious damage in structural metals, including void swelling and embrittlement. Hence the design of advanced metallic materials with significantly enhanced radiation tolerance is critical for the application of advanced nuclear energy systems. The goals of this dissertation are to examine the fundamental physical mechanisms that determine the responses of certain metallic multilayers, with ultra-high density interface structures, to plastic deformation and high fluence He ion irradiation conditions. This dissertation focuses on the investigation of mechanical and radiation responses of Al/Nb and Fe/W multilayers. Radiation induced microstructural evolution in Cu and Cu/Mo multilayer films are briefly investigated for comparisons.

Al/Nb multilayer films were synthesized by magnetron sputtering at room temperature. The interface is of Kurdjumov-Sachs orientation relationship. I*n situ* nanoindentation inside a transmission electron microscope (TEM) reveal that interfaces act as strong barriers for dislocation transmission and dislocations climb along the Al/Nb

interfaces at a much higher velocity than in bulk. The evolution of microstructure and mechanical properties of Al/Nb multilayers has been investigated after helium ion irradiations: 100 keV He^+ ions with a dose of $6\times10^{16}/cm^2$. When layer thickness, h, is greater than 25 nm, hardness barely changes, whereas radiation hardening is more significant at smaller h. This study shows that miscible fcc/bcc interface with large positive heat of mixing is not stable during ion irradiation.

In parallel we investigate sputtered Fe/W multilayers. Film hardness increases with decreasing h, and approaches a maximum of 12.5 GPa when h = 1 nm. After radiation, radiation hardening is observed in specimens when $h \geq 5$ nm, however, hardness barely changes in irradiated Fe/W 1 nm specimens due to intermixing.

In comparison, Cu/Mo 5 nm multilayers with immiscible interface has also been investigated after helium ion irradiations. Interfaces exhibit significantly higher helium solubility than bulk. He/vacancy ratio affects the formation and distribution of He bubbles. The greater diameter of He bubbles in Cu than Mo originates from the ease of bubble growth in Cu via punching of interstitial loops.

Finally, helium bubble migration and growth mechanisms were investigated in irradiated Cu (100) single crystal films via in situ heating inside a TEM. The activation energy for bubble growth is ~ 0.02 eV at low temperature. At higher temperatures, the activation energy for bubble coalescence is ~ 0.22 eV inside crystal, and 0.34 eV close to surface. The migration mechanisms of helium bubbles involve continuous as well as Brownian movement.

DEDICATION

This dissertation is dedicated to:

My wife Qi Liu

ACKNOWLEDGEMENTS

First and foremost I would like to thank my advisor, Prof. Xinghang Zhang for providing this great research opportunity, consistent encouragement and financial support through the entire Ph.D. work that made this work possible. His insightful discussion, patience in explaining science, critical thinking, and direction of the project have been invaluable.

I would like to thank other members on the defense committee, Prof. Haiyan Wang, Prof. Lin Shao, and Prof. Karl Hartwig for their guidance and suggestions that helped shape this dissertation.

I am also grateful to Drs. Amit Misra, Jian Wang, Qiangmin Wei, Mike Nastasi, and Nathan Mara at Los Alamos National Laboratory and Jianyu Huang at Sandia National Laboratory for their valuable comments and encouragement. I would like to thank Dr. Zhiping Luo in Microscopy and Imaging Center at Texas A&M University for his tremendous support on microscopy experiments.

I would like to thank my colleagues and friends, O. Anderoglu, E.G. Fu, D. Foley, S. Rios, D. Bufford, B. Ham, K. Yu, C. Sun, Y. Liu, M. Martin, J.J. Carter, Z. Bi and J. Yoon. I appreciate their friendship and support during this period. The technical and administrative staffs in Department of Mechanical Engineering and at Texas A&M University deserve mention.

I would like to express my deepest gratitude to my parents and my wife, Qi Liu. Without their understanding and support, I would not make it through.

TABLE OF CONTENTS

CHAPTER Page

CHAPTER Page

CHAPTER Page

LIST OF FIGURES

FIGURE Page

FIGURE Page

FIGURE Page

FIGURE Page

FIGURE Page

FIGURE Page

FIGURE Page

FIGURE Page

FIGURE Page

FIGURE Page

FIGURE Page

LIST OF TABLES

CHAPTER I

INTRODUCTION

1.1 Applications of metallic multilayers

Internal interfaces in materials are extended defects including grain boundaries and interphase boundaries, found in almost all natural or artificially produced material. Because of the fundamental properties and their special use in wide range of technological applications, the development of multilayer films has been received intense interest for past few decades. The essence of the unique properties of multilayer films results from the layer thickness can be comparable to some certain characteristic length, such as the electron mean free path for electrical conductivity or the exchange interaction length for magnetic materials. By combining different types of components and layer thicknesses, multilayer films can obtain novel and unique mechanical, magnetic, thermal and optical properties, leading to their application in many fields of nanotechnology.

By composing magnetic and nonmagnetic metals, for example, multilayer films have revealed interesting giant magnetoresistance (GMR) effect resulting from the interplay between electron transport and magnetic behavior [1]. This leads to the

---

This dissertation follows the style of *Journal of Nuclear Materials*.

development of the data storage device industry. Ferroelectric multilayer films, typically consist of a layer of a ferroelectric perovskite such as SrBiTiO3 and a layer of electrode, which can be metallic (e.g., Pt), also have applications in nanoelectromechanical systems and optoelectronic devices [2]. Effects arising from repeating stacks of high-atomic-number and low-atomic-number elements such as La/B_4C or W/Si result in the formation of high-quality X-ray mirrors [3, 4]. The wavelength that is reflected by an X-ray mirror can be controlled by the layer thickness and the angle of the incident X-ray beam. The quality of the reflected X-rays is controlled by the number of repeats in the multilayer films.

Even in today's integrated-circuit engineering where several different materials are combined together, interfaces play a crucial role for the performance of these devices. Therefore, interface engineering is an important field of materials engineering. For many technological applications, the construction of internal interfaces, including the orientation relationship, the interfacial misfit dislocation, and interface kinetics, plays a crucial role. However, identifying interfaces offers a considerable challenge. This is caused by their complexity, which results from the large number of independent variables upon which the properties of interfaces depend. There are considerable difficulties already in the definition of what the structure of an interface is and how it depends on the independent variables.

Recently, the application of multilayer films in nuclear reactors is proposed [5]. Studies of strengthening effects and radiation tolerance enhancement of metallic multilayer films are the major subject of my thesis. Interface dominated materials can exhibit extraordinary mechanical properties, such as high yield stress and good ductility when the length scale associated with the interfaces approaches the ~ 100 nm regime [6, 7]. Particularly when the layer thickness decreases to a few nanometers, the maximum strength of metallic multilayer films can approach as high as the estimated theoretical strength limit of $E_c/30$, where E_c is Young's modulus [8, 9]. Extremely high strength achievable in multilayers with certain type of interface making multilayers very attractive for a variety of application, and their potential applications offer a continuous driving force to investigate the interface - dislocation interaction mechanism in these multilayers.

1.2 Interface dislocation configuration

The orientation relationship (OR) between two phases of different crystal structure is of special importance. The interface OR will directly affect the misfit dislocation network (density and separation etc) at the interface, which correspondingly determines the mechanical, magnetic, optical or some other properties. Take face centered cubic (FCC) / body centered cubic (BCC) interface as an example, if only low index poles or reflections are considered, there are four major types of interface: Kurdjumov-Sachs

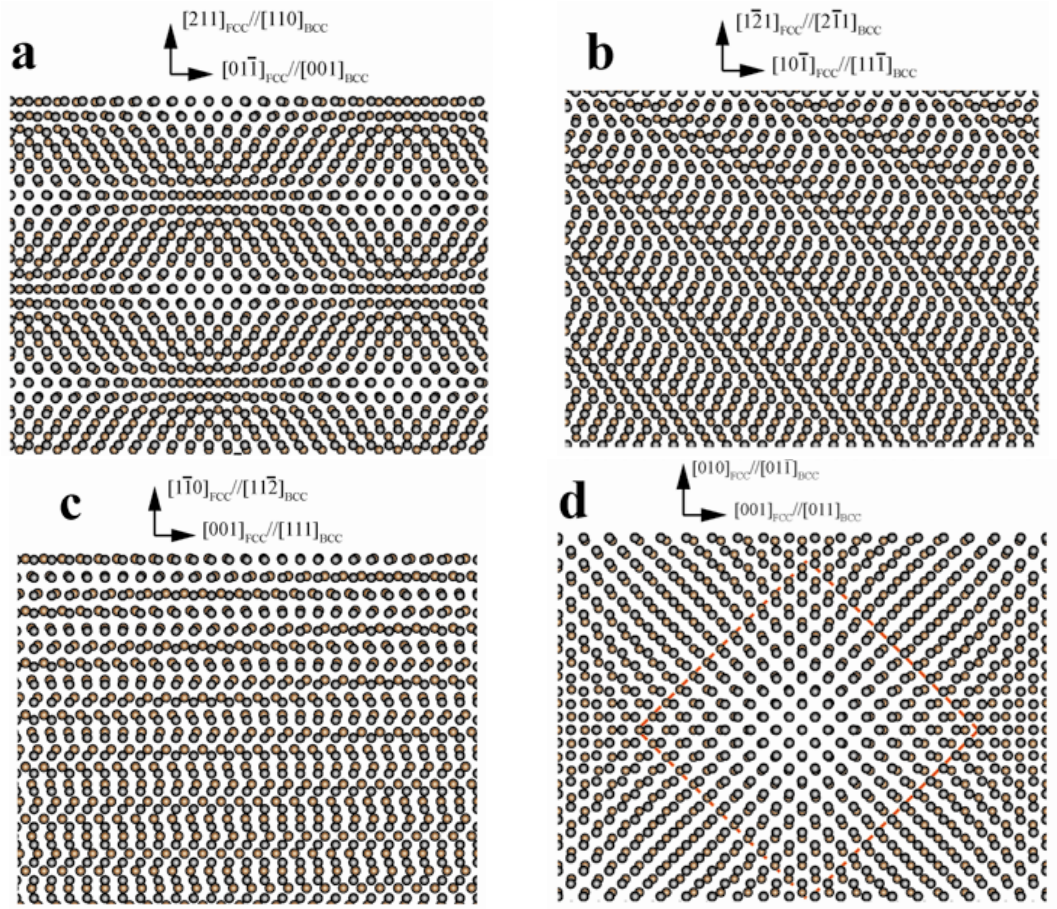

Figure 1.1 Schematic illustrations of relative positions of atoms looking normal to the interface plans for four type of interface OR. (a) N-W orientation [11, 12]. (b) K-S orientation [10], (c) Pitsch orientation [13], (d) Bain orientation [14]. (The grey atoms stand for fcc structured element atoms and the orange ones stands for bcc atoms.)

(K-S) [10], Nishiyama-Wassermann (N-W) [11, 12], Pitsch [13], and Bain [14] OR. The OR of these four types of interface is listed as follows and schematic illustrations of relative positions of atoms along the interface normal direction are shown in Fig. 1.1.

(a) N-W OR: {111} FCC || {110} BCC, <110> FCC || <100> BCC;

(b) K-S OR: {111} FCC || {110} BCC, <110> FCC || <111> BCC;

(c) Pitsch OR: {110} FCC || {110} BCC, <100> FCC || <111> BCC; and

(d) Bain OR: {100} FCC || {100} BCC, <100> FCC || <110> BCC.

Patches can be identified where the atoms from two layers are well aligned along the interface normal direction. MD simulation studies have shown that each patch is typically associated with one interface dislocation intersection [15, 16]. The difference of the patch configuration determines different interfacial dislocation configuration. Fig. 1.2 clearly shows the density of patches can increase when the increase of rotation angle.

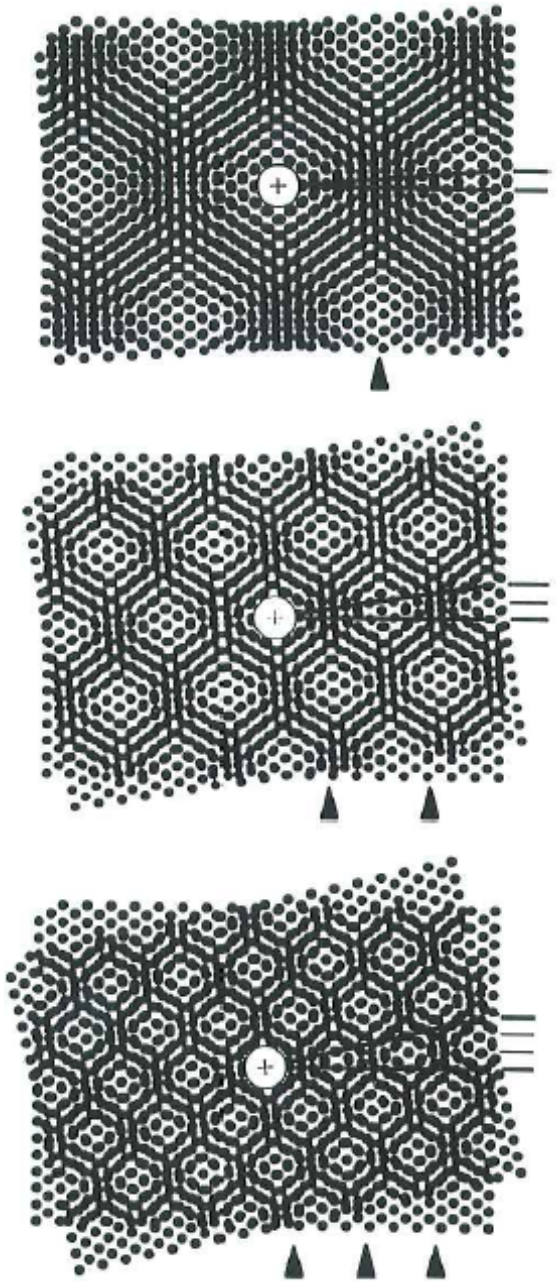

Figure 1.2 Schematic illustrations of relative positions of atoms looking normal to the interface plans with relatively different rotation angle. Patches can be identified where the atoms from two layers are well aligned along the interface normal direction. When the rotation angle increases, the patch density is increasing accordingly [17].

1.2.1 Interface dislocation net calculation

When the close-packed planes of FCC and BCC metals contact each other, K-S and/or N-W orientation relations are commonly observed. In Fig. 1.3, schematic configuration of the crystallography of K-S and N-W FCC / BCC interfaces are shown. In fact, the difference between these orientation relations is ~ 5.26 degrees by a rotation in the interface plane [15, 16].

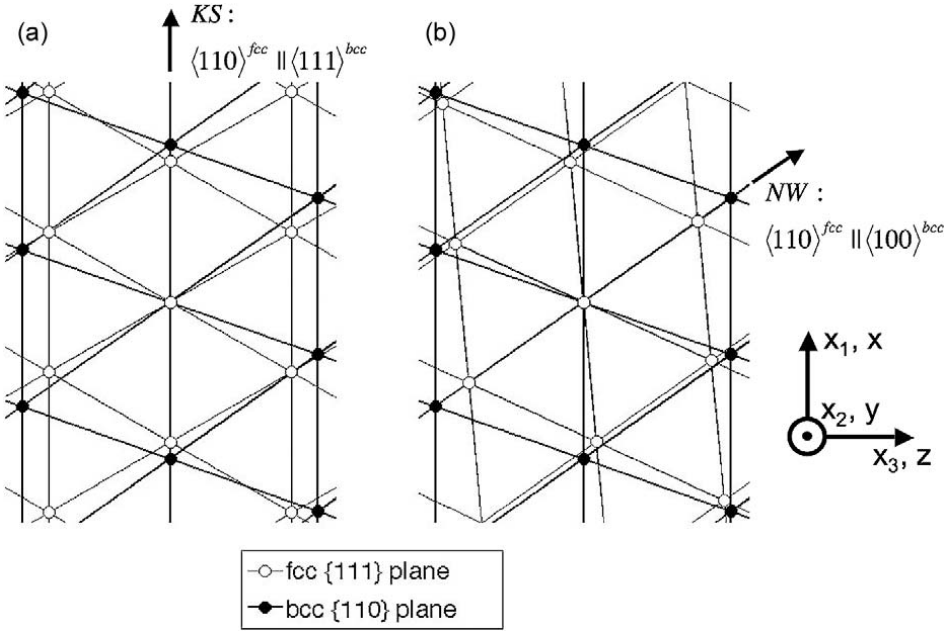

Figure 1.3 Schematic representation of two common orientation relations of interfaces between FCC {111} and BCC {110} close packed atomic planes: (a) Kurdjumov–Sachs, $<110>^{FCC}$ || $<111>^{BCC}$; (b) Nishiyama–Wassermann, $<110>^{FCC}$ || $<100>^{BCC}$. The difference between these orientation relations is about 5.26 degrees by a rotation in the interface plane [15].

Here we take Cu and Nb as an example to investigate the dislocation configuration in Cu-Nb K-S interface (a_{Cu}=3.615 Å, a_{Nb}=3.301 Å). If perfect Cu (111) is joined with Nb (110) in K-S orientation relation ($d_{Cu(111)}$ = 2.088 Å, $d_{Nb(110)}$ = 2.336 Å), the resulting interface before relaxation is shown in Fig. 1.4. A Moiré pattern of streaks of interface area where the locations of Cu and Nb atoms in the adjoining planes appear to line up can be discerned. The unit cell dimensions of the streaks is 1.34 × 2.55 nm and the area is 3.42 nm^2.

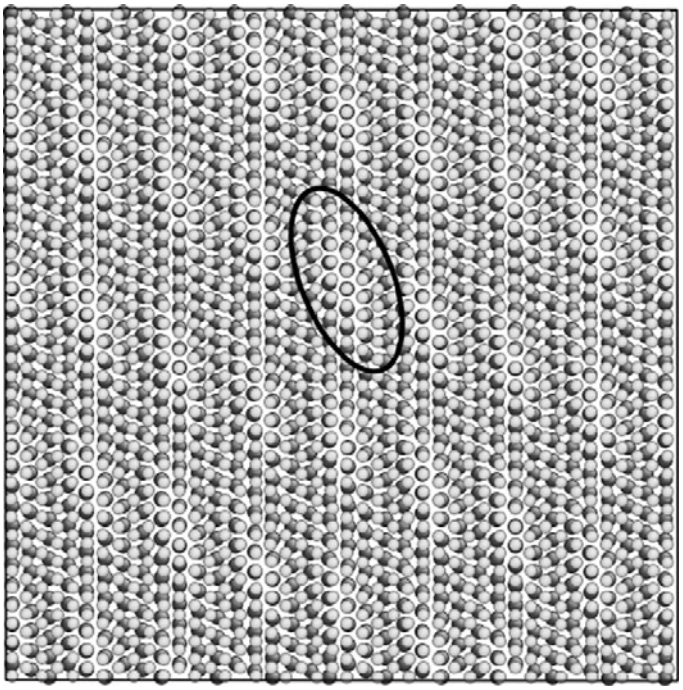

Figure 1.4 Visualization of the unrelaxed K-S interface between FCC Cu (light) and BCC Nb (dark) looking normal to the interface plane. Repetitive pattern is indicated by the black oval.

In reality Cu and Nb atoms at each side the interface will experience stress (tension or compression), which can be considered as homogeneous for simplicity. In order to build the construction of the homogeneous strain, α structure is proposed. Three <110> directions in the Cu {111} interface plane are labeled as $<110>_1^{Cu}$, $<110>_2^{Cu}$, $<110>_3^{Cu}$ in Fig. 1.5(a). In the Nb {110} interface plane, two possible <111> directions and one <100> direction are labeled as $<111>_1^{Nb}$, $<111>_2^{Nb}$, $<100>^{Nb}$. To strain the perfect Cu {111} interface plane into the α structure, a homogeneous in-plane deformation is applied. After deformation these rows satisfy the following conditions:

1. The direction of *A* rows is parallel to the direction of $<110>_1^{Cu}$
2. The direction of *C* rows is parallel to the direction of $<100>^{Nb}$
3. The distance *d(A)* between atoms along *A* rows is chosen such that the perpendicular spacing *s(C)* between *C* rows is equal to the perpendicular spacing $s(<100>^{Nb})$ between Nb $<100>^{Nb}$ rows;
4. The distance *d(C)* between atoms along *C* rows is chosen such that the perpendicular spacing *s(A)* between *A* rows is equal to the perpendicular spacing $s(<110>_1^{Cu})$ between Cu $<110>_1^{Cu}$ rows.

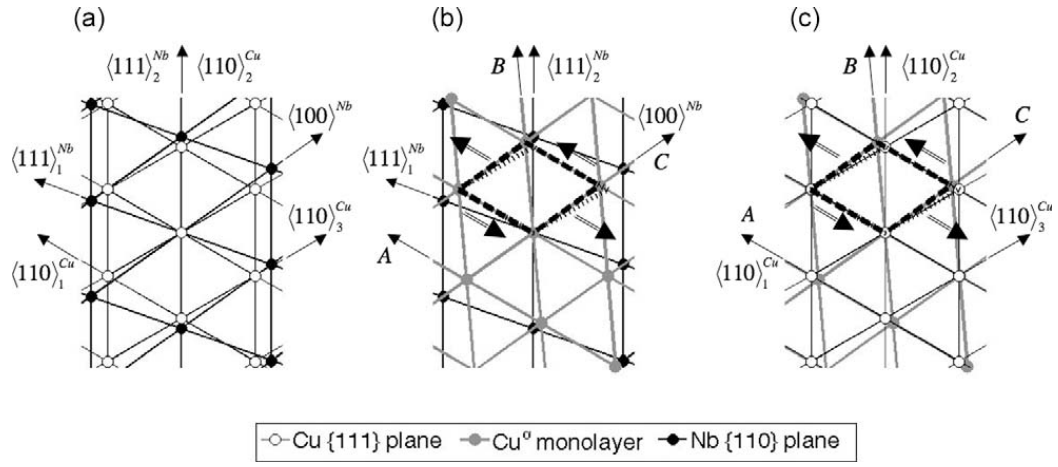

Figure 1.5 (a) The arrangement of Nb {110} and Cu {111} planes in the K-S orientation relation. (b) The arrangement of Nb {110} plane and Cu$^{\alpha}$ plane. (c) The arrangement of Cu$^{\alpha}$ plane and an unstrained Cu {111} plane. The strains that must be applied to create the Cu$^{\alpha}$ structure from a Cu {111} plane are illustrated by the dashed-line box and the thick arrows in (b) and (c) [16].

If α structure plane is seen as the interfacial layer, following method can be used to determine the interfacial dislocation configuration on the interfacial plane. Adopting the coordinate system in Fig. 1.5, one can express the nearest-neighbor vectors pointing along directions $<110>_1^{Cu}$ and $<110>_3^{Cu}$ in a perfect Cu {111} plane as

$$\vec{v}_{<110>_1^{Cu}} = \frac{\sqrt{2}}{2} a_{Cu}[\frac{1}{2}, \frac{-\sqrt{3}}{2}],$$
$$\vec{v}_{<110>_3^{Cu}} = \frac{\sqrt{2}}{2} a_{Cu}[\frac{1}{2}, \frac{\sqrt{3}}{2}], \qquad (1.1).$$

Therefore, the directions A and C in the Cu$^{\alpha}$ plane can be expressed as:

$$\vec{v}_A = \sqrt{30-12\sqrt{6}}\, a_{Nb}[\frac{1}{2}, \frac{-\sqrt{3}}{2}],$$
$$\vec{v}_C = \frac{3}{2}(\sqrt{6}-2) a_{Cu}[\sqrt{\frac{1}{3}}, \sqrt{\frac{2}{3}}], \qquad (1.2).$$

The displacement gradient $F_{Cu\to\alpha}$ that deforms one set of vectors $[\vec{v}^{T}_{<110>_1^{Cu}}\ \ \vec{v}^{T}_{<110>_3^{Cu}}]$ into the other $[\vec{v}_A^{T}\ \ \vec{v}_A^{T}]$ equals to

$$F_{Cu\to\alpha}=\begin{pmatrix} (3-\sqrt{6})\dfrac{a_{Cu}+a_{Nb}}{a_{Cu}} & (\sqrt{3}-\sqrt{2})\dfrac{a_{Cu}-a_{Nb}}{a_{Cu}} \\ [(\dfrac{6-2\sqrt{6}}{\sqrt{2}})+3(\dfrac{2-\sqrt{6}}{\sqrt{2}})\dfrac{a_{Nb}}{a_{Cu}}] & (\sqrt{6}-2)-(\sqrt{6}-3)\dfrac{a_{Nb}}{a_{Cu}} \end{pmatrix} \qquad (1.3).$$

The determinant of $F_{Cu\to\alpha}$ gives the change in interface area from a perfect Cu {111} plane to α structure, meanwhile it can be used to check the accuracy of the α structure. In our case, $\det(F_{Cu\to Cu^{\alpha}}) \approx 1.00538$, indicating the area density in the α structure is decreasing. The magnitudes of the uniform elongation and simple shear pictured in Fig. 1.5(b) and 1.5(c) are 0.538 and 11.6%, respectively [15, 16].

By using the Frank–Bilby formula [18], when an interface between crystals with lattices A and B, as shown in Fig. 1.6(a) and supposes that these lattices are related by homogeneous displacement gradients F^A and F^B to a common coherent reference lattice, shown in Fig. 1.6(b). Lattice A can be obtained by operating F^A on the reference lattice while lattice B can be obtained in the same way. Vector $\vec{p}$ is an arbitrary vector chosen in the plane of the interface between A and B. When mapped into the perfect reference configuration, this vector can take two different values from the A lattice and B lattice mapping respectively. Mapped from the A lattice, $\vec{p}$ takes on the value $F^{A\text{-}1}\vec{p}$, alternatively, if mapped from the B lattice, $\vec{p}$ takes on the value $F^{B-1}\vec{p}$. The Burgers

circuit in the configuration is shown in Fig. 1.6(a). The Burgers circuit in the reference configuration shown in Fig. 1.6(b) contains a closure failure $\vec{B}$, which can expressed as:

$$\vec{B} = (F^{A-1} - F^{B-1})\vec{p} \qquad (1.4).$$

Eq. (1.4) is known as the Frank–Bilby equation and computes the sum $\vec{B}$ of Burgers vectors of interfacial dislocations crossed by vector $\vec{p}$.

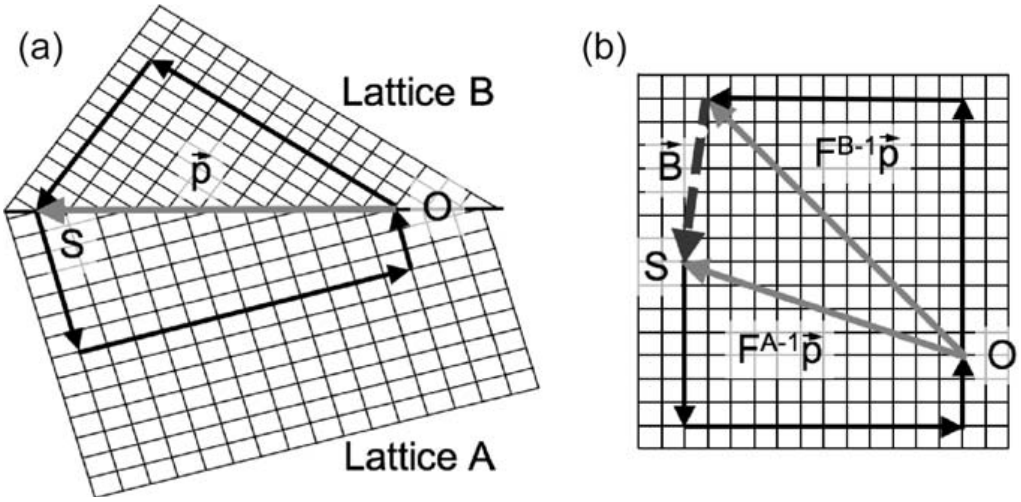

Figure 1.6 (a) A Burgers circuit constructed across the interface between lattice A and lattice B beginning at point S. Vector $\vec{p}$ is an arbitrary interface vector from the origin O terminating at S. (b) The Burgers circuit in (a) constructed in a coherent reference lattice. If lattice A is obtained from the reference lattice through a homogeneous deformation F^A and lattice B is similarly constructed using F^B, then the Burgers circuit has the closure failure $\vec{B} = (F^{A-1} - F^{B-1})\vec{p}$, dashed arrow [15, 18].

In the case of the Cu/Nb K-S interface, the α-geometry reference configuration as shown in Fig. 1.5 is used. The Burgers vector of interfacial dislocation can be described

as:

$$\vec{b} = (F_{Nb\to\alpha} - F_{Cu\to\alpha})\vec{p} \tag{1.5}$$

This expression can also be rewritten as

$$\vec{b} = (F_{Nb\to\alpha} - I)\vec{p} + (I - F_{Cu\to\alpha})\vec{p} \tag{1.6}$$

When the operator $I - F_{Cu\to\alpha}$ is diagonalized, two eigenvalues and eigenvectors will be yielded:

$$\begin{aligned} &\lambda_1 = 0, \quad \vec{\nu}_1 = [1, (\frac{\sqrt{2}a_{Cu} - \sqrt{3}a_{Nb}}{a_{Cu} - a_{Nb}})], \\ &\lambda_2 = 1 + 2(\sqrt{6} - 2)\frac{a_{Cu}}{a_{Nb}}, \quad \vec{\nu}_2 = [1, -\sqrt{3}]. \end{aligned} \tag{1.7}$$

The operator $I - F_{Cu\to Cu^{\alpha}}$ have one zero and one non-zero eigenvalue. It describes one set of parallel interfacial dislocations with line direction $\vec{\xi} = \vec{\nu}_1$, and Burgers vector direction parallels to $\vec{\nu}_2$. The relation between Burgers vector magnitude and dislocation spacing is described as $\lambda_2| = \frac{b}{s}\sqrt{1 - (\vec{\nu}_1 \cdot \vec{\nu}_2)^2}$, where s is the spacing distance. A comparison of the burgers vector directions $\vec{\nu}_2$ with $<110>_1^{Cu}$ and $<100>^{Nb}$ indicates that $\vec{\nu}_2$ is parallel to $<110>_1^{Cu}$. Therefore, the assumption that the Burgers vector magnitudes are equal to one nearest neighbor distance along these directions can be made, and the values of the dislocation spacing can be developed from the previous relation. In the similar way, another set of dislocations can be calculated. Configuration of two sets of interfacial dislocations at Cu/Nb interface is shown in Fig. 1.7.

However, since this method is based on a purely geometrical analysis of lattices A

and B, it cannot provide information which depends strongly on the nature of interatomic bond. For example, it cannot describe how the Burgers vector is partitioned among individual interfacial dislocations because of the low stacking fault energy. Thus, in FCC materials it does not distinguish between perfect $\frac{1}{2}<110>$ dislocations and ones that have dissociated into two Shockley partials. Also it cannot be used to compute dislocation core widths and so does not predict whether the dislocation is spread out over a wide area at the interface or not.

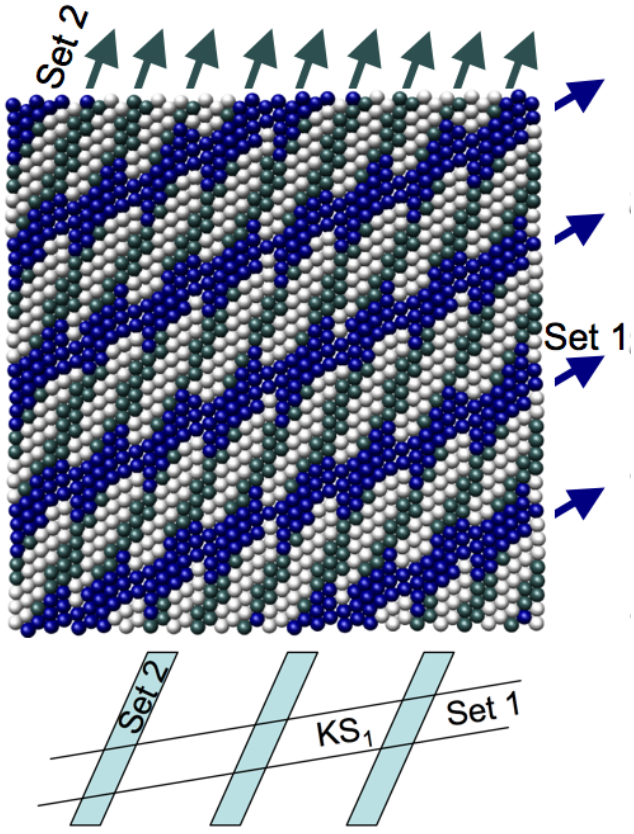

Figure 1.7 Two sets of misfit dislocations lie in the Cu-Nb plane in K-S orientation relation [19].

1.2.2 Dislocation reaction in dislocation net

When two sets of parallel dislocations cross with each other, the interactions should be considered to get the final stable dislocation configuration. The possible reactions depend upon the self-energy and interaction energies of the reacting dislocations, and also depend on both the crystal structure and the characteristics of the boundary. When the dislocation segment is formed, Eq. 1.8

$$\sum_i b_i^2[(1-\nu\cos^2\beta_i)\xi_i + 2\nu\cos\beta_i\sin\beta_i\frac{\xi_i\times(\xi_i\times b_i)}{|\xi_i\times b_i|}] = 0 \qquad (1.8),$$

can be applied to establishes the equilibrium angle in the plane of the boundary. Also, interaction forces can lead to "puckering" of the boundary, in which alternate nodes are displaced in opposite directions normal to the average boundary plane. For example, as shown in Fig. 1.8(a), the dislocation network has a lozenge shaped mesh if there is no interaction. However, reactions between crossing dislocations can change the dislocation net to hexagonal mesh (Fig. 1.8(b)). An actual example of a hexagonal mesh in Fe boundary is shown in Fig. 1.9.

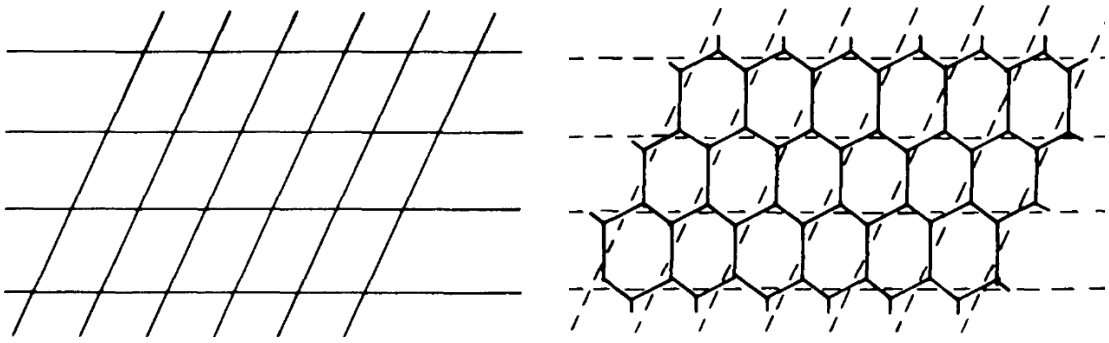

Figure 1.8 (a) Lozenge-shaped dislocation nets and (b) Hexagonal shaped dislocation nets when interaction happens [18].

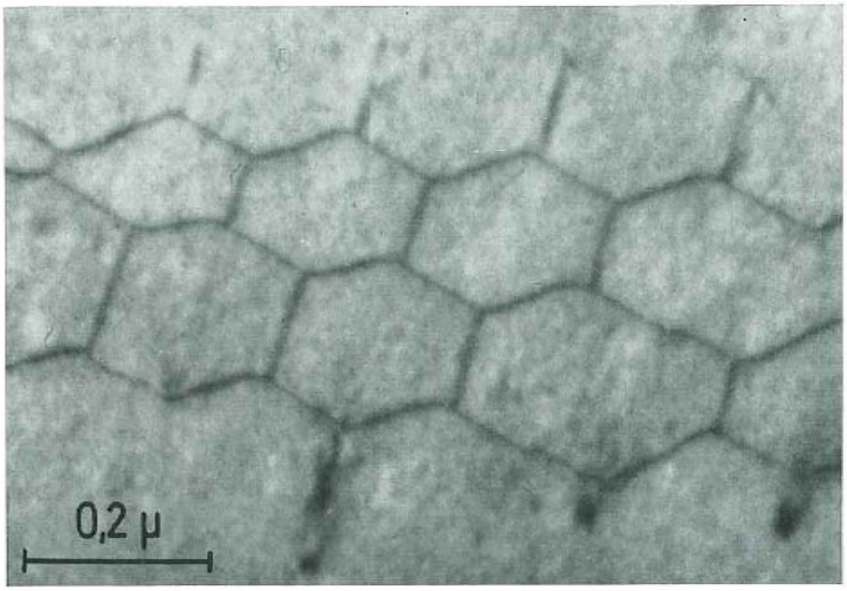

Figure 1.9 Hexagonal dislocation network in iron [17].

1.3 Mechanical properties of metallic multilayers

A variety of metallic multilayer systems have been explored in an attempt to understand the impact of interfaces on the strength of these multilayers. These include FCC / FCC type interface, such as Cu/Ni, Cu/Ag, Cu/330 austenitic stainless steel, etc.

[20 - 22]; FCC/BCC type, such as Cu/Nb, Cu/Cr, Cu/W, Fe/Pt [20, 23, 24]; and BCC/BCC type, such as Fe/Cr [24]. In comparison to the rule-of-mixture estimation of the composites by using the strengths of the individual constituent, the strength of these nanostructured multilayers is much higher [25 - 27]. Table 1 lists some mechanical properties of these metallic multilayers. Some general conclusions can be inferred from the table:

1. The maximum strength is typically achieved at an individual layer thickness of 2 - 5 nm.
2. The maximum strength is typically within a factor of 2 - 3 of the theoretical strength limit (~ E/40).
3. For a given type of material systems, e.g., polycrystalline FCC-FCC such as Ag-Cu, Al-Cu and Cu-Ni, the H-P slope increases as E_{hard} (or E_c) increases for approximately the same E_{hard}/E_{soft} ratio. Similar trend is observed in polycrystalline FCC-BCC systems (Cu-Nb, Cu-Cr and Pt-Fe).
4. For a given system (e.g., Pt-Fe and Cu-Ni), the single crystalline multilayer with cube-on-cube orientation relationship shows a lower H-P slope as compared to the polycrystalline multilayer. This indicates that grain boundaries within a layer also contribute to the H-P slope.

Table 1.1 Some mechanical properties of some metallic multilayer films

Multilayer system	σ_{max} (GPa)	h (nm) atσ_{max}	σ_{max} as a fraction of E_c	H-P slope (Mpa·m$^{-1/2}$)	E_{hard}/E_{soft}	E_{hard} (GPa)	Reference
FCC-FCC							
Cu-Ni (sc)	1.63	5	$E_c/100$	0.08	1.5	200	[20]
Cu-Ag	0.65	46	$E_c/130$	0.11	1.6	102	[28]
Cu-Al	0.78	20~70	$E_c/130$	0.13	1.5	104	[29]
Au-Ni	2.1	1~2	$E_c/70$	NA	2.5	200	[30]
Ag-Ni	2.08	5	$E_c/70$	NA	1.6	200	[27]
FCC-BCC							
Ag-Cr (sc)	1.63	2.5	$E_c/100$	NA	3	300	[26]
Cu-Nb	2.13	2.5	$E_c/60$	0.16	1.08	110	[20]
Cu-Cr	2.33	2.5~10	$E_c/80$	0.32	1.9	230	[20]
Fe-Pt	6	3.5	$E_c/35$	0.44	1.1	260	[26]
Fe-Pt (sc)	3.2	2	$E_c/65$	0.23	1.1	260	[26]
BCC-BCC							
Fe-Cr (sc)	2.8	2	$E_c/80$	NA	1.05	275	[26]

* σ_{max} is the maximum yield strength achieved in the given system, sc (single crystal), NA (not available), E_c is multilayer Young's modulus, E_{hard} is the Young's modulus of the hard phase, and E_{soft} is the Young's modulus of the soft phase.

Fig. 1.10 shows the indentation hardness (H) of some Cu-based multilayers changing with layer thickness, h. When h is large, ~ 100 nm, the value of H increases linearly to $h^{-1/2}$, which is consistent with the Hall-Petch model. However, when h decrease to a length scale of a few tens of nanometers, the Hall-Petch model "breaks down", i.e., no longer applicable in this regime, but the strength still continues to increase with decreasing layer thickness. The hardness of multilayer films reaches peak value when h is reduced to a few nanometers [26, 31, 32].

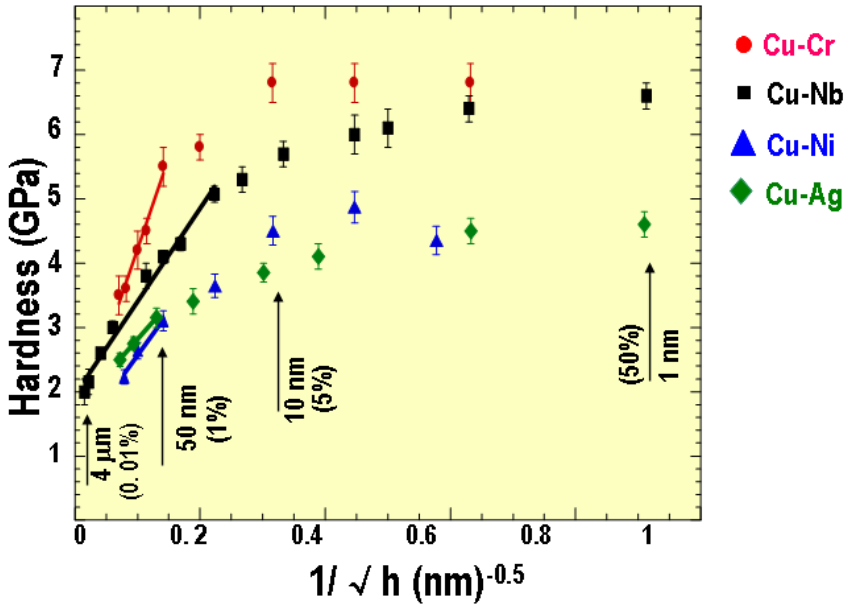

Figure 1.10 The dependence of hardness on layer thickness (h) for Cu-Cr, Cu-Nb, Cu-Ni and Cu-Ag multilayers. Linear fit at larger h is consistent with the Hall-Petch model. At lower h, the Hall-Petch model breaks down [9].

As illustrated schematically in Fig. 1.11, major deformation mechanisms in these multilayered materials depend on the layer thickness, h [33, 34], and can be divided into three parts.

1.3.1 Pile-up based Hall-Petch model

When h is greater than 50 ~ 100 nm, the dislocation pile-up based Hall-Petch scaling law can be used to explain the strengthening mechanism. Straight-edge dislocations on the same sliding plane piled up against the interface which resists the leading dislocation with a "barrier stress" of τ^*. When the force on the dislocation

reaches the value of resolved shear stress τ_0, dislocations are able to glide. The number of dislocations at one end of the pileup can be approximated by [18]

$$N = \pi h^{'}(\tau - \tau_0)/G^{'}b \tag{1.9}.$$

where τ is the resolved shear stress across the slip plane, b is the unit slip distance provided by a single dislocation. $G^{'} = G/(1-\nu)$, where G is the shear modulus, and ν is Poisson's ratio. τ_0 has many components, including a lattice resistance (Peierls-Nabarro stress), solid solution effects, and precipitation hardening. When the leading dislocation is just able to cross the interface, it follows that

$$\tau = \tau_0 + (\frac{G^{'}b\tau^{*}}{\pi h^{'}})^{\frac{1}{2}} \tag{1.10},$$

which provides the critical resolved shear stress to push the leading dislocation across the interface.

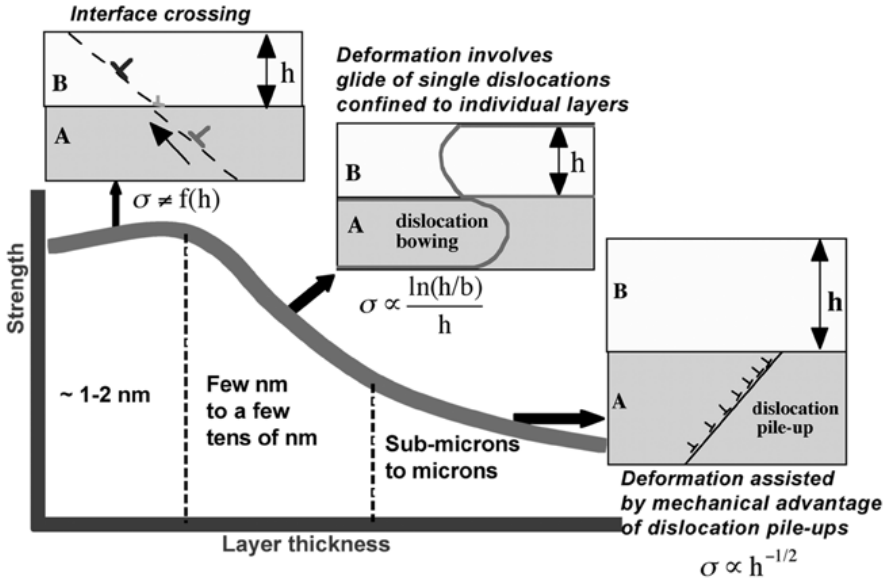

Figure 1.11 A schematic illustration of the deformation mechanisms in metallic multilayers as a function of individual layer thickness [33].

1.3.2 Confined layer slip in nanolaminates

When h is approximately 5 to 100 nm, deformation occurs by glide of single Orowan-type loops bounded by two interfaces [9, 35 - 37]. Since the interface barrier to dislocation slip transmission is higher than the gliding resistance, dislocation movement are confined to isolated layers, which can be also described as confined layer slip model (CLS) [34, 35, 37]. When threading dislocations or loops propagate in a confined layer, the dislocation will leave trailing dislocation lines of energy T per unit length along the interface. As depicted in Fig. 1.12, the critical resolved shear stress for such confined layer propagation is

$$\tau = \frac{G'b}{2\pi h'} \ln(\frac{h'}{b}) \quad (1.11),$$

where h′ is the distance along the sip plane between adjacent interfaces.

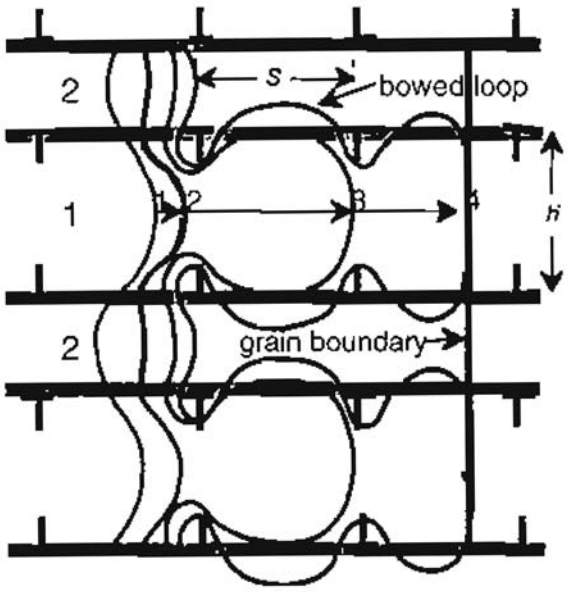

Figure 1.12 Successive configurations for a threading dislocation as a function of increasing applied stress leading to confined layer propagation [37].

1.3.3 The transmission of single dislocation across interface when h ≤ 5 nm

When h ≤ 5 nm, experimental data indicate that the strength of metallic multilayers reaches a saturation value and no significant increase is observed when h further decreases. Hence the deformation mechanism has, very likely, changed from CLS model to interface crossing of single dislocations [33]. The CLS stress, which increases as h decreases, will eventually exceed the interface barrier strength (τ*), and lead to the event

of dislocation crossing interface. The exact layer thickness at which the transition from CLS to interface crossing occurs depends on the magnitude of τ^*.

1.3.4 Other factors that impact the strength of multilayer films

The configuration of interface will also greatly affect the mechanical property of multilayer system. The strengthening effects from the structure barrier, modulus difference, coherency stress, and misfit dislocation density also need to be considered carefully [9, 38, 39].

1.3.4.1 Koehler image stress

The Koehler stress model originates from the large difference in the shear modulus between two constituents. In a system with a large modulus mismatch, there exists repulsive image stress when a dislocation in softer layer is going to cross the interface and enter into the component with higher elastic modulus. Resolved shear stresses required to overcome the repulsive images stress can be expressed as [38]:

$$\tau = bRG\sin\theta / 4\pi h, \qquad (1.12),$$

where b is the Burgers vector, $R=(G_A-G_B)/(G_A+G_B)$, G_A, G_B are the shear modulus of materials with higher and low shear modulus respectively, h is the distance of dislocation from the interface, and θ is the smallest angle between the interface and the glide planes of crystal with the smaller elastic constants. Clearly when h becomes small, the influence of the image stress will become significant.

1.3.4.2 Coherent interface

When layer thickness is very small and the lattice mismatch is not too large, it is easier to form coherent interface, where one layer is under compressive stress and the other layer under tensile stress. For epitaxial multilayer films with coherent interface, the mismatch strain is

$$\varepsilon = \frac{\Delta a}{a} = \frac{2(a^A - a^B)}{a^A + a^B}, \qquad (1.13),$$

where a^A and a^B are the lattice parameters of two component of the film. If we assume the maximum attainable flow strength of the composite is equal to the critical stress to move dislocations across the interface [40], then the yield strength of the multilayer films is determined by

$$\sigma = \frac{C^A C^B}{C^A + C^B}\varepsilon \qquad (1.14),$$

where C^A and C^B are the effective biaxial elastic constant for each component.

1.3.4.3 Incoherent interface with network of misfit dislocations

When the strain energy associated with the relaxation is larger than the energy of the dislocations created by such relaxation processes, misfit dislocation network will be generated at the interface. In interfaces with low shear resistance (so called “weak” interface), when a dislocation interact with the interface, the core of the dislocation tends to spread at the interface (due to a weak interface effect). The spread of dislocation cores

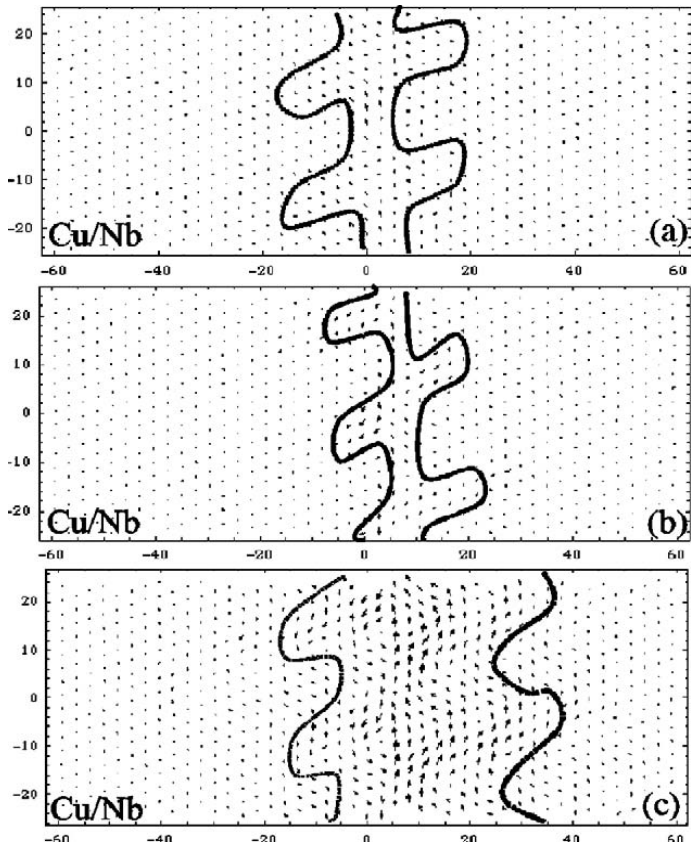

Figure 1.13 Distrgistry in the K-S Cu/Nb interface, showing core spreading when various glide dislocations enter the interface: (a) edge Shockley partial, (b) mixed Shockley partial, and (c) full screw dislocation [41 - 43].

at the interface can increase the strength of multilayer films. For instance, in Cu/Nb multilayers, the shear resistance of interface is significantly lower than that of each individual component; therefore, core spreading is expected in interfaces when a glide lattice dislocation enters the interface. Fig. 1.13 shows the disregistry plots after different dislocations enter Cu/Nb K-S interfaces. The arrows indicate disregistry vectors, and the curves outline the boundary between slipped and non-slipped regions. Since the

dislocation energy will decrease when the core spreads. The force on the glide dislocation is attractive when the dislocation approaches the interface. Fig. 1.13 shows that a strong attraction force for the dislocation is created by the sheared interface, particularly for the screw part.

1.3.4.4 Interface with ordering mismatch

When the heat of mixing of two layer components is negative, intermixing may occur along the interface. Combining mechanics of dislocation glide within individual layers, Koehler's image force and effect of layer miscibility, Chu and Barnett [44] provided a model to explain the hardness enhancement for the interface with intermixing. They got the conclusion that modulus difference and interface width were two major reasons that determine the hardening of multilayer films. For trapezoidal or sawtooth composition modulations, the maximum shear stress, the stress required for yield, was obtained when the dislocation was at the center of the interface region. And the maximum shear stress can be calculated as the sum of three parts: the effect of the extended dislocation strain field, the dislocation core and the average shear stress required for slip in homogenous materials with the same composition as at the center of the interface.

Besides the aforementioned factors, which are typically considered as major contributors to the strengthening of multilayer films, there are still some other factors deserved to mention [37].

1. The chemical stress associated with the motion of a dislocation from a layer with low stacking fault energy into one with high stacking fault energy.
2. The creation of a residual dislocation at the interface.
3. The interaction of dislocation with steps at the interface.

1.4 Radiation damage mechanisms

Radiation materials science deals with the interaction of radiation with matter, which occurs in the core of nuclear power reactors where the atoms of components are displaced numerous times over the course of their engineering lifetimes. After radiation, materials usually change the shape and volume, increase the hardness and severely reduce the ductility, or increasing trend of embrittlement. There are four types of radiation that can alter the structure of materials: neutrons, ions, electrons and gamma rays. All of these forms of radiation have the capability to displace atoms from their lattice sites, which is the fundamental process that drives the damages in structural metals. The effect of radiation on materials is rooted in the initial event in which an energetic projectile strikes a target, and the primary result is the creation of Frenkel defect pairs. Radiation displaces an atom from its site, leaving a vacant site behind and

the displaced atom eventually comes to rest in an interstitial position. The vacancy interstitial pair is central to radiation effects in crystalline solids and is known as a Frenkel pair [45]. The presence of the Frenkel pair and other consequences of irradiation damage determine the physical and the mechanical effects of irradiation.

The radiation damage event, which is the displaced atom (also known as the primary knock-on atom, PKA) comes to rest in the lattice as an interstitial, will consume about 10^{-11} s. Subsequent events are classified as physical effects of irradiation, which include void swelling, blistering, phase change, segregation, etc. The radiation damage event is the basis for understanding all effects of irradiation. A number of radiation experiments on 316 stainless steel alloy (Fig. 1.14) reveal that the yield strength enhancement is directly connected with the displacement damage [46] Therefore, quantifying the displacement process, which is a quantitative description of the number of vacancies and interstitials produced by an incoming projectile, is of special importance [45].

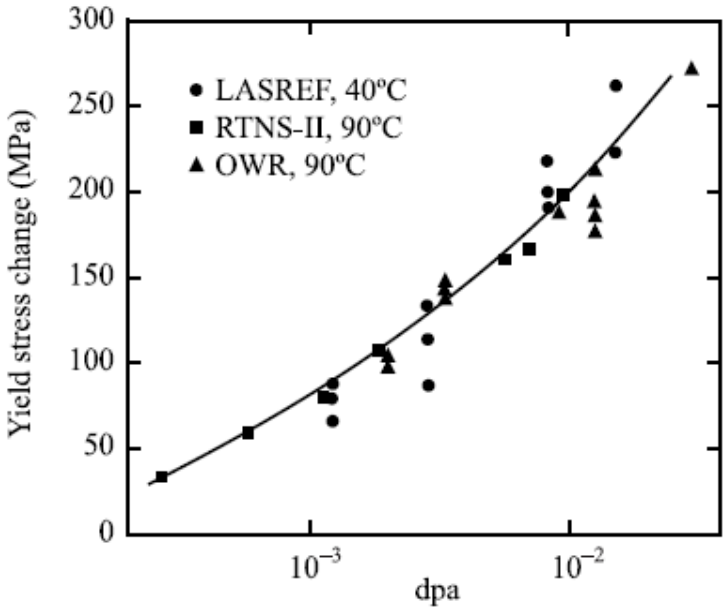

Figure 1.14 Comparison of yield stress change in 316 stainless steel irradiated in three facilities with very different neutron energy flux spectra. While there is little correlation in terms of neutron fluence, the yield stress changes correlate well against displacements per atom, dpa [46].

The number of displacements per unit volume per unit time R can be described as [45]:

$$R = N\int_{E\min}^{E\max} \phi(E)\sigma_D(E)dE \quad (1.15),$$

where N is the atom number density, E_{max} is the maximum energy of the incoming particle, E_{min} is the minimum energy of the incoming particle, φ(E) is the energy dependent particle flux, and $\sigma_D(E)$ is the energy dependent displacement cross section, which can be expressed as:

$$\sigma_D(E) = \int_{T\min}^{T\max} \sigma(E,T)\nu(E)dE \quad (1.16),$$

where T_{max} is the maximum energy transferred in a collision of a particle of energy E and a lattice atom, T_{min} is the minimum energy transferred in a collision of a particle of energy E and a lattice atom, σ(E, T) is the cross section for the collision of a particle of energy E that results in a transfer of energy T to the struck atom, ν(T) is the number of displacements per primary knock-on atom. The two key variables in this equation are σ(E,T), describing the transfer of energy from the incoming particle to the target atoms, and ν(T), the total number of displacements that the PKA goes on to make in the solid. Taken together, they describe the total number of displacements caused by an incoming particle of energy E.

1.4.1 Radiation damage

The minimum amount of energy in the collision to be displaced from its lattice site

represents the displacement threshold and is called the displacement energy, E_d. If the transfer energy to the lattice atoms, Γ, is less than E_d, the struck atom undergoes vibrations and stays in the lattice position. If, however, $\Gamma > E_d$, the struck atom is able to move out, leaving a vacancy and occupying an interstitial site in the lattice.

The displacement energy, E_d, is one critical parameter to evaluate whether the target atom is able to leave its lattice site and form a stable interstitial. This energy depends on the movement direction of the target atom. Due to the crystallographic structure, the displacement barrier to a lattice atom is not the same in all directions. For example, as shown in Fig. 1.15(a), the atom in the lower left-hand corner of FCC structure is assumed to receive energy by a collision. Possible low-index flight directions for the recoil are shown as wavy lines in the drawing. One obvious minimum in the displacement threshold will be in the [111] direction, through the center of the triangle formed by the three nearest neighbors. A schematic of the potential energy of the struck atom as it moves along the [111] direction is shown in Fig. 1.15(b).

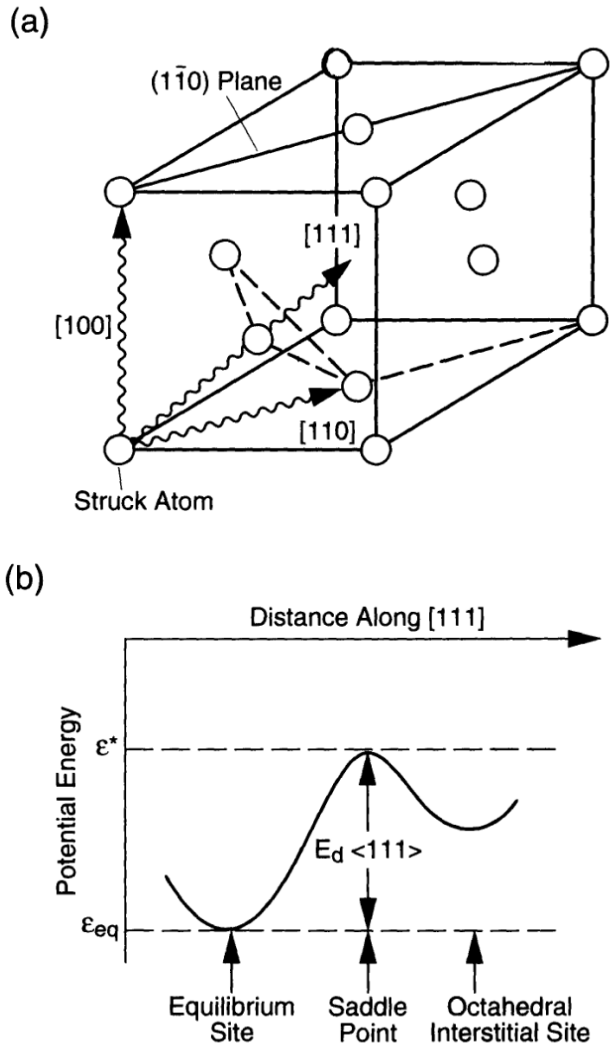

Figure 1.15 (a) Displacement of a lattice atom recoiling from a collision with an energetic atom; (b) potential energy of the struck atom as it moves along the [111] direction [47].

The threshold orientation dependence for Cu is shown in Fig. 1.16 [48]. If the struck atom moves off along its close packed direction, the displacement barrier will be high and the displacement energy needed to form a Frenkel-pair will be correspondingly high, because its neighbors have removed its energy before it escapes. The displacement

data indicate that the displacement threshold is considerably lower when the direction of the struck atom is along a line of atoms in the crystal (i.e., (100) and (110) directions) than it is in the open (111) directions.

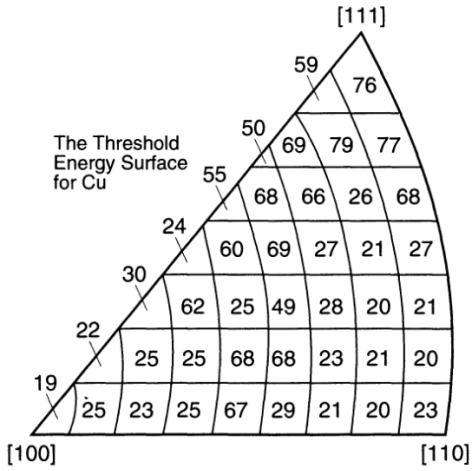

Figure 1.16 Directional dependence of the displacement threshold for Cu [48].

1.4.2 Displacements produced by a primary knock-on

Primary recoil atoms will be produced when an energetic incident ion undergoes a collision with a lattice atom. When the energy transferred to the PKA is large enough, E » E_d, the PKA can continue the knock-on-atom process, producing secondary or tertiary recoil atom displacements, which in turn can displace additional atoms. Such an event will generate lots of defects in near proximity of each other, which is commonly referred to as a collision or displacement cascade. The average number of displaced atoms in a

cascade produced by a PKA of energy E will be denoted by $N_d(E)$, also known as the displacement damage function. Based on the hard-sphere model of Kinchin and Pease [49], damage function $N_d(E)$ can be calculated. The following list the basic assumption in the Kinchin and Pease model [47, 50]:

(1) Collisions are between like atoms;

(2) The probability of transferring energy during the collision process is determined by a hard-sphere cross-section.

(3) The cascade is created by a sequence of two-body collisions;

(4) All collisions are elastic, i.e., only consider nuclear processes, ignoring electronic stopping;

(5) The energy E_d consumed in displacing an atom is neglected in the energy balance of the binary collision that transfers kinetic energy to the struck atom;

(6) The arrangement of the atoms in the solid is random and effects due to the crystal structure are neglected;

(7) A lattice atom receiving less than a critical energy E_d is not displaced. Similarly, if a knock-on atom emerges from a collision with $E < E_d$ it does not contribute further to the cascade. Also, atoms receiving energy between E_d and $2E_d$ are displaced but cannot themselves further increase the total

number of displacements.

Based on these assumptions, damage function can now be constructed as:

$$\langle N_d(E)\rangle = \begin{cases} 0 & (\text{if } E < E_d) \\ 1 & (\text{if } E_d < E < 2E_d) \\ E/2E_d & (\text{if } 2E_d < E < E_c) \\ E_c/2E_d & (\text{if } E > E_c) \end{cases} \quad (1.17),$$

and the dependence of displacement event on PKA energy is shown in Fig. 1.17.

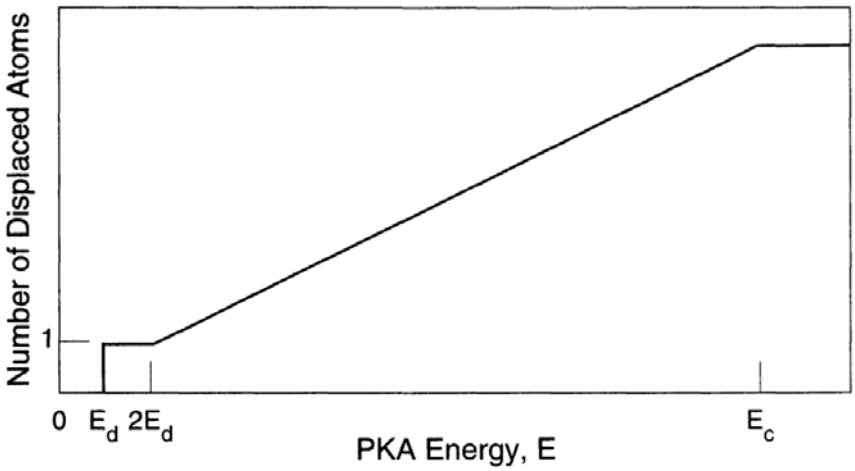

Figure 1.17 A graphical representation of the number of displaced atoms in the cascade as a function of PKA energy according to Kinchin and Pease model.

1.4.3 Mean free path and the displacement spike

Here the spatial distribution of point defects that are generated as PKA has been considered. An important quantity in determining the spatial distribution of irradiation damage is the average distance or mean free path, λ_d. The probability of a projectile with energy E undergoing a collision with a target atom, transferring energy greater than E_d

while traversing a thickness dx can be given by [51]:

$$P(E) = N\sigma(E)dx \qquad (1.18),$$

where N is the atomic density of the target and σ(E) is the total collision cross-section. Setting P(E) = 1 and replacing dx by λ_d, the mean free path, therefore, the mean free path λ_d can be expressed as:

$$\lambda_d = \frac{1}{N\sigma(E)} \qquad (1.19).$$

Calculation of the mean free path between recoils of Cu ions of various energies in a Cu target shows that: at high energy, Cu ions produce primary recoils well separated, however, at low energy, the distance becomes much less, until λ_d approaches the interatomic spacing. This indicates that as an ion slows down in the collision process, the mean free path will decrease accordingly.

Brinkman [52] has investigated the details of damage distribution in a cascade as a function of λ_d. As λ_d approaches the atomic spacing of the target atoms, a highly damaged region is formed where every displaced atom is forced away from the PKA path, producing a volume of material which is composed of a core of vacancies surrounded by a shell of interstitial atoms, as shown in Fig. 1.18. This highly damaged volume of material is referred to as a displacement spike.

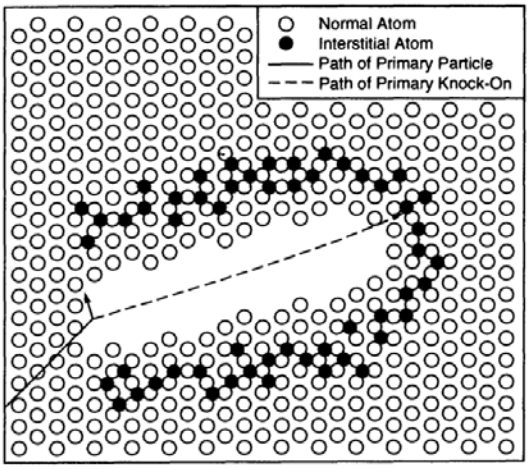

Figure 1.18 Schematic of a highly damaged volume of material which is formed when the mean free path between collisions, λ_d, approaches the atomic spacing of the target atoms. The dense cascade is referred to as a displacement spike [52, 53].

1.4.4 Thermal spike

As the formation of the displacement spike comes to an end, all the moving displaced atoms reach a point where they have insufficient energy to cause further displacement. At this point, the energy will be shared around neighboring atoms and finally dissipated as lattice vibrations. After approximately 10^{-12} s, a state of dynamic equilibrium may result where the vibration energy distribution begins to approximate a Maxwell- Boltzmann function. This period of lattice heating is known as the thermal spike phase of the collision cascade, and may exist for several picoseconds before being quenched to ambient temperature.

1.5 Radiation effects in metals

1.5.1 Defect configuration

The PKA can continue the knock-on-atom processes, producing secondary recoil atom displacements, which in turn can displace additional atoms. Immediately after displacement cascade, most of point defects (interstitials and vacancies) start to recombine and annihilate. On the other hand, a small fraction of the damage cascade will be left to form different extended defects such as vacancy clusters, voids and interstitial loops, as shown in Fig. 1.19. Stacking fault tetrahedral (SFT), shown in Fig. 1.20 as an evolution of vacancy agglomeration, are frequently observed in irradiated metals and alloys with faced-centered cubic (FCC) structure, such as Au, Cu, Ni, Pd and stainless steel [54 - 60].

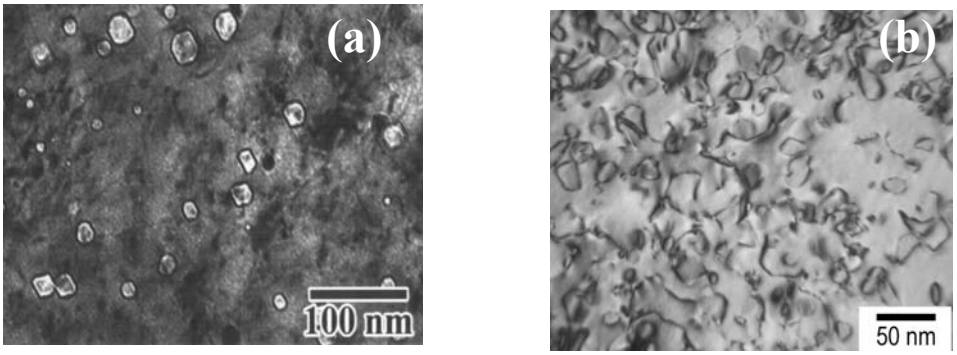

Figure 1.19 Observations of (a) voids and (b) dislocation loops from TEM images in the irradiated stainless steel [61].

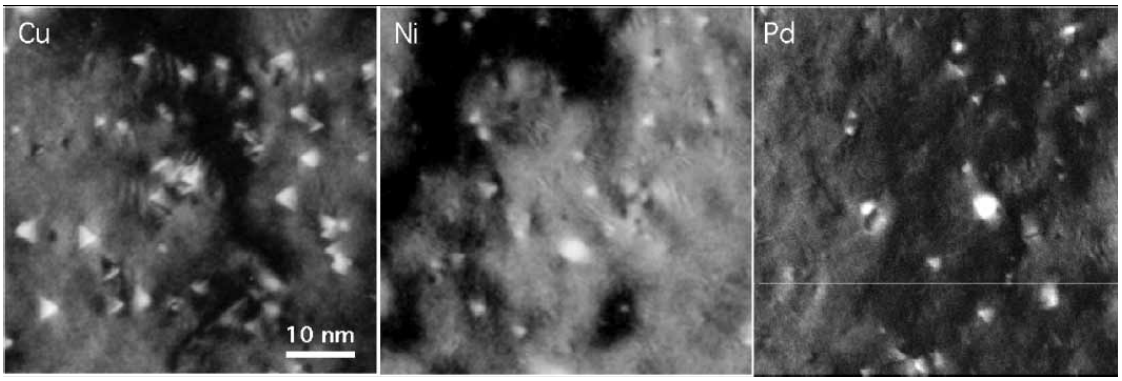

Figure 1.20 Observation of stacking fault tetrahedral (SFT) from TEM micrographs of Cu, Ni and Pd irradiated at room temperature [62].

In fusion reactors, besides voids, interstitial loops and SFT, a high concentration of He atoms can be created via (n, α) or other transmutation reactions typically, and then leads to formation of a large number of He bubbles. Fig. 1.21(a) shows the He bubble, produced by the irradiations in pure aluminium with 600 MeV protons, aligning along the grain boundaries [63]. Since He is insoluble in metals and alloys, it is inevitable that He atoms generated during irradiation will precipitate together to form He bubbles at grain boundaries and in the grain interior (Fig. 1.21(a)). It clearly shows that on average, the bubbles at the grain boundaries are larger than those in the matrix. However, the size of the bubbles on the dislocations is not uniform and depends on the local bubble spacing. It also exemplifies the formation of a bubble-denuded zone along the grain boundary.

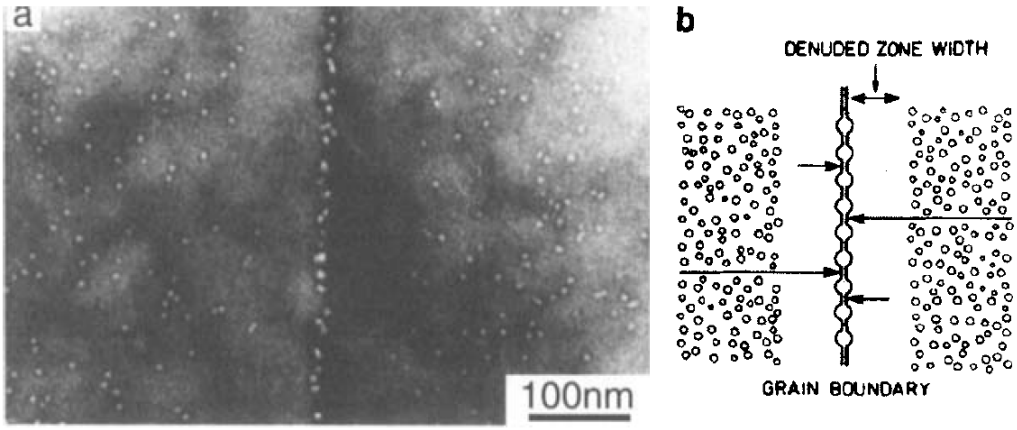

Figure 1.21 (a) Helium bubbles in the grain interior and at a grain boundary in high purity aluminium irradiated with 600MeV protons at 220°C to a dose level of 2.5dpa, (b) schematic illustrations of helium transport to a grain boundary from the denuded zone and the grain interior [63].

1.5.2 Formation mechanism of dislocation loops

During radiation, a loop is usually formed by condensation of radiation-produced vacancies or interstitials into roughly circular disks followed by collapse or the atomic planes adjacent to the platelet. Vacancy-loop formation is shown in Figs. 1.22(a) and 1.22(b), and the corresponding process for interstitials is depicted in Figs. 1.22(c) and 1.22(d). The ending result of the collapse or condensation process can be delineated by an edge dislocation. In the FCC structure materials, loops usually form on the closed packed {111} planes, where the defect formation energy is lower. The dislocation loops shown in Figs. 1.22(b) and (d) are Frank sessile dislocations. The dislocation encloses a stacking fault, and the loop can climb by absorbing or emitting point defects. The vacancy loop can grow by vacancy absorption and shrink, or even eliminate by

absorption of interstitials.

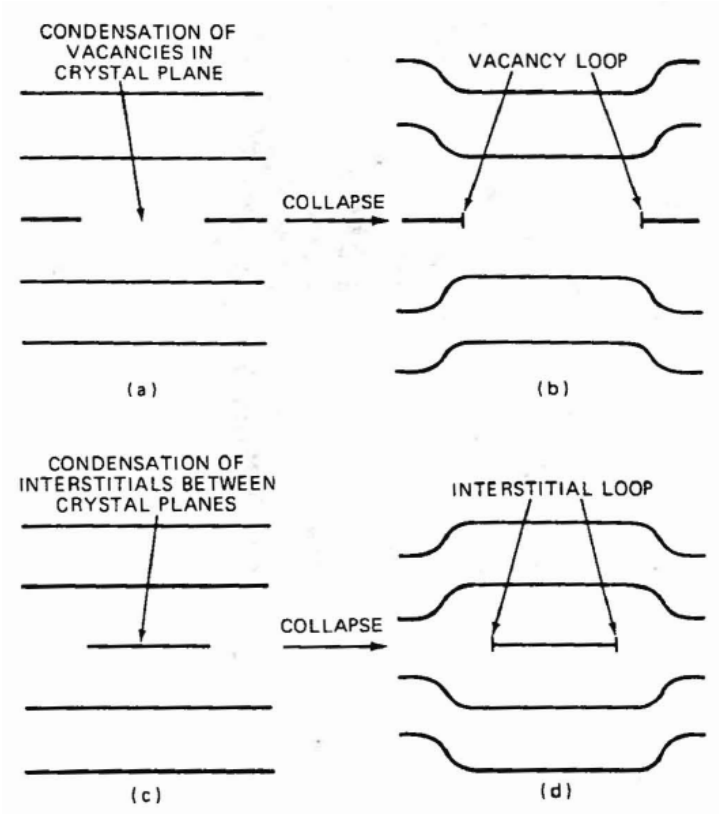

Figure 1.22 Formation of vacancy loops and interstitial loops.

1.5.3 Formation mechanism of stacking-fault tetrahedra

Stacking-fault tetrahedra are usually found in metals of low stacking-fault energy. Silcox and Hirsch first observed such tetrahedra in quenched gold foils [64]. Examples of tetrahedra in gold are presented in Fig. 1.23.

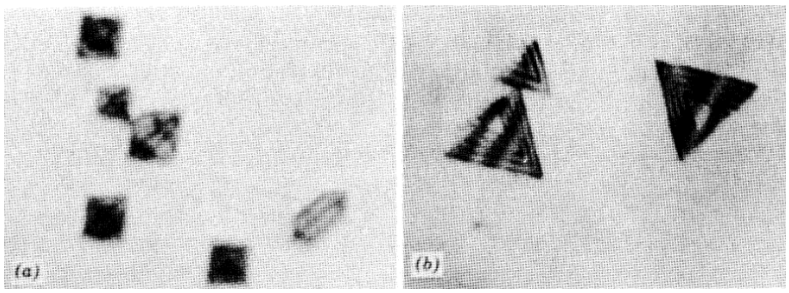

Figure 1.23 Stacking-fault tetrahedra in gold viewed by electron-transmission microscopy: (a) viewed along <100> [64], (b) viewed along <211> [18].

One mechanism of formation of tetrahedra is the extension of a Frank partial dislocation loop formed by vacancy condensation. Consider a loop of intrinsic fault bounded by the Frank sessile as shown in Fig. 1.24. Those portions of the loop which have line directions near <110> can dissociate and yield the configuration of Fig. 1.24(a). The decrease in energy accompanying the dissociation gives rise to forces that pull more of the original line of δD into <110>; the attractive interaction forces between βD, γD, and αD also cause the length of the dissociated segments to increase. These forces, plus any caused by favorably oriented shear stresses, lead to the development of configurations Fig. 1.24(b) and (c) in sequence. The final result is a tetrahedron bounded completely by intrinsic stacking faults and stair-rod dislocations.

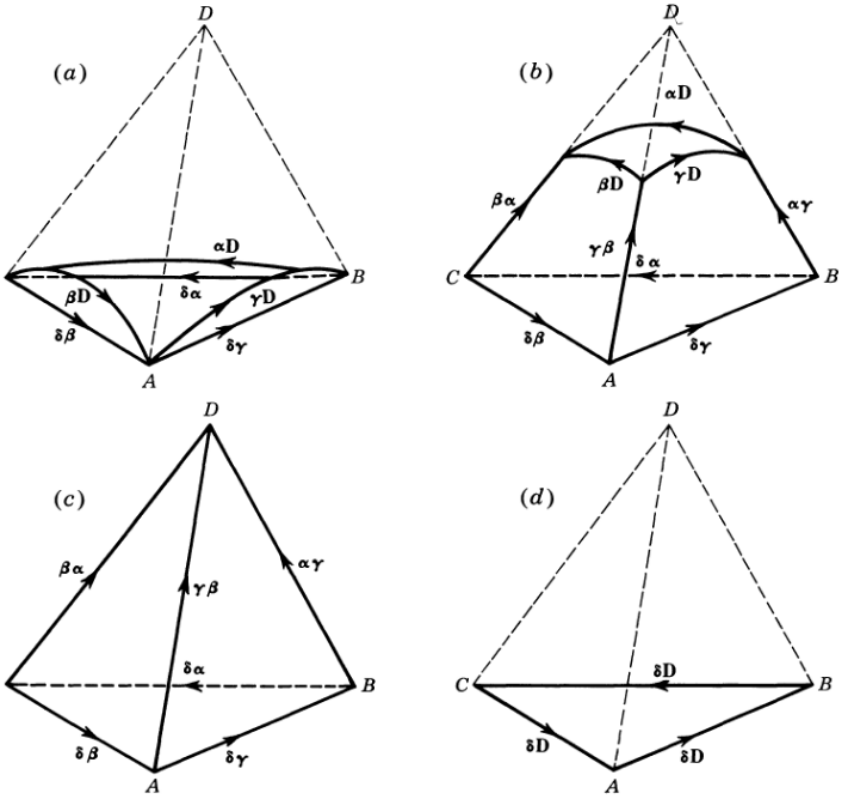

Figure 1.24 Various stages (a) to (c), in the formation of a stacking-fault tetrahedron from (d) a. Frank sessile loop.

1.6 Radiation hardening effects [45, 47]

In general exposure of most metals to ion irradiation results in an increase in yield strength. Typical engineering stress-strain curves for the two types of steels are shown in Fig. 1.25. Together with increasing yield strength after radiation, the ductility is reduced. Radiation hardening in both FCC and BCC metals is attributed to the radiation induced various defects within the grains, including point defects (vacancies and interstitials), impurity atoms, small vacancy clusters, dislocation loops, cavities, precipitates. Their

characteristics and barrier strength to gliding dislocations are listed below:

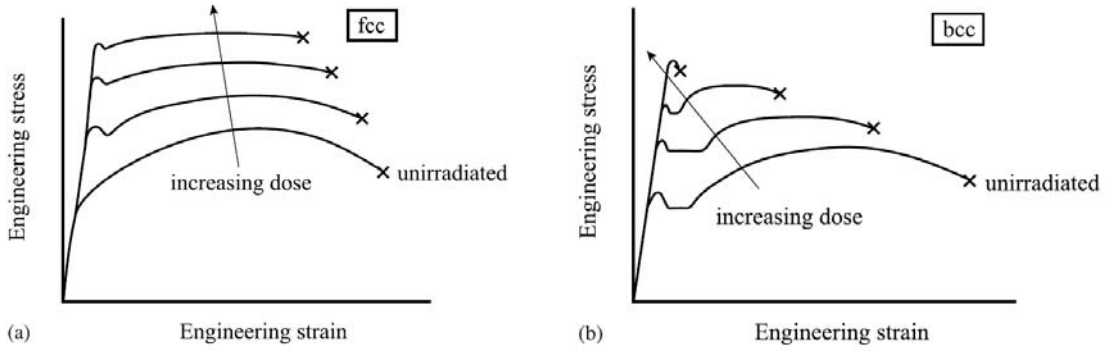

Figure 1.25 Effect of irradiation on the stress-strain behavior for (a) austenitic stainless steel (FCC metals) and (b) ferritic steel (BCC metals) [45].

- Frank loops: self-interstitial clustering. Once nucleated they can continue to grow by absorbing net self-interstitials. This growth continues until they become unstable and interact with network dislocations to be incorporated directly [65].
- Perfect loops and network dislocations: perfect dislocation loops can glide on their glide cylinders and continue to expand by net self-interstitial absorption. Network dislocations and large loops can restrain the movement of other gliding dislocations or annihilate with neighboring dislocations of opposite type, dislocation density decreasing (recovery).
- Bubbles: bubbles are primarily He-gas filled cavities. Because of extremely low solubility, He atoms combines with vacancies to form

bubbles. Once nucleated, the bubbles grow by absorbing isolated He atoms or vacancies [66, 67].

- Voids: beyond a certain critical radius, He bubbles become unstable and grow as voids by net vacancy absorption without the need to maintain mechanical equilibrium [67].
- Precipitates: a variety of second phases form as a result of thermally-induced precipitation and radiation induced segregation. The propensity to form these phases depends strongly on the material composition and environment [68].

Based on a dispersed barrier hardening model [69], the increase in yield stress $\Delta\sigma_y$ is equated to the increase in applied stress required to move a dislocation through a field of obstacles:

$$\Delta\sigma_y = M\alpha\mu b/l \quad (1.20),$$

where M is Taylor factor, α is the barrier strength, and l is the average spacing between obstacles. Table 1.2 provides a summary of the barrier strengths of various types of radiation induced defects. There is some relatively good agreement among studies: Voids and large precipitates act like Orowan (perfectly hard) barriers, with α approaching one; Frank loops and small precipitates have intermediate barrier strengths; and small bubbles, small loops, clusters and network dislocations have relatively small

barrier strengths.

Table 1.2 Comparison of obstacle strengths

Relative Strength	Barrier Type	Research System	α	Reference
Strong	Voids	Austenitics	1	[70]
	Voids	Ni	1	[71]
	Voids	Austenitics	1	[72]
	Voids	Austenitics	1	[73]
	Large Precipitates	Austenitics	1	[73]
Intermediate	Frank loops	Austenitics	0.33	[72]
	Frank loops	Austenitics	0.45	[74]
	Frank loops	Austenitics	0.45	[73]
Weak	Small bubbles	Austenitics	0.2	[72]
	Small loops/clusters	Austenitics	0.2	[75]
	Vacancy clusters		<0.25	[76]
	Dislocations		0.15-0.3	[77]
	Dislocations	Austenitics	0.11	[72]
	Dislocations	Austenitics	0.2	[73]

Radiation strengthens materials in two different ways. It can increase the stress required to start a dislocation moving on its glide plane, which is called source hardening. Once moving, dislocation can be impeded by natural or radiation induced obstacles close to or lying in the slip plane, which is called friction hardening.

1.6.1 Source hardening

Even without ion irradiation, the stress required to initiate dislocation motion can be identified with the unpinning stress of the Frank-Read sources in the metal, which is

inversely proportional to the distance between pinning points. The gradual yielding characteristics can be explained by the distribution of stresses required to operate the sources generating dislocations. In radiated metals, the yield point increases and is probably due to the irradiation-produced defect clusters standing in the vicinity of Frank-Read sources. These obstacles raise the stress required to expand the loops or to permit multiplication to continue.

1.6.2 Friction hardening

The friction forces responsible for resisting the motion of a dislocation through the crystal can be characterized as long range or short range. Therefore, the total applied shear stress can be expressed by the sum of the long-range and short-range stresses:

$$\sigma = \sigma_S + \sigma_L \qquad (1.21).$$

where σ is the friction stress and σ_S, σ_L represent the short-range and long-range contributions, respectively. The friction stress is roughly equal to the true stress at any point in the plastic deformation region of the stress-strain plot.

1.6.2.1 Long range stresses

The long-range forces arise from the repulsive interaction between the moving dislocation and the components of the dislocation network of the solid. Although the dislocation network of a metal does not resemble in a regular array, it still can be represented as a series of cubes, the edges of which are formed by dislocation lines. Fig.

1.26 shows such an idealized dislocation network with a loop on a glide plane tending to expand. The long-range forces are due to the interaction of the stress fields of the dislocation loop and of the dislocation network. For simplicity, the long-range force on the moving dislocation can be obtained,

$$F_{LR} = \frac{Gb^2}{2\pi l} \tag{1.22}.$$

The stress needed to overcome this force is F_{LR}/b; thus,

$$\sigma_{LR} = \frac{Gb}{2\pi l} \tag{1.23}.$$

After radiation, interstitial loops or other defects will be generated, increasing overall dislocation density, therefore, the long-range stress on mobile dislocations will increase accordingly.

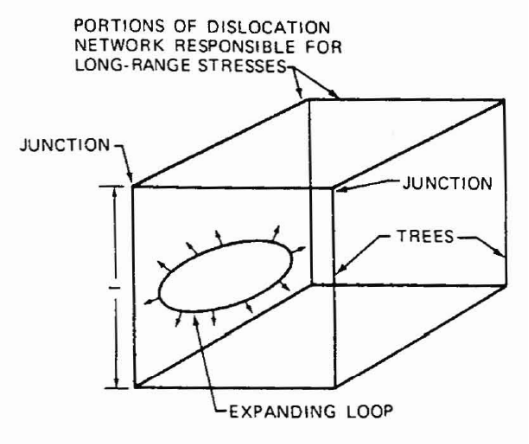

Figure 1.26 Model of the dislocation network in a solid [47].

1.6.2.2 Short-range stresses

Short-range forces are due to obstacles that lie in the slip plane of the moving dislocation. The short-range forces are active only when the moving dislocation comes very close to or contacts the obstacle. Furthermore, short-range forces can be divided into athermal and thermal components. Athermal mechanisms normally involve bowing of a dislocation around an impenetrable obstacle. In a thermally activated process, overcoming the obstacle usually requires that the moving dislocation cut through or climb over the barrier in its path.

The major difference between source and friction hardening can be interpreted as follows. (1) Source hardening has a major impact on the yield strength (the onset of plastic deformation) of materials. In other words, the activation of dislocation source (Frank-Read source) is impeded by the introduction of defect clusters. (2) Once dislocation sources are activated, the ease of continuous glide is determined by friction hardening, impedance originated from dislocation density (long range) and other obstacles (short range) in the gliding path of dislocations. Hence friction hardening can add onto the yield strength of materials, and determine the overall tensile strength after radiation.

1.6.3 Dose effect

Radiation hardening is also a function of the total dose of radiation. The tensile

curves obtained from proton-irradiated Cu single crystals at several doses are shown in Fig. 1.27 [78]. Hardening is present even at very low doses and the hardening increases with dose and has even not saturated at 0.2 dpa, almost one order of magnitude higher compared to the unirradiated critical shear stress value. The total shear strain before fracture also decreases with dose.

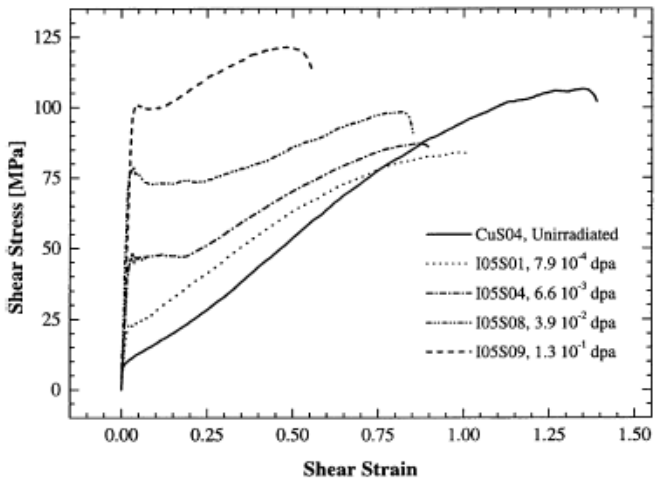

Figure 1.27 The shear stress-strain of Cu irradiated to different doses at ambient temperature [78].

1.7 Motivation and objective

In general, the effect of irradiation on materials is rooted in the initial event in which Frenkel pairs are generated. The central idea of this thesis is to use atomic-scale design of stable interfaces to attract, absorb and annihilate point defects. The idea of exploring irradiation tolerant metallic multilayer materials comes from the following

rationale:

1. Defect formation energies are significantly lower in certain type of interfaces than elsewhere in the crystal (0.1 ~ 0.3 eV in the interface as opposed to 1 ~ 3 eV in bulk) [15].

Fig. 1.28 presents the vacancy and interstitial formation energies in the Cu and Nb layers as a function of initial position normal to the Cu/Nb K-S interface. Away from the interface, defect formation energies approach the formation energy of the corresponding defect in bulk. At ~ 1 nm away from the interface, defects can interact with the interface and their formation energies decrease correspondingly. At the interface, the formation energies for both vacancies and interstitials are significantly less than the value in perfect crystal. When the Cu interstitial is ~ 1 nm away the interface, the formation energy is similar to those at the Cu/Nb interface. The relaxation process by MD simulation has been shown in Fig. 1.29 (a) - (d). At the beginning, the defect configuration is created within the Cu layer by putting into one extra Cu atom, and eventually, the defect is absorbed into the interface. Because this relaxation method was conducted by potential energy minimization (PEM) without any thermal agitation, the absorption of the defect into the interface involves either very small or no barriers to migration.

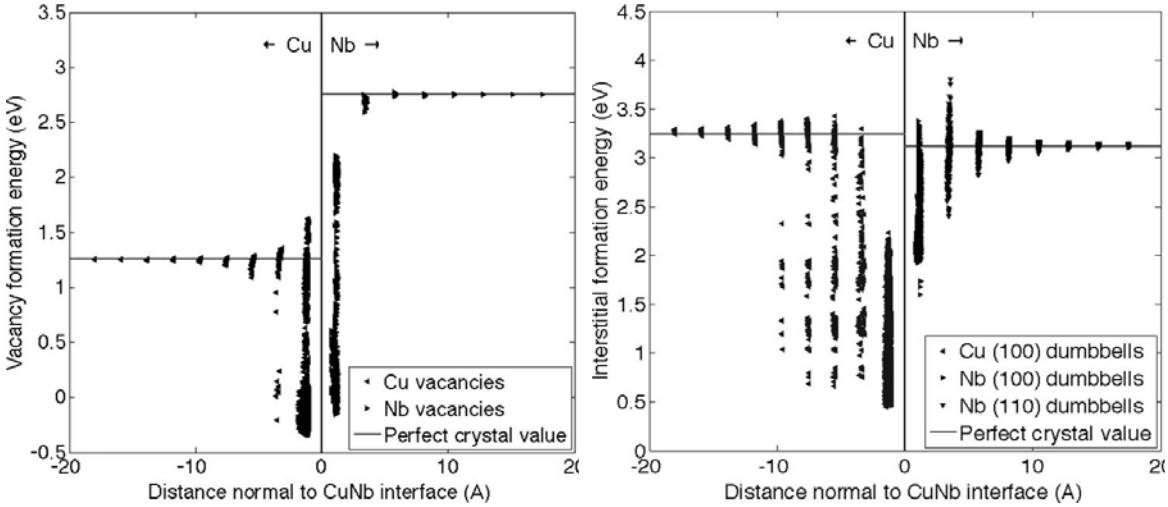

Figure 1.28 Dependence of vacancy formation energies in Cu and Nb as functions of distance normal to the Cu/Nb interface in the KS1 configuration. Dependence of interstitial formation energies in Cu and Nb as functions of distance normal to the Cu/Nb interface in the KS1 configuration [15].

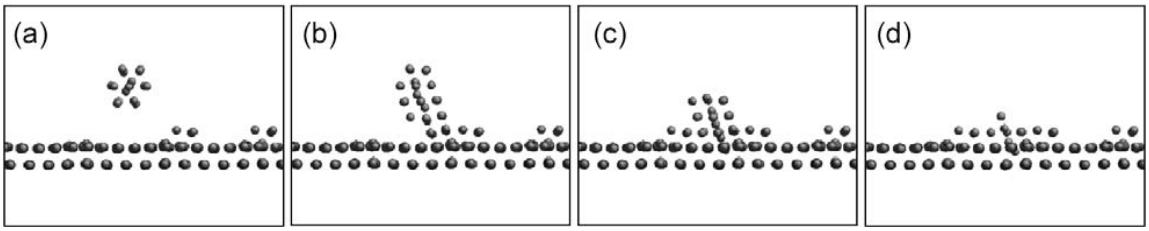

Figure 1.29 The process of relaxation by potential energy minimization (PEM) of a <110> split dumbbell interstitial inserted at a distance of 1 nm away from the Cu/Nb interface in the K-S configuration. Only atoms with high excess potential energy are shown.

2. The range of interaction with other point defects, the so-called core size of trapped defects, is ~ 6 times larger at interfaces than in bulk lattices.

The structure changes occurring at interfaces during the removal and insertion of some atom reveal the origin of the low formation energies of interfacial defects. The

configuration of interface after removal of one atom is totally different from a vacancy in perfect bulk materials, where the defect is localized.

Taking Cu-Nb interface as an example, after relaxation, changes in the vicinity of sites of atom removal or insertion in the Cu plane are shown in Fig. 1.30. During the process of local perturbation and relaxation, removal or insertion of one atom does not result in the formation of compact localized point defects. Furthermore, it can generate a large delocalized region of approximately 3 nm in diameter at the interface, which is considerably larger than the size of the point defect core region in perfect crystal. The delocalization of point defects at the interface will carry significant consequences for the annihilation of vacancy - interstitial pairs. During ion irradiation, materials will generate a huge amount of Frenkel pairs. Because of the large critical distance for vacancy - interstitial pair recombination at Cu/Nb interfaces, interfaces should promote radiation resistance.

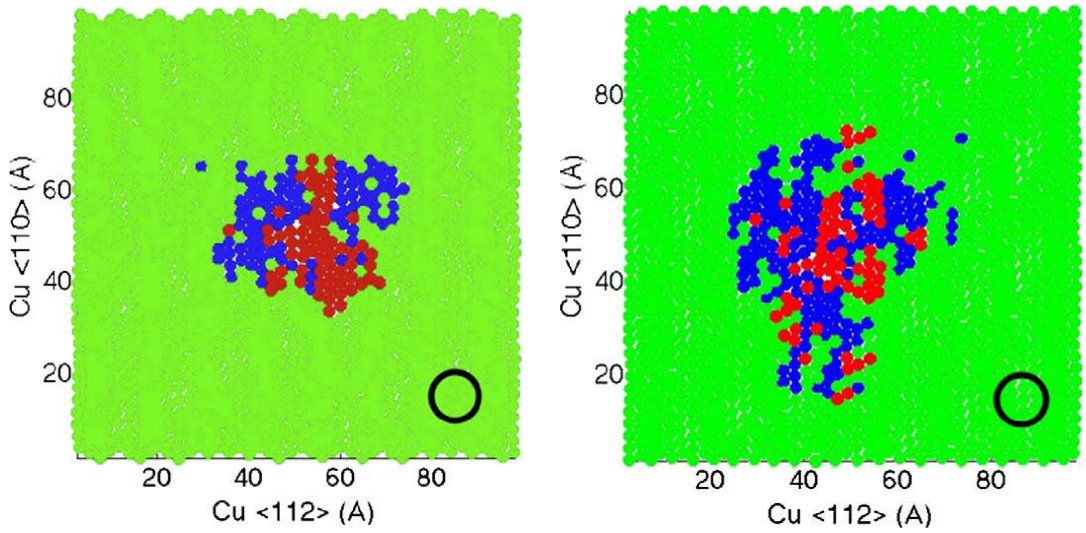

Figure 1.30 Changes in the volumes of atomic environments in the vicinity of atom (a) removal or (b) insertion in the interfacial Cu {111} plane of K-S indicate the extent of delocalization of defects in the interface plane. In these plots, red dots indicate atom sites where changes of the volumes > 0.02 $Å^2$, blue indicate changes of the volumes < −0.02 $Å^2$. For comparison, the black circles identify the size of the localized vacancy or interstitial in bulk Cu crystal [15].

3. The defect mobility at interfaces is higher by at least 5 orders of magnitude than in the bulk [15, 79].

By atomistic simulations, the phenomenon of dislocation climb at the interface has been observed through absorption and emission of vacancies and a counter diffusion of atoms in the interfacial plane, as shown in Fig. 1.31. The efficiency of dislocation climb is ascribed to the high vacancy concentration at the interfacial plane, the low formation energy to removal or insertion of atoms, and the low kinetic barrier for vacancy migration. As in Cu-Nb interface, diffusivity of one vacancy depends on its formation and migration energies at Cu-Nb interface plane, which is much lower than that in bulk

crystals. In addition, the migration of a point defect in the interfacial plane involves the rearrangement of a group of atoms with an associated delocalized displacement field within the interface, unlike single atom jumps for a vacancy in a bulk crystal. The kinetic barriers associated with the migration from one delocalized displacement field to the other is smaller, compared with a Cu adatom diffusing on a flat Cu {111} surface.

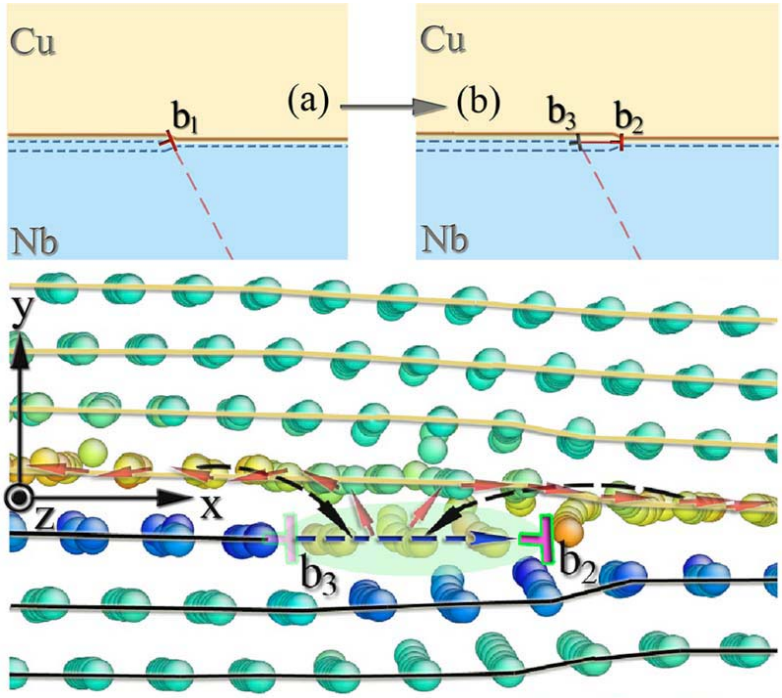

Figure 1.31 The dissociation of a mixed dislocation b_1 in the Cu/Nb interface. The schematic plots show (a) a mixed dislocation b_1 situated at the interface and (b) the dissociation into an interfacial dislocation b_2 and an interfacial discontinuity b_3 left near the trace of the Nb slip. (c) Atomic structures after the dissociation of the dislocation b_1 in the interface. The red arrows indicate the diffusion of vacancies and the black arrows indicate the counter diffusion of Cu atoms. The yellow lines outline Cu (111) planes, and the black lines represent Nb (110) planes [43, 79].

Due to the low formation energy, high diffusivity and larger core size of defects at interfaces, these Frenkel pair defects induced by ion irradiation can diffuse to interfacial regions and annihilate with each other, wiping out radiation damages and consequently reducing void swelling or blistering. Materials possessing a high volume fraction of certain type of interfacial regions may therefore be more irradiation tolerant than conventional polycrystalline materials.

The goal of this research project is to explore and construct certain types of interfaces in metallic nanolayers which are able to attract more radiation induced point defects and facilitate the annihilation of unlike point defects. Interface sink strength can be evaluated by the density of defect trapping sties and the increase in strain energy upon defect absorption. The major tasks of this research include: (1) design and fabricate metallic nanolayers with different type of interfaces; (2) at different layer thickness, explore the interaction of dislocations with layer interface; (3) identify the mechanisms of interactions between layer interfaces and radiation induced point defects, and (4) examine the evolution of microstructure and strengthening in multilayers after radiation. Several multilayer systems are selected to serve these purposes, including Cu/Mo, Fe/W and Al/Nb multilayers.

1.7.1 Cu/Mo multilayer system – immiscible fcc/bcc

Cu/Mo interface is selected because of its greater positive heat of mixing, 18 J/mol

[80]. The system should possess high temperature stabilities during ion irradiation. A large positive heat of mixing also indicates a weak interface, i.e., the bonding strength between Cu and Mo across layer interface may be weak.

1.7.2 Fe/W multilayer system – miscible bcc/bcc

Both Fe and W have bcc structure that could enable good radiation tolerance at higher temperature. When layer thickness is small, Fe/W interface is supposed to be coherent. In coherent interface, dislocation interactions with interface could be very different from that in weak interface scenario, such as Cu/Mo.

1.7.3 Al/Nb multilayer system – miscible fcc/bcc

Al/Nb has a unique fcc/bcc interface, where the interatomic spacing of Al (111) is essentially the same as that of Nb (110). Secondly, Al-Nb is a chemically miscible system with a negative heat of mixing of -18 J/mol [80], distinctively different from that of immiscible Cu/Mo system. Hence the strength of Al-Nb interatomic bond at interface should be stronger than that of Al-Al and Nb-Nb bonds. Both characteristics imply that interactions of radiation induced point defects with Al/Nb interface could be largely different than those in Cu/Mo system.

CHAPTER II

EXPERIMENTAL

2.1 Fabrication of metallic multilayer films

Magnetron sputtering is the technique used to produce metallic multilayer films in this work. The advantages of magnetron sputtering are as follows. (1) There are great versatility and flexibility in choosing a large variety of metallic materials for sputtering. (2) Films have better adhesion on substrates than other deposition techniques, such as evaporation. (3) The good conductivity of metals can guarantee discharge-free sputtering of targets. (4) For the same voltage applied, one to two orders of magnitude more current is available in magnetron sputtering than regular DC discharge technique [81].

The mechanism of magnetron sputtering technique is described below. Existence of magnetic field traps electrons uniformly close to the surface of a target as shown in Fig. 2.1. A parallel magnetic field is superposed on the glow discharge. Electrons in the glow discharge show cycloid motion, and the orbit drifts in the direction of the $E \times M$, where E and M denote the electric field in the discharge and the superimposed magnetic field. Magnetic field is oriented such that these drift paths for electrons form a close loop. This causes an increasing rate of collision between the electrons and the sputtering gas molecules. The magnetic field causes the plasma density to go up which leads to increased current density at the cathode, and hence raises the sputtering rate and

efficiency of the sputtering system [82]. Sputtering with a transverse magnetic field produces several important modifications. Target-generated secondary electrons do not bombard substrates because they are trapped in cycloidal trajectories near the target, and thus do not contribute to increased substrate temperature and radiation damage. In addition, this class of sputtering sources produces higher deposition rates than conventional sources and lends itself to economic, large-area industrial application. Since guns can also be shorted because of the falling metal flakes in between anode shield and target clamp, it is important to check the resistance between these two after changing the targets. A commercial vacuum cleaner is usually used for that purpose.

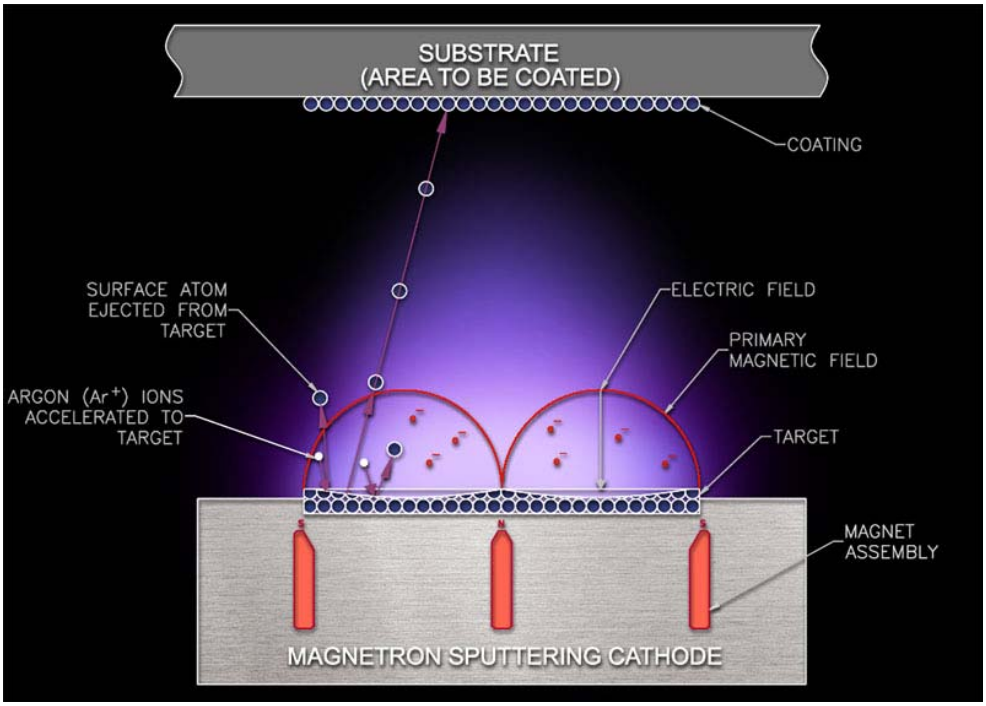

Figure 2.1 Working principle of magnetron sputtering [83].

Cu, Mo, Fe, W, Al and Nb metal targets were used to produce the metallic multilayer films in this work. After etching the Si substrates were immediately placed into the sputtering chamber via a load transfer system. The time interval between etching and placing the etched substrates into high vacuum chamber is usually less then 10 minutes. The chamber was evacuated to a base pressure of $5 \times 10^{-8} \sim 1 \times 10^{-7}$ torr prior to deposition. All depositions were performed at room temperature. No heating or cooling was applied to the substrate during deposition. The deposition rate was varied in the range of 5 ~ 10 Å/s by controlling the dc power to the magnetron gun and the distance between targets to substrate. Oxidized Si substrates (Si (100) with 1 μm thick SiO_2 layer) and HF etched Si (100) were used for depositions. The oxidized Si substrates are selected to avoid interdiffusion between the Si and multilayer films during annealing studies. The multilayer films grown on HF etched Si (100) were used to prepare TEM samples.

2.2 Characterizations of metallic multilayer interface by transmission electron microscopy (TEM)

Transmission electron microscopy (TEM) is critical in characterization of microstructures of sputtered multilayer films and radiation induced damage. TEM is a microscopy technique whereby high energy electron beam is transmitted through an ultra thin specimen, interacting with the specimen as electrons pass through. An image is

formed from the interaction of the electrons transmitted through the specimen, which is magnified and focused onto an imaging device, such as a fluorescent screen, on a layer of photographic film, or to be captured by a CCD camera [84].

TEM and Scanning TEM (STEM) were performed in the microscopy and imaging center (MIC) at TAMU equipped with two transmission electron microscopes. One is JEOL 2010 equipped with a Gatan SC1000 ORIUS CCD camera (Model 832), using 200 kV accelerating voltage with a LaB_6 filament. The microscope has 0.23 nm point-to-point resolution. The STEM and EDX were performed on a FEI Tecnai G2 F20 microscope with Fischione ultra-high resolution STEM HAADF detector (0.23 nm in the STEM image mode) and Oxford instruments EDX detector with a spatial resolution of ~ 1-2 nm.

2.2.1 Characterization of radiation damage by TEM technique

TEM technique has been particularly important in the field of radiation effects, where it has made many essential contributions to our understanding of how microstructures develop under irradiation. Depending upon the irradiation conditions and material, defect clusters may include dislocation loops of vacancy or interstitial nature, stacking-fault tetrahedra, bubbles and voids, all in a size range of the order of nanometers. Dislocation densities may be high with complicated geometries. In alloys, precipitation of second phases may be induced, enhanced, suppressed or impeded.

Segregation of alloying elements to or away from grain boundaries or dislocations may occur. Several points, list below, deserve special attention.

TEM has a finite resolution limit below which some loops are not detectable

The spacial resolution limit will depend on the type and functionality of the TEM microscope, sample quality, imaging conditions, and possibly the type of defect. In the best scenario, loops of diameter, d, ~ 1 nm are visible under the weak-beam condition, although it is necessary to record several images with varying s_g. SFT with edge lengths ≥ 1 nm are also visible under appropriate weak-beam or kinematical diffraction conditions [85].

In most TEM micrograph, only a proportion of the resolvable loops will be seen

Some loops will be out-of-contrast (i.e. $g \cdot b = 0$) and so will show only weak contrast which may be difficult to discern from background. The problem will be particularly severe for defects of size close to the resolution limit. These problems can be alleviated by imaging the same area under different diffraction conditions, using several diffraction vectors and deviation parameters s_g.

Loops may be lost from the foil due to surface image forces

This happens, for example, in heavy-ion irradiations of BCC and HCP metals, where the vacancy loops produced by the collapse of displacement cascades unfault to glissile prismatic loops. Jager and Wilkens [86] have shown that the presence of a

nearby surface may cause two effects. First, it may influence the unfaulting reaction. A given faulted loop of type b = 1/2<110> can unfault to one of three different b = 1/2<111> prismatic loop variants. The most likely variant to be produced is that with the largest component of b towards the surface. Second, if the elastic interaction energy of the loop with the surface is sufficiently high, surface image forces cause the prismatic loop to glide to the surface and be lost.

Counting may be difficult if the loop number density is very high

This problem may often be alleviated by the use of weak-beam rather than strong beam diffracting conditions. The narrower peak widths in weak-beam images make image overlap problems less severe. An interesting alternative approach to this problem may be applicable if the loops are faulted, which is usually the case, for example, in austenitic steels after neutron irradiation in the temperature range from 300 to 550 ºC. In this case it is possible to image the loops using fine-structure diffraction effects associated with the stacking faults.

The method is illustrated in Fig. 2.2, which is taken from the work of Brown [87]. Fig. 2.2(a) shows a bright-field image of a neutron irradiated M316 stainless steel containing a high number density of faulted Frank dislocation loops. Clearly this image is of little use for determining the number density or sizes of the loops and their distribution over different planes. Fig. 2.2(b) shows a selected area diffraction pattern.

The foil is oriented close to [100] and it is apparent that satellite spots are present around the four {200} reflections. The origin of these satellite spots are reciprocal lattice spikes associated with stacking faults on the inclined {111} planes, as shown schematically in Fig. 2.2(c). The satellites will be visible around a given {200} reflection only if the reflection is not strongly excited, so that its reciprocal lattice point is not intersected by the Ewald sphere. Five reciprocal lattice 'spikes' are associated with each reciprocal lattice point. One is in a direction normal to the thin foil, and the intersection of this spike with the Ewald sphere gives rise to the central {200} reflection. The other four spikes are normal to the {111} planes of the stacking faults, and it is the intersection of these inclined spikes with the Ewald sphere which gives rise to the satellite spots. Each satellite spot originates from the stacking-faults of Frank loops on a particular {111} plane. It is possible by careful positioning of a small objective aperture to form a dark-field image using one of the satellite reflections. The result of doing this is shown in Fig. 2.2(d). Now just one of the four sets of Frank loops is visible. Clearly this image is more suitable for counting and sizing this set of loops. By forming similar images using the other satellite reflections the other three sets of loops can be analyzed in the same way.

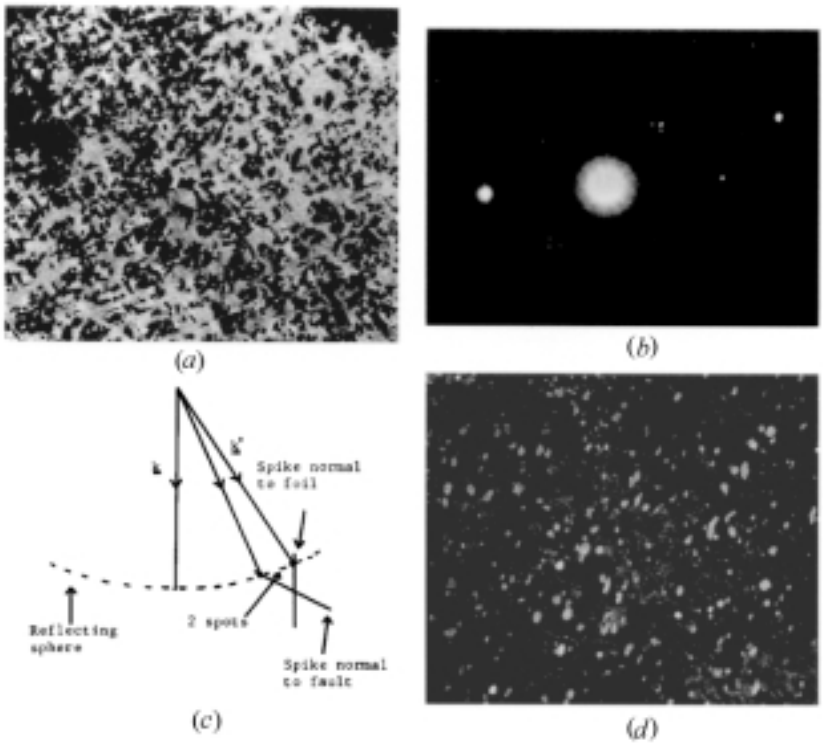

Figure 2.2 Faulted Frank loops in neutron-irradiated stainless steel: (a) bright-field image, with all four loop variants visible; (b) selected-area diffraction pattern, showing satellite spots around the 002 and 020 reflections; (c) schematic showing the origin of one satellite spot; (d) dark-field image obtained using one of the satellite spots, showing only one set of Frank loops.

2.3 Investigation of deformation mechanism of interface by in situ TEM

In situ nanoindentation studies were conducted at room temperature with a Nanofactory scanning tunneling microscopy (STM) platform inside a Tecnai G(2) F30 TEM operated at 300kV, which is available in Center for Integrated Nanotechnologies (CINT), Sandia National Laboratory. In TEM mode the instrument has a resolution of 0.20 nm at 300 kV. The instrument is equipped with scanning capability with a resolution of 0.14 nm in high-angle annular dark-field (HAADF) mode. It is also

equipped with energy-dispersive x-ray (EDX) analysis for detection of characteristic x-rays for elemental analysis, and an electron energy-loss spectrometer for characterizing composition as well as for energy-filtered imaging.

The STM-TEM system (as shown in Fig. 2.3) provides a unique combination of TEM and Scanning Tunneling Microscopy techniques, which are used simultaneously in one instrument for the full sample characterization. It consists of a STM equipped TEM sample holder, a controller and a PC with Nanofactory's data acquisition software. The STM probe scanner is integrated with a patented 3D approach mechanism having a very wide range of motion from picometers to millimeters, which is employed either for a coarse adjustment of the sample orientation, or a precise probe positioning. The STM indenter (tip) with a radius of ~ 50 nm moves along a direction normal to the layer interface at a constant velocity of ~ 0.2 nm/s. A Gatan CCD camera was used to capture the deformation of specimen during indentation with a frame rate of 2/sec.

Figure 2.3 Image of the STM-TEM indenter manufactured by Nanofactory.

2.4 X-ray diffraction (XRD)

X-ray diffraction is a powerful and non-destructive tool for the structural analysis of multilayer films. In the XRD experimental, the multilayer samples are exposed to a monochromatic beam of x-rays from a Cu-K_α source, which is used to investigate the crystal structure with a wavelength of 1.5405 Å. The thin film sample scatters the incident x-ray beam in all directions. However, due to the periodic arrangement of atoms on specific crystallographic planes in the crystalline solid thin film, the scattered x-rays mutually reinforce each other in certain directions. The position (angle θ) of the diffracted beam is given by the Bragg's law:

$$\lambda = 2d \sin\theta \qquad (2.1),$$

where λ is the wavelength for the incident x-ray beam, d is the spacing between planes that contribute to diffraction, and θ is the angle between incident beam and the crystallographic plane. From the intensity and position of the diffracted beam, various interplanar spacing, crystal structure, and orientation of the thin film are determined. Fig. 2.4 shows diffraction according to Bragg's law.

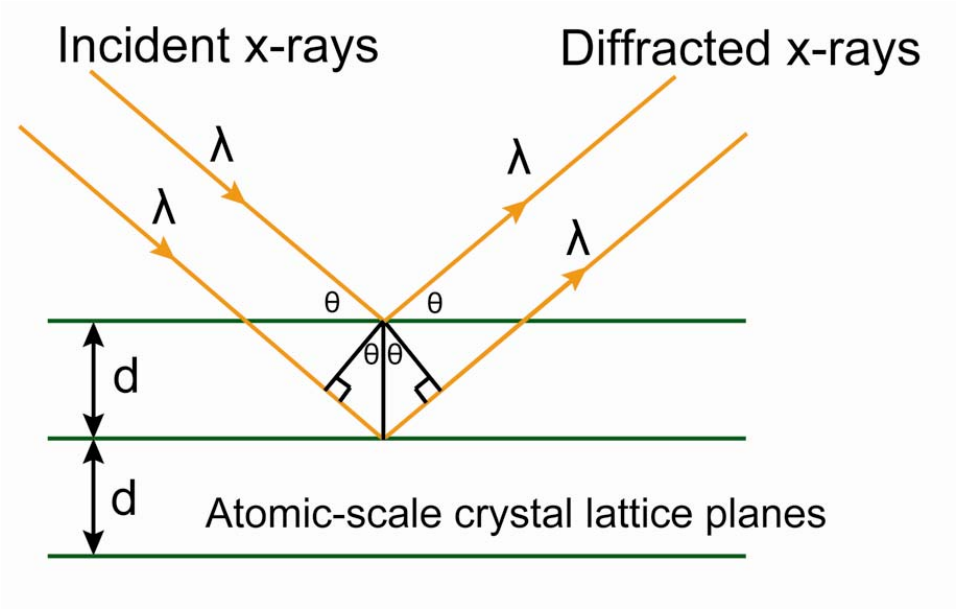

Figure 2.4 Schematic representation of the diffraction according to Bragg's law.

XRD was performed in the study by two Bruker powder diffractometers (D8 - Focus Bragg-Brentano and D8-Vario) in the X-ray Diffraction Laboratory at the Department of Chemistry. Bruker-AXS D8 advanced Bragg-Brentano X-ray powder diffractometer (XRD) is equipped with Cu-K_α source anode, D8 Goniometer, automatic divergence slit, graphite monochromator on the diffracted beam and Lynxeye PSD for detection. The divergent x-ray beam of filtered or monochromatized radiation impinges on the face of a sample. The angle between the direct x-ray beam and the diffracted beam is 2θ, where θ is the Bragg angle for each set of crystal planes. This is called the 2θ method. The divergent x-ray beam of filtered or monochromatized radiation impinges on the flat face of a sample. The sample is rotated at precisely half of the angular speed of

receiving slit so that a constant angle between the incident and diffracted beam is maintained.

2.4.1 Superlattice effects

During XRD experiment on the metallic multilayer systems, when h is ~ 5 nm or less, superlattice effect will affect the peak position. The characteristic length scales in superlattices are: (i) bilayer thickness, Λ (Λ = 2h), (ii) the inter planar spacing of constituents, and (iii) the structural coherency length, ξ, which is the distance over which atomic positions are quantitatively correlated, and it can be estimated from the full width half maximum (FWHM) by using the Scherrer's equation. The influence of interfacial constraint on lattice parameter of multilayers is more significant at smaller h [88, 89]. Hence we would anticipate greater magnitude of evolution of peak positions. When ξ is larger than Λ, the peak position can be indexed by [88]:

$$\frac{2\sin\theta}{\lambda_x} = \frac{1}{\overline{d}} \pm \frac{n}{\Lambda} \qquad (2.2),$$

where λ_x is the wavelength of x-ray, n is satellite order, $\overline{d}$ is the average lattice constant. The x-ray diffraction pattern of metallic multilayers can be simulated by the Schuller's model, expressed by: [89].

$$I \propto \frac{1+\cos^2 2\theta}{\sin\theta\sin 2\theta}\left|\left\{\begin{array}{l}\sum_{j=1}^{n}\exp[-W_A(\frac{\sin\theta}{\lambda_x})^2 f_A(\theta)\rho_A \exp(i\frac{4\pi}{\lambda_x}x_j\sin\theta)] \\ +\sum_{j=1}^{m}\exp[-W_B(\frac{\sin\theta}{\lambda_x})^2 f_B(\theta)\rho_B \exp(i\frac{4\pi}{\lambda_x}x_j\sin\theta)]\end{array}\right\}\right|^2 \qquad (2.3),$$

where $1 + \cos^2 2\theta$ is the polarization factor, $\sin 2\theta$ is the Lorentz factor, $\sin\theta$ is a geometric factor, f_A and f_B are the atomic scattering function of component A and B. ρ_A and ρ_B are in-plane atomic density of A and B respectively. W_A and W_B are the corresponding Debye-Waller factors. x_j is the position of the jth atomic plane, n is the number of A plane in one layer and m is the number of B plane in one layer, λ_x is the wavelength of X-ray. The atomic scattering function is given by [90],

$$f(s) = Z - 41.78214 \times s^2 \times \sum_{i=1}^{N} a_i \exp(-b_i s^2) \qquad (2.4),$$

where $s = \sin\theta/\lambda_x$, Z is the atomic number, a_i and b_i are materials dependent coefficients and N is the number of terms in the summation. The only adjustable parameter (to fit XRD profile) is the number of atomic planes. In the following chapters, we can see that the simulation has correctly captured major characteristics of X-ray profiles of Fe/W multilayers, including peak positions, relative peak intensity, peak broadening and line shape.

2.5 Nanoindentation

2.5.1 Definition of hardness

The mechanical properties of a material reflect its response or deformation to an applied load or force. Hardness is one of the important mechanical properties of a material and indicates its resistance to localized plastic deformation or to permanent penetration by another hard material. Measuring hardness involves two steps. Firstly a

small and hard indenter is pressed into the material with a load F and the displacement is composed of elastic and plastic deformation; secondly when the indenter is retracted, the elastic deformation is recovered and only the residual area A (plastic deformation) is measured [91]. Fig. 2.5 shows the schematic diagram of the cross-section of an indentation. The harder the material, the smaller and shallower is the indent. The hardness is defined by

$$H = P/A \qquad (2.5),$$

where H is hardness, P is load and A is residual area.

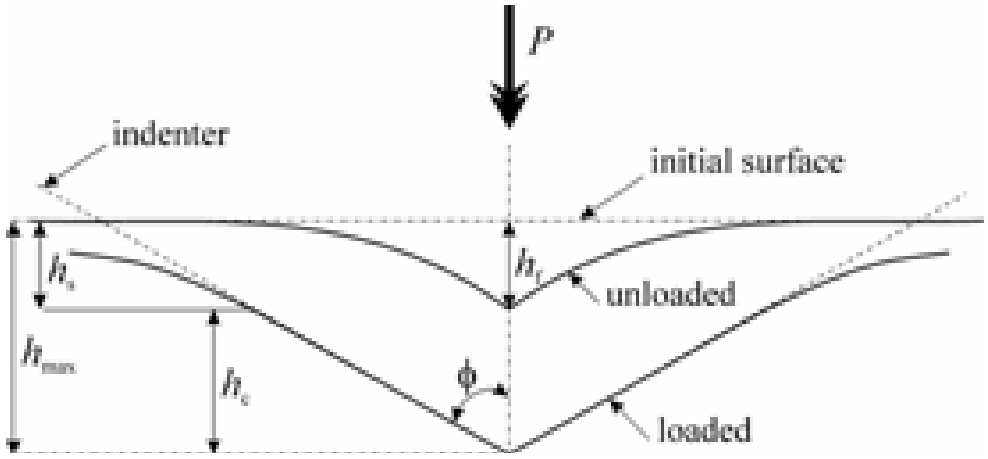

Figure 2.5 Schematic representation of the cross sectional indentation.

2.5.2 Determination of indentation hardness

The hardness of materials measured by nanoindentation is referred as indentation hardness (H_{IT}) and it is determined by equation

$$H_{IT}=F_{max}/A_c \quad (2.6),$$

where F_{max} is the maximum applied force and A_c is the projected (cross-sectional) area of the contact between the indenter and the test piece determined from the load-displacement curve. A_c can not be measured directly and is an area function, which describes the shape of the indenter tip, and hence it has to be expressed as a mathematic function relating to the depth of contact of the indenter with the test piece h_c [83]. The indentation hardness measurement process is similar to the conventional techniques. Hardness values are directly obtained from the load-displacement curve, but they are sensitive to the details of the analysis. Data analysis methods include elastic contact model [92 - 94], continuous stiffness method [95], and Herzian contact solution for spherical indenters [96]. Among these, the analysis based on elastic contact model developed and refined by Oliver and Pharr in 1992 [94] is the most commonly used nanoindentation analysis method, and is used to determine the indentation hardness of thin film in the dissertation as well. It assumed: (1) deformation upon unloading is purely elastic; (2) the compliances of the samples and of the indenter tip can be combined as springs in series and (3) the contact can be modeled using an analytical model for contact between a rigid indenter of defined shape with a homogeneous isotropic elastic half space using equation:

$$S = \frac{2E_r\sqrt{A_c}}{\sqrt{\pi}} \quad (2.7),$$

where S is the contact stiffness, A_c is the contact area, and E_r is the reduced modulus [94].

Based on these assumptions, contact depth h_c can be expressed by

$$h_c = h_{\max} - \varepsilon(h_{\max} - h_i) \quad (2.8),$$

where h_{max} is the maximum depth and h_i, the intercept depth, is the intercept of the tangent to the load-displacement data at the maximum load on unloading with the depth axis [94]. The correction factor ε, a function of the shape of the indenter tip, for flat punch is 1, conical punch is 0.73, Berkovich and Vickers indenter is 0.75, and for paraboloid of revolution (includes spherical) is also 0.75.

The procedure for data analysis to obtain indentation hardness is as follows: The slope of the fit at F_{max} is used to obtain h_i, and h_{max} at F_{max} is acquired in load-displacement curve shown in Fig. 2.6. Correction factor ε is determined by the shape of indenter tip. So the contact depth h_c can be obtained by inputting h_{max}, h_i and ε according to Eq. 2.8. The project area A_c is a function of shape of indenter tip.

For a Vickers indenter, a pyramid shape indenter with a square base, $A_c=24.5\times h_c^2$ and for a perfect Berkovich indenter, a diamond pyramid with triangular base, $A_c=23.96\times h_c^2$. The obtained h_c is inputted into the area function to get A_c. Finally the indentation hardness can be obtained according to Eq. 2.6.

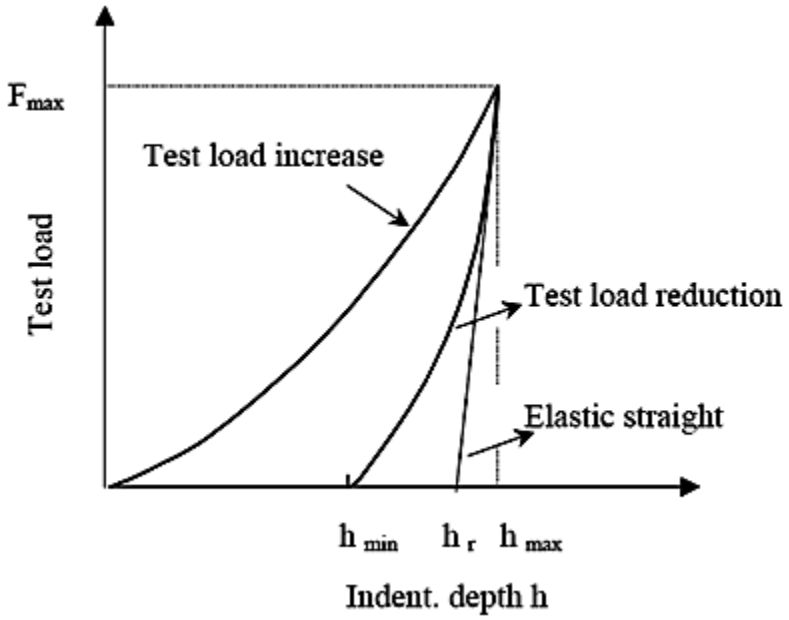

Figure 2.6 Schematic diagram of a loading-unloading curve during indentation

2.5.3 Determination of indentation modulus

The elastic contact model assumes that the compliances of the samples and of the indenter tip can be combined as springs in series, so

$$\frac{1}{E_r} = \left(\frac{1-\nu_{indenter}^2}{E_{indenter}}\right) + \left(\frac{1-\nu_{IT}^2}{E_{IT}}\right) \qquad (2.9),$$

where E_r is called reduced modulus, $E_{indenter}$ is the modulus of indenter and E_{IT} is modulus of the tested materials. $v_{indenter}$ and v_{IT} is the Poisson's ratio of the indenter and the tested materials, respectively. In the contact model, the contact stiffness describes the slope of the tangent of load-displacement curve during unloading cycle and can be expressed by Eq. 2.7 [94]. So reduced modulus is obtained by a rearrangement of Eq. 2.7

as:

$$E_r = \frac{S\sqrt{\pi}}{2\sqrt{A_c}} \tag{2.10}$$

According to Eq. 2.9, the E_{IT}, modulus of the tested materials can be expressed by E_r, which can be obtained according to Eq. 2.10 after contact stiffness, the slope of the tangent, is acquired from loading-unloading curves. So combining the Eq. 2.9 and 2.10, finally the E_{IT} can be obtained according to the following equation

$$E_{IT} = (1-\nu_{IT}^2)/(\frac{2\sqrt{A_c}}{S\sqrt{\pi}} - (\frac{1-\nu_{indenter}^2}{E_{indenter}})) \tag{2.11}$$

The indentation modulus is comparable to the Young's modulus of the material. Accurate quantitative measurements of indentation hardness and modulus may be obtained by nanoindentation measurements. However, results from this technique are influenced by many factors such as tip geometry, machine compliance, time-dependent displacements, surface roughness, indentation size, etc [81, 97 - 99].

2.5.4 Measurement of thin film hardness

The nanoindentation measurements in our study were performed by the Fischerscope HM2000XYp measurement system, which measures the indentation hardness according to ISO 14577. Basically, the hardness measured with Fischerscope HM2000XYp is determined from the area of the indenter displacement under load. The indentation depth and a constant, specific to each indenter, are used to calculate the area

of the indenter displacement. The positioning devices consist of the holding device for the measuring head and a microscope with an attached video camera for examining the test area shown on the computer monitor. Manually adjustable XY measuring stage and programmable XY measuring stage are equipped in the tester. The coordinates of the measurement points can be stored and visited automatically in sequence. A Vickers indenter was used as the indenter. The load range is from 0.4 to 2000 mN and the maximum indentation depth of the indenter is 150 μm. The hardness and indentation modulus of metallic multilayer films were measured based on an average of 9-12 indents at different indentation depths at room temperature with the same loading rate. The maximum indentation depth was kept at ~ 200 nm for all specimens. The low surface roughness of the thin film (a few nm) leads to a negligible roughness effect. The total thickness of the films is ~ 2 μm.

2.6 Ion accelerator for ion implantation studies

The basic elements in the typical ion accelerators illustrated in Fig. 2.7 include ion source, acceleration column, mass separator, beam sweeping and target chamber. A wide variety of ion beams with sufficient intensity for irradiation can be produced by different types of ion sources. The total fluence (ion dose) varies with the irradiation time and beam current density.

In this dissertation, He ion implantation at energy up to 100 keV with a fluence

level up to 6×10^{17} ion/cm^2 was performed in Dr. Lin Shao's accelerator laboratory at the Department of Nuclear Engineering at TAMU. The Accelerator Laboratory is one of the largest university ion irradiation facilities in the U.S. A total of five accelerators are able to deliver virtually all ions in the elemental table with ion energy from a few hundred to a few MeVs. The lab provides unique capabilities to perform accelerator based irradiation studies on various nuclear materials.

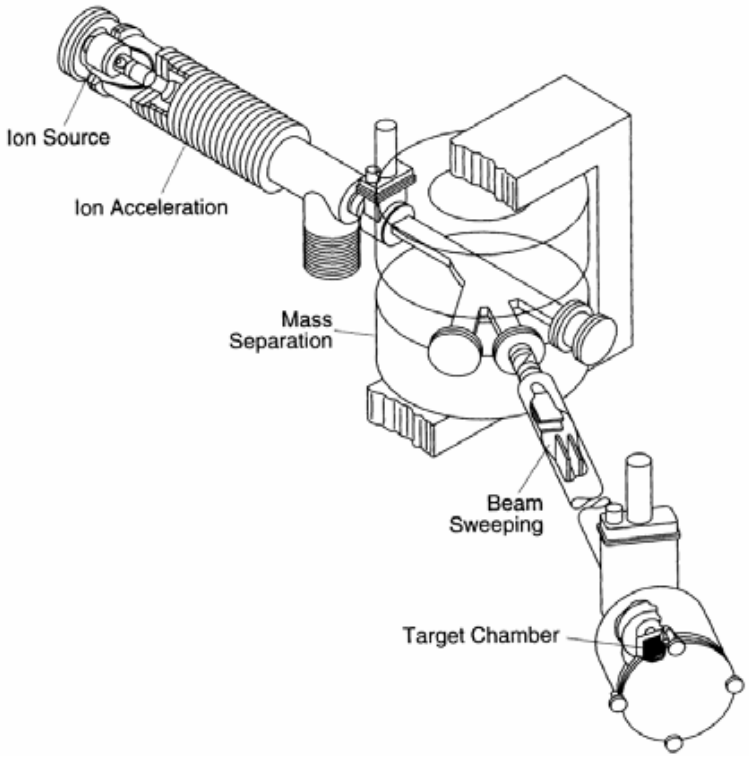

Figure 2.7 Schematic diagram of typical ion irradiation system.

CHAPTER III

MECHANICAL PROPERTIES OF AL/NB (FCC/BCC) INTERFACE – IN SITU NANOINDENTATION STUDIES OF INTERFACE-DISLOCATIONS INTERACTIONS IN AL/NB MULTILAYERS

3.1 Overview

Using *in situ* nanoindentation inside a transmission electron microscope, we investigate the interactions of dislocations with interfaces in Al/Nb multilayers. The studies reveal that (1) interfaces act as strong barriers for the transmission of dislocations and sinks for absorbing dislocations; and (2) dislocations can climb along the Al/Nb interfaces, facilitating the annihilation of dislocations within interfaces. The climb velocity is estimated to be approximately 0.4 nm/sec, much higher than that in bulk materials. These findings imply that interfaces play a crucial role in determining the deformation mechanisms of nanoscale Al/Nb multilayers.

3.2 Introduction

Interfaces between dissimilar metals often exhibit unique properties that are not found in bulk crystals [100]. For example, Cu/Nb interfaces can adopt multiple atomic structures with nearly degenerate energies, stimulating the delocalization of point defect within interface and their interactions [101, 102, 41, 33, 42, 19, 103, 79]. Atomistic simulations have revealed that the formation and migration energies of vacancies and

interstitials within interfaces are lower than that in bulk materials, implying that these interfaces can act as strong sinks for vacancies and interstitials [19, 103]. Using atomistic simulations, we have also shown that dislocations can efficiently climb near and within interfaces through both the emission and absorption of vacancies at dislocation cores [79]. Also these interfaces can act as strong barriers for slip transmission because the dislocation core spreads in interfaces as a result of their low shear resistance and the discontinuity of slip systems across these interfaces [35, 43, 44, 101, 102]. Through dislocation climb, dislocation debris within interfaces can be reassembled into lattice dislocations, moving away from interfaces under applied stress. In addition, reactions between interfacial dislocations assisted by climb could lead to partly annihilation of dislocations (removal of certain dislocation contents), and hence lead to partly recovery within interfaces.

Atomistic simulations so far provide insight into the interaction of interfaces with dislocations, implies that these interfaces may play a crucial role in determining the strength and deformation mechanisms of nanoscale multilayers [103]. However, experimental study, in particular, real time observations of the dislocation-interface interactions are still scarce. In this letter, we report direct observations of the dislocation-interface interactions in the Al/Nb multilayers by using *in situ* nanoindentation inside a transmission electron microscope and the studies provide strong

evidence for the role of interface in prohibiting slip transmission and facilitating dislocations annihilations.

3.3 Experimental

Al/Nb multilayer with individual layer thickness of 5 nm (referred to as Al/Nb 5nm thereafter) was deposited by using the DC magnetron sputtering technique on Si (100) substrate at ambient temperature. The chamber was evacuated to a base pressure of $\leq 5 \times 10^{-8}$ torr prior to deposition. The deposition rate was ~ 0.6 nm/s. High resolution transmission electron microscope (HRTEM) was performed on a JEOL 3000F microscope operated at 300 kV. *In situ* nanoindentation studies were conducted at room temperature with a Nanofactory scanning tunneling microscopy (STM) platform inside a Tecnai G(2) F30 transmission electron microscope (TEM) operated at 300kV [104]. The STM indenter (tip) with a radius of ~ 50 nm moves along a direction normal to the layer interface at a constant velocity of ~ 0.2 nm/s. A Gatan CCD camera was used to capture the deformation of specimen during indentation with a frame rate of 2/sec.

3.4 Results and discussions

Fig. 3.1(a) is a cross-sectional TEM micrograph of Al/Nb 5nm multilayer. Diffraction pattern (DP) shows that Al/Nb multilayer film has strong Al {111} and Nb {110} texture, and $\mathrm{Al}(11\bar{1})$ || Nb (110) || Al/Nb layer interface. The mean columnar grain size is approximately 100 nm. HRTEM micrographs of Al and Nb adjacent to interface

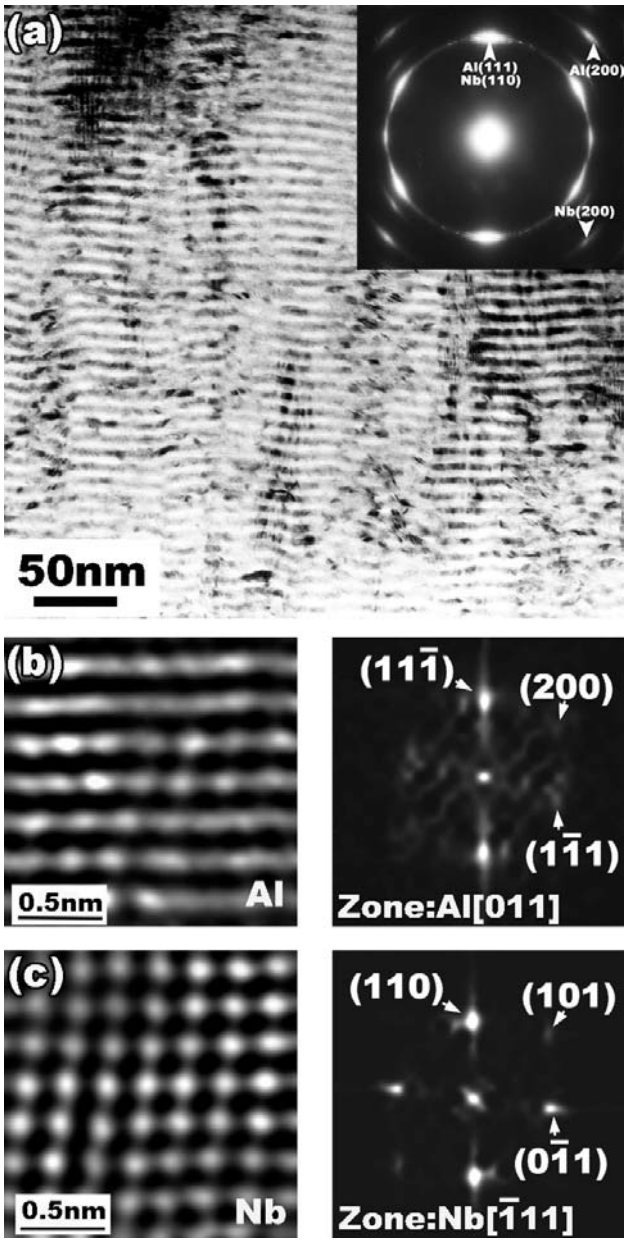

Figure 3.1 (a) XTEM micrograph of as-deposited Al/Nb 5nm multilayer film. The inserted selected area diffraction (SAD) pattern shows a strong Al {111} and Nb {110} fiber texture. (b) Cross-sectional HRTEM micrograph of Al layer adjacent to layer interface and the corresponding FFT, indicating an Al [011] zone axis. (c) HRTEM micrograph of the adjacent Nb layer and corresponding FFT, indicating a Nb [$\bar{1}$11] zone axis. The Al and Nb interface possess a Kurdjumov-Sachs orientation relation: (11$\bar{1}$) Al || (110) Nb, [011] Al || [$\bar{1}$11] Nb.

as shown in Fig. 3.1(b) and 3.1(c) reveal a Kurdjumov-Sachs (KS) orientation relation, i.e. Al $(11\bar{1})$ || Nb (110), Al [011] || Nb $[\bar{1}11]$.

Fig. 3.2(a) shows a cross-sectional HRTEM micrograph of Al/Nb 5 nm multilayers during the *in situ* nanoindentation test. The location of indenter tip is also labeled. Fig. 3.2(b) is the magnified image of the square box marked in Fig. 3.2(a). Dislocations and their locations are marked in the image by identifying extra compact atomic planes, $(11\bar{1})$ in Al and (110) in Nb. The pure screw dislocations cannot be identified using this technique due to the absence of extra atomic plane and will not be considered further. The identified dislocations are then grouped into two types with respect to their locations: type 1 at interfaces and type 2 inside the layers. Considering the width of dislocation cores, dislocations within 3 atomic layers to the interface are grouped into type 1. Fig. 3.2(c) plots the evolution of dislocation density during nanoindentation experiments. It reveals that the density of dislocations at interfaces is ~ 4 times higher than those inside the layers. These observations have following implications. (1) Dislocation activities remain abundant inside crystal lattice even at a layer thickness of 5 nm. These dislocations with a density of 10^{15}-10^{16} m^{-2} should account for a large magnitude of plastic deformation in crystals. (2) The higher dislocation density could indicate that interfaces block the transmission of lattice dislocations. If the lattice dislocations (inside layers) can quickly propagate through layer interfaces, one would anticipate an identical

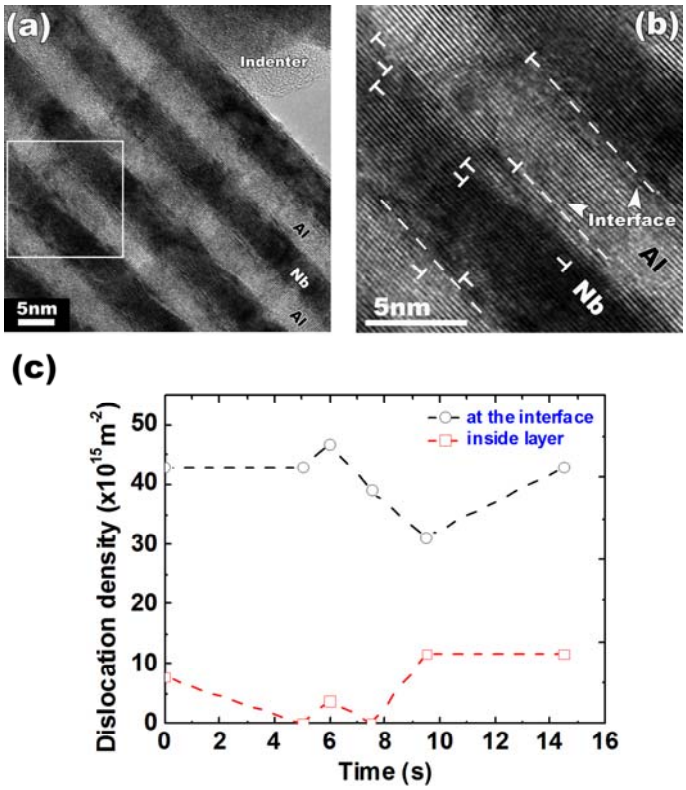

Figure 3.2 (a) XTEM micrograph of Al/Nb 5 nm film under the tip of a nanoindentor during indentation process. (b) HRTEM micrograph of the square box in (a) showing dislocations. Interfaces are delineated with dashed lines. (c) The evolution of dislocation densities both inside the layers and at the interfaces with time during indentation process.

dislocation density at and away from layer interfaces. In Al/Nb multilayers, the crystal structures are drastically different across interface, and hence lead to discontinuity in slip system [42]. Dislocations entering interface are likely to be trapped by the interface, and reemission of interface dislocation requires higher magnitude of resolved shear stress. Hence the higher dislocation density at layer interface provides direct evidence that Al/Nb interfaces act as strong barriers to the transmission of dislocations.

Another noteworthy phenomenon is the observation of wide stacking faults (SF) inside Al layer during *in situ* nanoindentation. Fig. 3.3(a) shows a stacking fault generated in Al, with one end at the interface and the other end inside Al connected by a Shockley partial dislocation. The inverse fast Fourier transform (IFFT) of the HRTEM image, in Fig. 3.3(a'), shows that the stacking fault has a length of ~ 2.4 nm. The leading and trailing partial dislocations are labeled in the figure as b_L, and b_T respectively. During nanoindentation, an applied compressive stress σ can be converted to resolved shear stress (RSS) τ_{rss}. The Peach-Koehler glide force acting on the leading Shockley partial dislocation, composed of four terms,

$$F_L = \tau_{rss} b_L - \gamma_{SF} + F_{b_L b_T} - F_P^L \qquad (3.1),$$

tends to move the leading partial towards the upper interface or away from the lower interface. The positive sign of the glide force is defined with respect to a direction away from the lower interface. The first term on the right in Eq. 3.1 represents the contribution

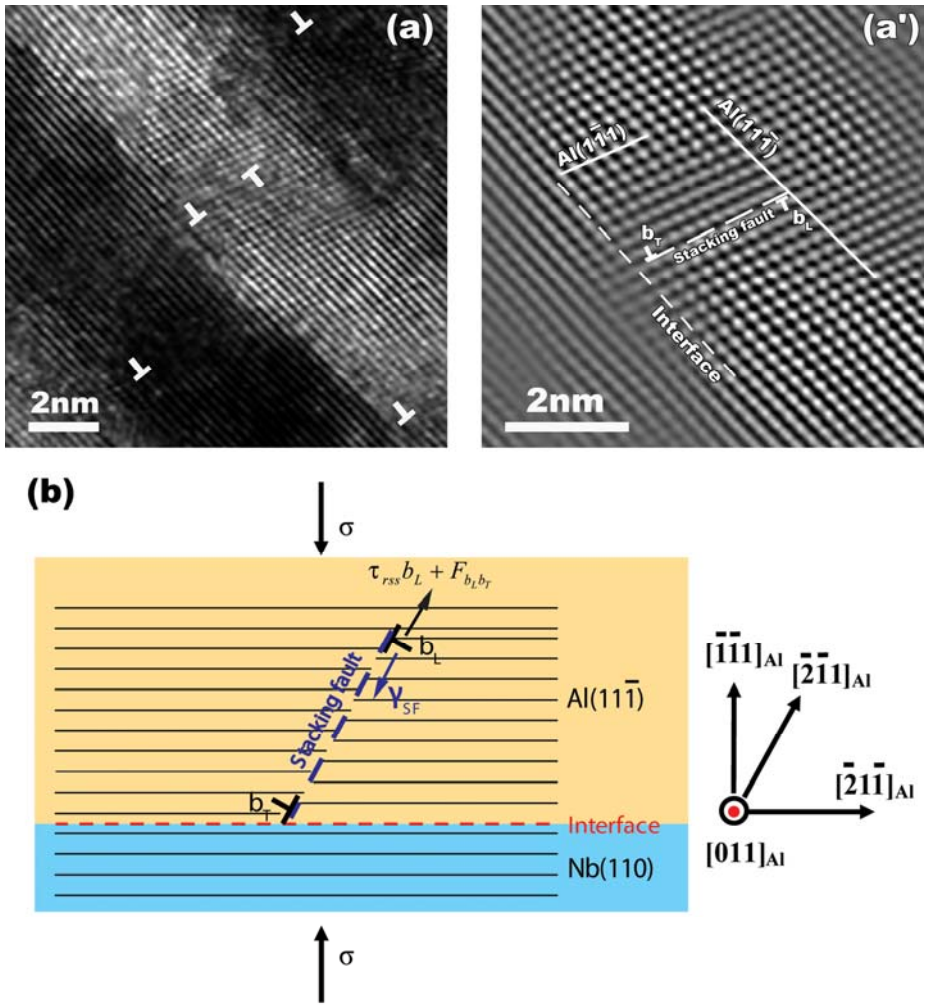

Figure 3.3 HRTEM image of a stacking fault inside Al layer (a) and the corresponding FFT processed TEM image (a') at higher magnification. The stacking fault is bounded by a leading and trailing partial, labeled as b_L and b_T. The trailing partial resides at the layer interface. (b) A schematic plot of the pining mechanism for a partial dislocation pinned by the interface. The forces acting on the leading partial is explained in detail in the text.

from the applied shear stress; the 2nd is the tension of the stacking fault formed when the leading partial dislocation b_L glides away from the trailing partial; the 3rd term represents dislocation interactions; and the last term represents Peierls force or friction type of force. F_P^L may be negligible for b_L, typical for isolated partials in fcc metals. A schematic of the forces and their influence on the direction of movement of the leading partial is shown in Fig. 3.3(b). For the trailing Shockley partial situated at the interface, the corresponding Peach-Koehler force can be written as

$$F_T = \tau_{rss} b_T + \gamma_{SF} - F_{b_L b_T} - F_P^T \qquad (3.2).$$

When the separation distance of the paired partials, d_{SF}, increases, the corresponding mechanical work imposed to the system, calculated by $W = F_L d_{SF}$, also increases. In parallel if the trailing partial remains at the interface, the friction force acting on the trailing partial must also increases. Because the stacking fault energy is high for Al [18], 166 mJ/m^2, the separation distance is typically very small (less than 1 nm) under zero applied stress [105 - 107]. Hence the observation of stacking fault in Al is more difficult than in other metals with much lower stacking fault energy. In this study, a separation distance of 2.4 nm is observed inside Al, indicating that the friction stress associated with interfaces poses a strong pinning effect in trapping the trailing partial. Similar phenomena have been observed in nanocrystalline Cu [108] and Al [107, 109 -

112] where grain boundaries exerts a pinning effect to the trailing partial, causing an extend stacking fault and enhancing the possibility of forming deformation twins.

Dislocation annihilation at interfaces is also observed during *in situ* nanoindentation studies. Figs. 3.4(a) - (d) show a series of XTEM snapshots (processed by FFT) at different instants during a continuous loading process. Initially as shown in Fig. 3.4(a), two dislocations, labeled as b_1 at the interface and b_2 slightly away from the interface (inside Nb) are separated at a distance, d_p, of 2.5 nm, and d_p is measured along the direction parallel to the interface. After 2 seconds, d_p decreases to 1.7 nm as depicted in Fig. 3.4(b). The decrease in the separation distance via dislocation climb occurs at an average velocity of 0.4 nm/sec, about two orders of magnitude larger than the climb velocity of a dislocation in bulk Al lattice, 0.001 nm/sec [113]. At 2.5 seconds, the two dislocations annihilate at the interface as shown in Fig. 3.4(c). Besides climb, the dislocation b_2 also glides towards the interface, and consequently the two dislocations lay on the same plane parallel to the interface. Finally, Fig. 3.4(d) shows that the crystal becomes perfect after the annihilation of dislocations at the interface.

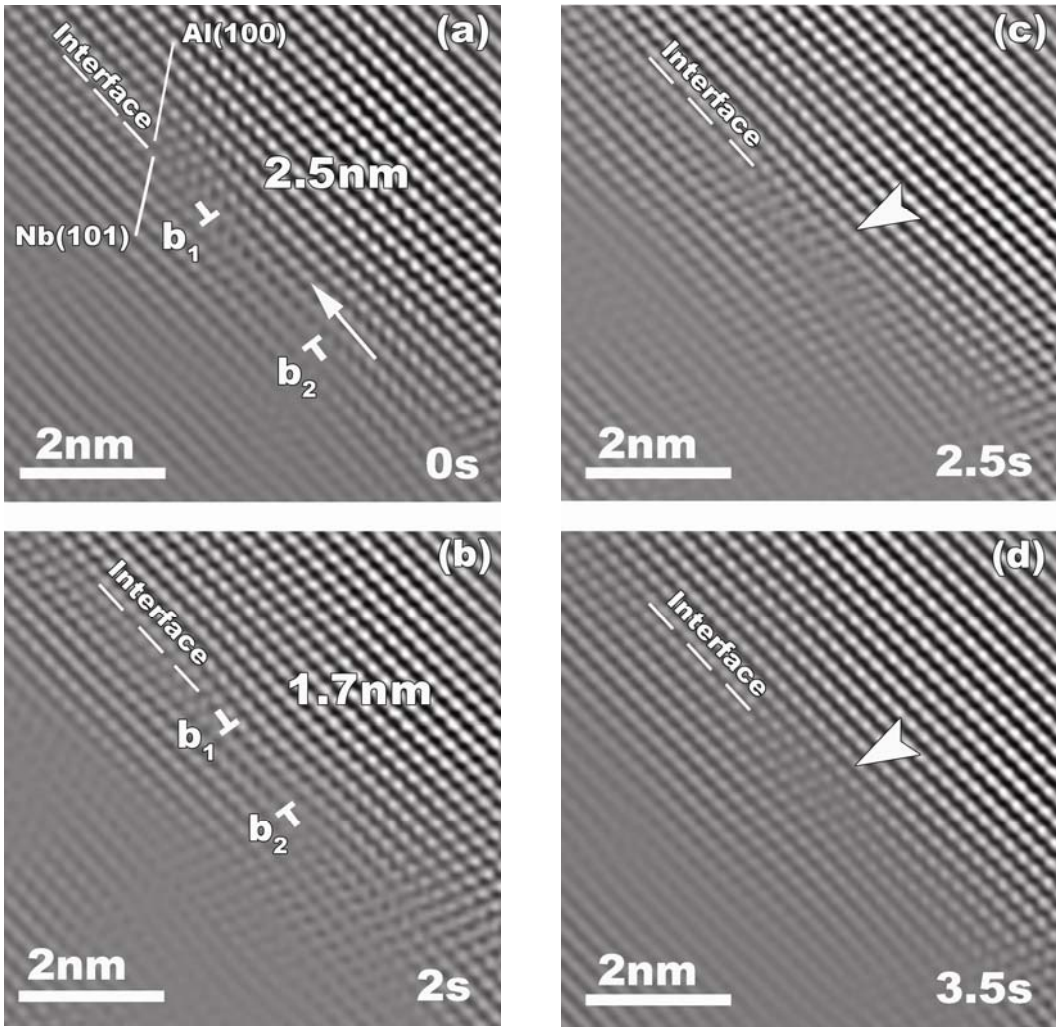

Figure 3.4 HRTEM snapshots of dislocation annihilation process at interface captured at different instants during *in situ* nanoindentation. (a) At 0 sec, the two dislocations are separated by 2.4 nm, (b) After 2 seconds, the separation distance has been reduced to 1.7 nm via climb of the dislocations. (c) At 2.5 seconds the two dislocation annihilate with one another and dislocation b_2 undergoes both climb and glide movement. (d) At 3.5 seconds a perfect crystal is obtained along the interface after the complete annihilation of dislocations.

Dislocation climb is achieved via mass transport, such as vacancy diffusion and/or interstitial diffusion [18, 114]. The dislocation climb velocity, v, can be expressed by [115]

$$v = \frac{2\pi D b^2 [c(R) - c^0]}{\ln(\frac{R}{b})} \quad (3.3),$$

where D is the vacancy diffusivity, c(R) is the vacancy concentration at distance R a way from the jog, c^0 is the concentration maintained in the lattice in equilibrium, and b is the Burgers vector of the dislocation. Since the vacancy diffusivity along interface is much greater than in bulk lattices [116], the velocity of dislocation climb at interfaces should also be greater than that inside lattices. Atomistic simulations of the Cu/Nb interface can accommodate multiple, mutable interface structures [102]. Consequently the vacancy formation energy at the interface is low, and such interface can contain a high vacancy concentration than inside crystal lattices [79], and hence facilitate the climb of dislocations along interfaces. The Al/Nb interface adopts the same KS orientation relation as the Cu/Nb interface, although the atomic arrangement slightly differs from each other. Also, the local perturbation associated with atom removal or insertion spreads out in the region of the interface and it is easy to interact with interfacial dislocations nearby. Hence the Al/Nb interface could maintain a similar capability in storing vacancies. The efficient climb of dislocations observed at Al/Nb interfaces

indicates that the diffusivity and migration rate of vacancies at interface should both be sufficiently high.

3.5 Conclusions

In conclusion, by using *in situ* nanoindentation and HRTEM technique we studied various types of interface-dislocation interactions in Al/Nb multilayer composites. The Al/Nb interfaces can act as strong barriers to the transmission of dislocations, trap dislocations, pose a strong pinning force that leads to the extension of stacking fault in Al, and facilitate dislocation climb and annihilation within interfaces. These interactions will help us to understand the deformation mechanisms enabled by interface at nanometer length scales.

CHAPTER IV

MECHANICAL PROPERTIES OF FE/W INTERFACE – SIZE DEPENDENT STRENGTHENING MECHANISMS IN SPUTTERED FE/W MULTILAYERS WITH INCOHERENT BCC/BCC INTERFACES

4.1 Overview

We investigate the size dependent strengthening mechanisms in sputtered Fe/W multilayers with individual layer thickness, h, varying from 1 to 200 nm. Microstructure analyses reveal that Fe/W has incoherent bcc/bcc interfaces. When h decreases to 10 nm or less, XRD studies show significant lattice distortions, comparing to bulk counterpart, due to the interface constraint. The layer thickness dependent drastic variations of XRD profiles are simulated well by using the Schuller's model. Film hardness increases with decreasing h, and approaches a maximum of 12.5 GPa when h = 1 nm. The layer thickness dependent film hardnesses are compared with analytical models. Koehler's image force plays a dominant role in determining the maximum strength of composites at smaller h. Understanding the influence of interface on strengthening in multilayers will facilitate the design of high strength metallic materials.

4.2 Introduction

Mechanical properties of metallic multilayer films have received significant attention recently because the maximum hardness of some systems can approach the

theoretical strength of the composite [9, 117]. A variety of metallic multilayer systems have been explored in an attempt to construct different type of interfaces to achieve high strength. A majority of these studies focus on system with fcc/fcc type interfaces, such as Cu/Ni, Cu/Ag, Cu/330 austenitic stainless steel [21, 22], and fcc/bcc type interfaces, such as Cu/Nb, Cu/Cr, Cu/W, Fe/Pt [20, 23, 24]. There are very few studies on size dependent strengthening in systems with bcc/bcc type interfaces, such as Fe/Cr, and W/Mo [24, 118]. In general, film hardness increases with decreasing individual layer thickness, h, when h is greater than several tens of nanometers. Strengthening in this regime can be explained well by the Hall-Petch (HP) dislocation pile-up model [119, 120]. When individual layer thickness decreases further, film hardness-layer thickness relation deviates from the prediction of conventional HP model, indicating dislocation pile-ups are less likely. Instead, the Orowan bowing model may predict a more realistic deformation mechanism [8, 37]. At a few nanometer length scales, most multilayer systems reach a maximum hardness (referred to as peak hardness thereafter). In coherent multilayer systems, such as Cu/Ni, peak hardness is dominated by coherency stress, which is proportional to shear modulus and mismatch strain. In system with large elastic modulus mismatch, Koehler stress may prevail [38, 121, 122]. Recently it has been shown by molecular dynamic (MD) simulations that in systems with ‘opaque’ interface (referring to incoherent layer interface separating crystals with discontinuous slip

system), such as Cu/Nb, interface shear strength is lower than that of each constituent [101]. Dislocations are therefore attracted to interface, and significant dislocation core spreading occurs at the "weak" interface [101]. As a result of dislocation core spreading, dislocations lose their singularity, making it every hard to reemit into the opposite constituent. The "weak" interface in Cu/Nb therefore lead to significant strengthening at a few nm length scale. Recent review articles have described the work in this area in considerable detail [26, 31, 32]. In systems with diffuse composition gradient, film hardness may decrease due to intermixing along layer interface [123, 124].

In this study, the size-dependent strengthening mechanisms of an incoherent bcc/bcc system, consisting of a series of Fe/W multilayers, were investigated. Comparisons of peak hardness among Fe/W and several other W-based multilayers have been made to understand the influence of interface on peak strength of multilayers. This study will provide more insight to the understanding of mechanisms that may lead to high strength in metallic multilayers with bcc/bcc type interface.

4.3 Experimental

Fe/W multilayers were deposited by the magnetron sputtering technique at room temperature on SiO_2 substrates. The vacuum chamber was evacuated to a base pressure less than 5×10^{-8} torr prior to deposition. The constituents within the multilayers have equal individual layer thickness, h, varying from 1 to 200 nm. The total film thickness

was about 2 μm for all multilayers. Hence the number of bilayers varies from 5 for Fe 200nm/W 200 nm (referred to as Fe/W 200nm thereafter) to 1000 for Fe/W 1nm multilayers. Single layer, 2 μm-thick Fe and W films were sputter-deposited by using the same technique. Transmission electron microscopy (TEM) was performed on JEOL 2010 operated at 200 kV. High-resolution TEM (HRTEM) experiments were performed on a JEOL 3000F microscope operated at 300 kV. Scanning transmission electron microscopy (STEM) was performed on FEI Tecnai G2 F20 FE-TEM with an imaging resolution of 0.23 nm, and a nanoprobe size of a few nm was used for energy dispersive x-ray spectroscopy (EDX) analysis. X-ray diffraction (XRD) experiments were performed on Bruker-AXS D8 VARIO high-resolution x-ray diffractometer. The hardness and elastic modulus of multilayers were measured, at room temperature, by using instrumented nanoindentation technique via a Fischerscope HM2000XYp micro/nanoindentor with Vickers indenter tip. During nanoindentation, the indentor penetrates to a maximum indentation depth of approximately 1/10 of the total film thickness to accurately determine the hardness of films while avoid the substrate effect. An indentation depth of 75 - 250 nm. A minimum of nine indents were performed on each specimen to get an average hardness value at various indentation depth. A plateau of hardness vs. indentation depth is typically achieved. The curvature of the substrate was measured before and after deposition using the laser scanning technique [125, 126],

and the stress was calculated using the Stoney equation [127].

4.4 Results

XRD patterns of as-deposited Fe/W multilayers are shown in Fig. 4.1. When h decreases from 100 to 10 nm, as shown in Fig. 4.1(a), the relative peak intensity of W (110) and Fe (110) becomes stronger, indicating stronger textures along these orientations. Fig. 4.1(b) shows the XRD pattern of multilayers with smaller h, 1 to 5 nm. Significant lattice distortions from classical bcc structures are observed in both Fe and W in these fine nanolayers. The influence of h on the evolution of XRD profiles and superlattice peaks will be discussed in detail later. For comparison, XRD patterns of pure Fe and W films are also shown in the figure. Both Fe and W possess typical BCC structure (α phase), and the lattice parameter for coarse-grained Fe and W is 2.866 and 3.164 Å, respectively.

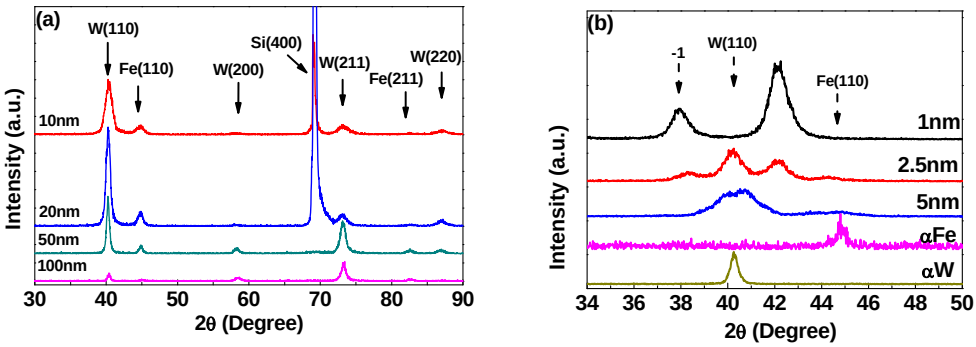

Figure 4.1 XRD patterns of sputtered Fe/W multilayer films with different individual layer thickness, h. (a) When h decreases from 100 to 10 nm, the W (110) and Fe (110) textures become stronger. (b) Comparisons of XRD patterns among multilayers with h = 1- 5 nm and pure Fe and W film. Both single layer Fe and W films have BCC structure.

The microstructures of single layer Fe and W films were examined by plan-view TEM experiments. Fig. 4.2 shows the plan-view TEM micrograph of single layer Fe and W film. The average grain size is about 200 nm in W, and 30 nm in Fe film. The microstructures of multilayer films are corroborated by examining cross-sectional TEM (XTEM) micrographs. XTEM micrographs of Fe/W 5 nm and 50 nm multilayers reveal relatively clear interfaces as shown in Fig. 4.3. Inserted selected area diffraction (SAD) pattern of Fe/W 5 nm, shown in Fig. 4.3(a), indicates a {110} fiber texture in both Fe and W. HRTEM micrograph of interface of Fe/W 5 nm multilayers shown in Fig. 4.3(b) indicates little intermixing along interfaces. Meanwhile, STEM image of Fe/W 5 nm multilayers is provided in Fig. 4.3(c) to show the chemically distinguishable interface

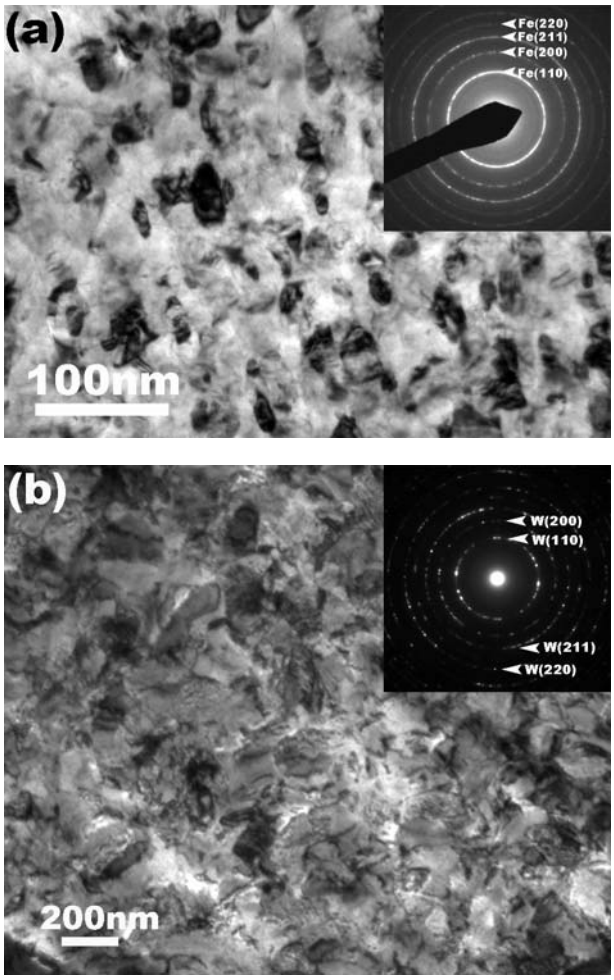

Figure 4.2. (a) A plan-view TEM micrograph and the inserted select diffraction pattern (SAD) of single Fe film show nanocrystalline grains with an average grain size of ~ 30 nm. (d) A plan-view TEM micrograph and its SAD show that the single layer W film has an average grain size of ~ 200 nm.

between Fe and W. Correspondingly a weak texture is observed in Fe/W 50 nm multilayers, as shown in Fig. 4.3(d). Fig. 4.4(a) shows the XTEM image of Fe/W 1 nm multilayer. The film shows columnar grains with an average grain size of ~ 20 nm. Multilayers have convex shape indicating the generation of compressive stress in films during growth process. The magnitude of compressive stress is determined to be ~ 1 GPa

by using the curvature measurement technique. Voids are also observed along columnar grain boundaries. Fig. 4.4(b) shows the corresponding SAD pattern of Fe/W 1 nm film. The diffraction pattern of Fe (110) and W (110) can not be distinguished, similar to the

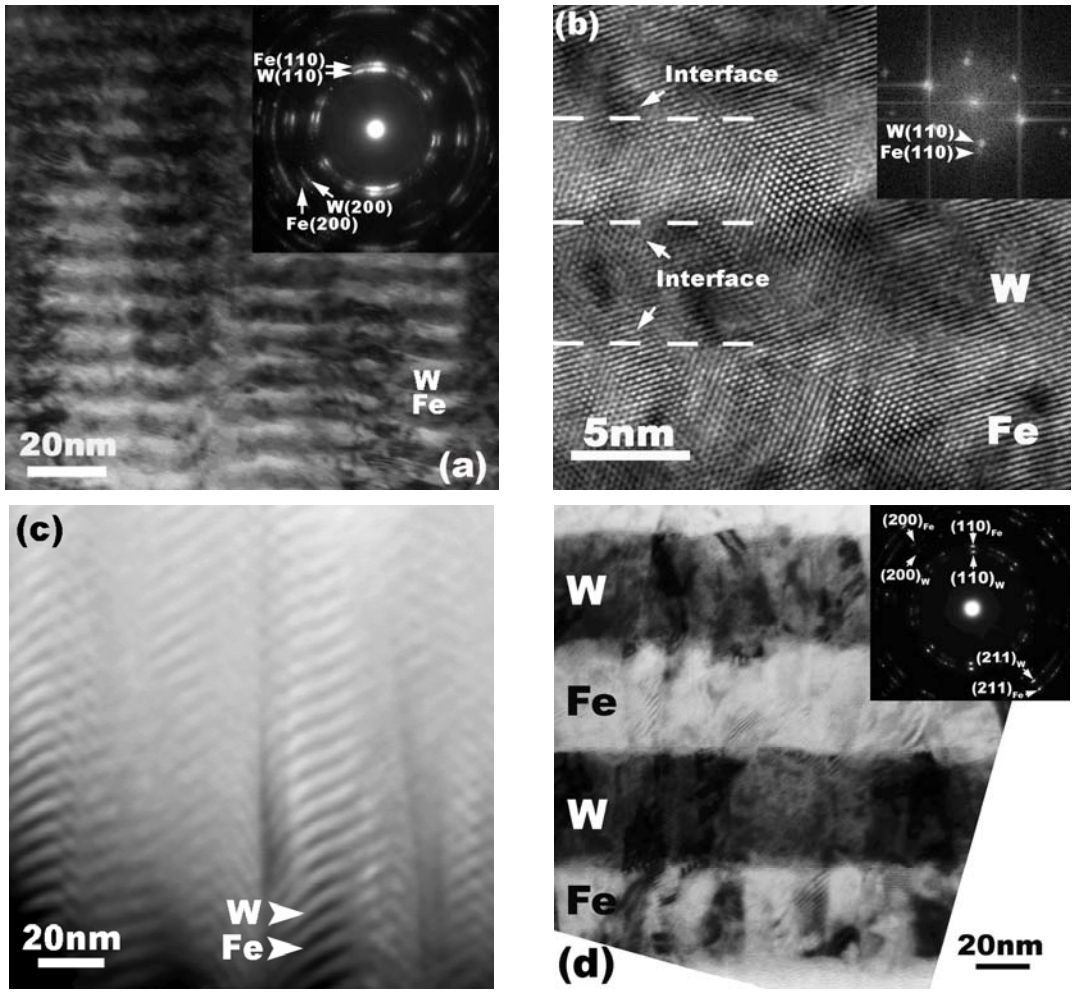

Figure 4.3 (a) XTEM micrograph of as-deposited Fe/W 5 nm multilayer films shows distinct layer interface and the inserted SAD pattern shows strong Fe (110) and W (110) texture. (b) HRTEM micrograph of interface of Fe/W 5 nm multilayers indicates little intermixing along interfaces. (c) STEM image of Fe/W 5 nm multilayers shows the chemically distinguishable interface between Fe and W. (d) XTEM micrograph of Fe/W 50 nm multilayer films with geometrically abrupt layer interfaces.

observation of a single peak (the right most peak) in XRD studies shown in Fig. 4.1(b). HRTEM image of Fe/W 1 nm nanolayers, Fig. 4.4(c), shows that the {110} atomic planes of Fe and W are closely matched across layer interface, and in some places misfit dislocations (primarily in Fe) are observed along the layer interfaces.

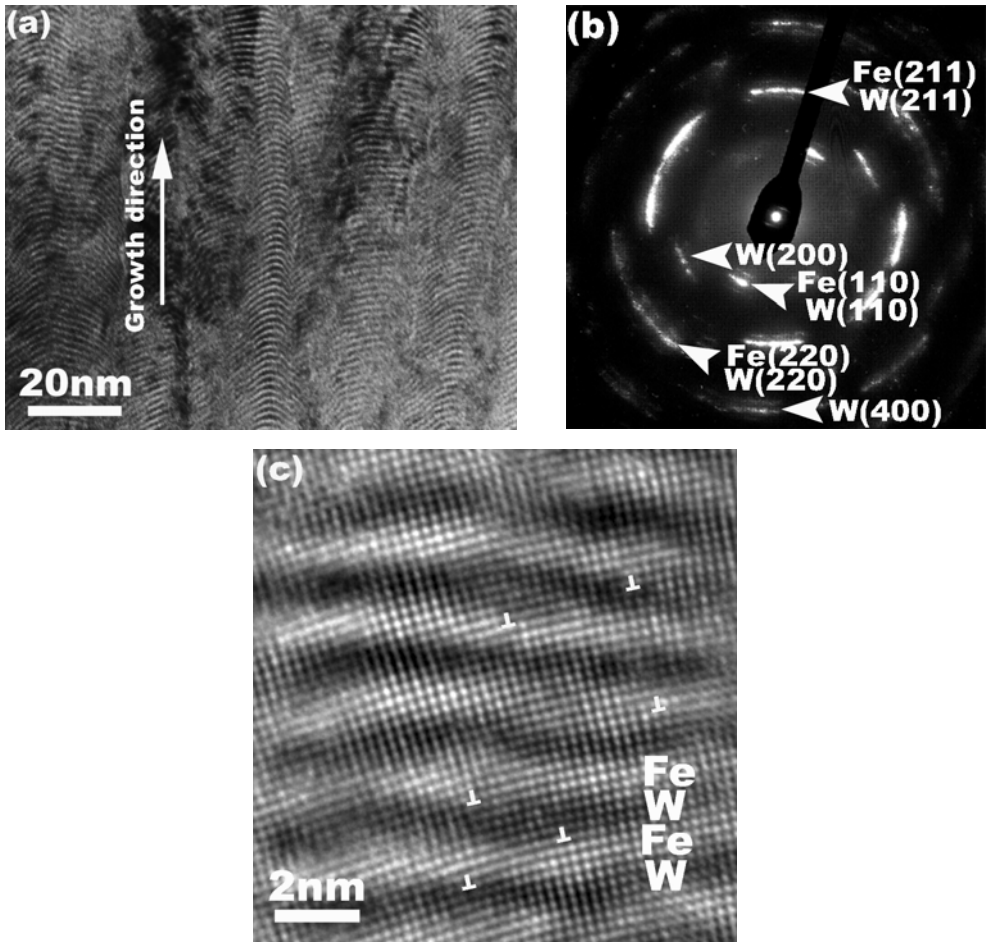

Figure 4.4. (a) XTEM micrograph of Fe/W 1 nm multilayers with clear layer interfaces. (b) The corresponding SAD pattern shows the overlap of a majority of Fe and W diffraction pattern, such as Fe and W (110), and Fe and W (211) diffraction rings. (c) HRTEM image, examined along Fe (W) <100> zone axis, shows semi coherent Fe/W interface with few misfit dislocations along the Fe/W interfaces.

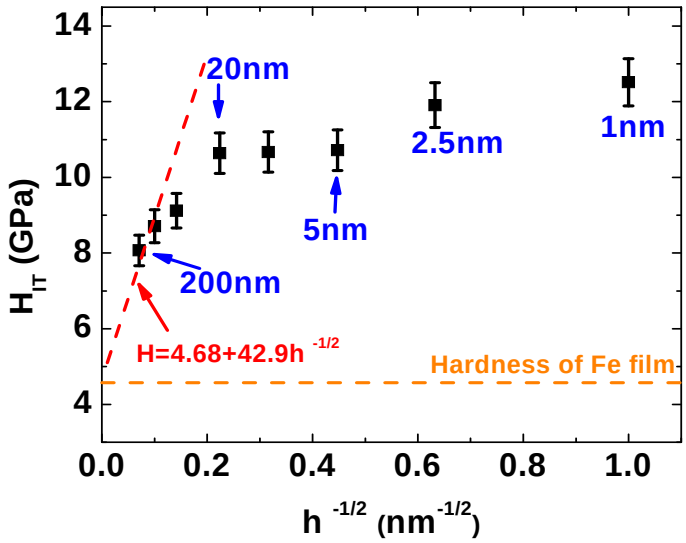

Figure 4.5 Indentation hardness (H_{IT}) of Fe/W multilayer films is plotted vs. $h^{-0.5}$, where h is the thickness of each individual layer. Hardness increases with decreasing layer thickness. The hardness of multilayers with layer thickness of greater than 50 nm is delineated by a dash line. The rule-of-mixture hardness and Fe hardness are shown as horizontal dash lines.

The indentation hardness of Fe/W multilayer films, H_{IT}, tested by nanoindentation technique is plotted as a function of $h^{-1/2}$, in Fig. 4.5. When h > 50 nm, the hardness of multilayer films scales approximately linearly with $h^{-1/2}$, following a traditional Hall-Petch relationship, i.e.,

$$H_{IT} = H_0 + kh^{-\frac{1}{2}} \qquad (4.1).$$

where H_{IT} is indentation hardness, H_0 is film hardness at infinitely large grain sizes, representing the overall resistance of the crystal lattice to dislocation movement, and k is the Hall-Petch slope, measuring the relative hardening contribution from layer interfaces. Since the hardness of 2 μm thick singl layer Fe film is ~ 4.6 GPa, as shown by the

horizontal dash line, and it is lower than that of 2 μm thick W films, ~ 8.8 GPa, we assume that the Hall-Petch strengthening in multilayers may be determined by dislocation pile-ups in the soft Fe layer. Plastic yielding occurs when dislocations in Fe transmit across layer interfaces. A linear fit of the experimental data (hardness of single layer Fe, Fe/W 200 nm, and Fe/W 100 nm), indicated by the dash line in the plot, yields H_0 = 4.68 GPa and k = 42.9 GPa·nm$^{0.5}$. As h decreases further, the film hardness increases nonlinearly, and reaches a maximum hardness of 12.5 GPa at h = 1 nm.

4.5 Discussions

4.5.1 Microstructure of Fe/W multilayer films

Both XTEM and XRD experiments indicate that when h ≥ 10 nm, film has a stronger Fe and W {110} fiber texture at smaller layer thickness. Further reduction of h leads to a gradual evolution of peak position and the appearance of probable satellite peaks due to the formation of nanolayer superlattices. When h decreases to 1 nm, two peaks appear at positions distinctly different from that of bulk W (110) and Fe (110) peaks as shown in Fig. 4.1(b). This evidence could lead to the misconception that new phases have been formed in Fe and W. For instance, the peak position of 2θ = 42.1^o corresponds to ε-Fe with hcp structure. However, it is known that ε-Fe exists only under very a very high pressure, ~ 10 GPa [128, 129].

To understand the influence of interface constraint on x-ray profiles, we attempt to

simulate the X-ray diffraction pattern in nanolayers by considering three characteristic length scales as proposed in the Schuller's model [88], (i) bilayer thickness, Λ ($\Lambda = 2h$), (ii) the inter planar spacing of constituents, and (iii) the structural coherency length, ξ, which is the distance over which atomic positions are quantitatively correlated, and it can be estimated from the full width half maximum (FWHM) by using the Scherrer's equation.

The influence of interfacial constraint on lattice parameter of multilayers is more significant at smaller h [88, 89]. Hence we would anticipate greater magnitude of evolution of peak positions as shown in Fig. 4.1(b). When ξ is larger than Λ, the peak position can be indexed by [88]:

$$\frac{2\sin\theta}{\lambda_x} = \frac{1}{\bar{d}} \pm \frac{n}{\Lambda} \qquad (4.2).$$

where λ_x is the wavelength of x-ray, n is satellite order, $\bar{d}$ is the average lattice constant, and is equal to ½ ($d_{Fe(110)} + d_{W(110)}$). For Fe/W 1 nm multilayer, based on the FWHM and peak position maxima of the right most peak in Fig. 4.6(a), ξ is calculated to be ~ 107 Å, $\bar{d}$ is determined to be 2.14 Å, close to the average bulk value of $d_{Fe(110)}$ and $d_{W(110)}$, which is 2.13 Å. The left most peak is a satellite peak originated from superlattices. From the separation of satellite (left) and diffraction peak (right), we obtained Λ = 22 Å, which is consistent with the bilayer thickness determined by XTEM studies. SAD pattern of the Fe/W 1 nm multilayer also shows the overlap of Fe and W

{110} diffractions, consistent with the existence of single peak (left) in XRD analysis. Furthermore HRTEM micrograph of Fe/W 1 nm multilayers shows the formation of "semi-coherent" Fe/W interface with the existence of few misfit dislocations at interfaces. The existence of minus satellite peak alone in Fe/W 1nm film indicates that both an amplitude and a phase modulation are present [130].

For Fe/W 2.5 nm multilayer, ξ is calculated to be ~ 86 Å based on FWHM of the diffraction peak (labeled as 2.14 Å in Fig. 4.6(b)), larger than Λ, and hence Eq. 4.2 is still applicable. The third-to-the-left diffraction peak in Fig. 6b has an average d spacing of Fe (110) and W (110), 2.14 Å. There are two first order satellite peaks (due to the superlattice structure) located symmetrically around the peak with a d-spacing of 2.14 Å. The +1 satellite peak overlaps with the Fe (110) peak, while the -1 satellite peak overlaps with the W (110) peak as shown in Fig. 4.6(b). The left most peak is the second order satellite peak (labeled as -2) of the superlattice. From the separation of satellite peaks, we obtain Λ of 48 Å.

The aforementioned superlattice peak positions, calculated based on Eq. 4.2 agree qualitatively with experimental observations of peak positions. Notice that there is no adjustable parameter in fitting the peak positions. Now we simulate the x-ray diffraction pattern of Fe/W multilayers by using the Schuller's model, expressed by: [89].

$$I \propto \frac{1+\cos^2 2\theta}{\sin\theta \sin 2\theta}\left|\begin{Bmatrix}\sum_{j=1}^{n}\exp[-W_{Fe}(\frac{\sin\theta}{\lambda_x})^2 f_{Fe}(\theta)\rho_{Fe}\exp(i\frac{4\pi}{\lambda_x}x_j\sin\theta)] \\ +\sum_{j=1}^{m}\exp[-W_W(\frac{\sin\theta}{\lambda_x})^2 f_W(\theta)\rho_W\exp(i\frac{4\pi}{\lambda_x}x_j\sin\theta)]\end{Bmatrix}\right|^2 \quad (4.3).$$

where $1 + \cos^2 2\theta$ is the polarization factor, $\sin 2\theta$ is the Lorentz factor, $\sin\theta$ is a geometric factor, f_{Fe} and f_W are the atomic scattering function of Fe and W. ρ_{Fe} and ρ_W are in-plane atomic density, which is 0.172 atom/Å^2 for Fe (110) plane, and 0.141 atom/Å^2 for W (110) plane. W_{Fe} and W_W are the corresponding Debye-Waller factors, and they are 0.26 for Fe and 0.15 for W. x_j is the position of the jth atomic plane, n is the number of Fe plane in one layer and m is the number of W plane in one layer, λ_x is the wavelength of X-ray. The atomic scattering function is given by [131],

$$f(s) = Z - 41.78214 \times s^2 \times \sum_{i=1}^{N} a_i \exp(-b_i s^2) \quad (4.4).$$

where $s = \sin\theta/\lambda_x$, Z is the atomic number, a_i and b_i are materials dependent coefficients and N is the number of terms in the summation. The only adjustable parameter (to fit XRD profile) is the number of atomic planes. Fig. 4.6 (a)-(d) shows comparisons of simulations and experimental XRD profiles of Fe/W multilayers with h of 1 - 10 nm. Overall the simulations has correctly captured major characteristics of X-ray profiles, including peak positions, relative peak intensity, peak broadening and line shape.

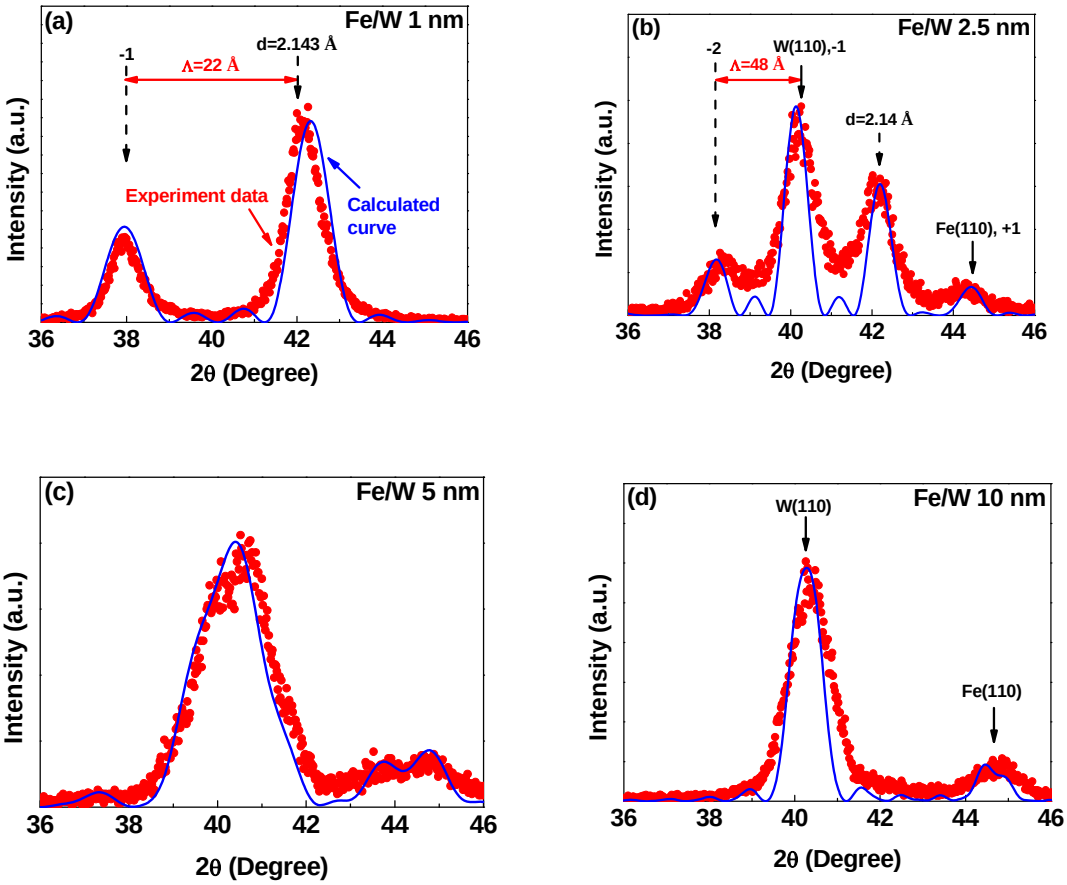

Figure 4.6 (a) – (d) Comparisons of analytical model described in text and experimental XRD results for h = 1, 2.5, 5, and 10 nm. The model captures the major characteristics of XRD profiles, in terms of peak position, superlattice, and FWHM etc., in most cases.

The simulations suggest that the evolution of lattice spacing is due to the interfacial constraint originating from a large lattice mismatch between Fe and W (110) planes, ~ 10 %. Hence our simulations and microstructural analyses support that the evolution of lattice spacing occurs as a result of interface induced constraint, and there is little evidence for the formation of ε-Fe.

4.5.2 Mechanical properties – hardening from the Fe/W interface

We will first examine the Hall-Petch strengthening mechanism at greater h (h > 50 nm). The elastic modulus of Fe, 200 GPa, is half of that of W, 400 GPa. Hence in multilayers with h on the order of tens of nm or greater, dislocation pile-ups should occur within the softer constituent, Fe, and when the stress concentration approaches critical values, dislocation will glide across layer interface into W layers, i.e., yielding occurs. Therefore we will model the strengthening mechanisms in the dislocation pile-up regime by using the individual layer thickness as obstacle spacing. According to the Hall-Petch dislocation pile-up model, the Hall-Petch slope, k, is expressed by [34, 37]

$$k = \sqrt{\frac{\tau^* \mu b}{\pi(1-\nu)}} \qquad (4.5).$$

where τ^* is the critical interface barrier shear stress, μ is the shear modulus of composites, b is the Burgers vector and ν is the Poisson's ratio. By using the average shear modulus of composites, ~120 GPa, b = 2.6 Å, ν = 0.3, and the Hall-Petch slope k = 42.9 GPa·nm$^{0.5}$ to be divided by a Taylor factor of 3.1 [132] and a Schmid factor of 2.7, we obtain $\tau^* \approx 1.9$ GPa. The τ^* should correspond to the critical shear stress needed to push a single glide dislocation across the Fe/W interface. Note that a lower bound theoretical strength limit of Fe/W multilayers can be estimated as $\mu/30$. Taking the average shear modulus of composites, we obtain that $\mu/30 \approx 4$ GPa. Hence our calculated τ^* for Fe/W is within a factor of two of the lower bound of the theoretical

limit.

The Hall-Petch slope, k, which is a measure of interface barrier strength for slip transmission, can also be estimated analytically as [133]

$$k = 0.18\mu\sqrt{b} \tag{4.6}.$$

where μ and b should be the parameters of the stiffer component of the multilayers, W. By using μ_W = 156 GPa, and b_W = 2.74 Å, we arrive at k = 14.7 GPa · $nm^{0.5}$. Considering the Taylor factor of 3.1, the calculated sloped is then ~ 45.6 GPa · $nm^{0.5}$, slightly greater than the measure value, 42.9 GPa·$nm^{0.5}$.

Second, we attempt to estimate hardness of multilayers by using the Chu-Barnett model [44]. This model considers the modulus difference of the constituents, dislocation core effect and finite width of layer interface. If there are sufficient dislocations already available within the layers, a lower bound resolved shear stress, τ_l, can be estimated by

$$\tau_l(h) = \tau_0 + \frac{\alpha_1 b\cos\theta}{h}(\mu_{Fe} + \mu_W)\ln(\frac{h}{b\cos\theta}) \tag{4.7}.$$

On the other hand, if the generation of dislocations is required, then an upper limit of resolved shear stress, τ_u, should be used and can be written as

$$\tau_u(h) = \tau_0 + \frac{2\alpha_1 b\cos\theta}{h}(\mu_{Fe} + \mu_W)\ln(\frac{h}{2b\cos\theta}) \tag{4.8}.$$

α_1 is $\frac{1}{4\pi}$ for screw dislocations, and $\frac{1}{4\pi(1-\nu)}$ for edge dislocations, where ν is the Poisson's ratio. θ is the smallest angle between the interface and the glide planes of the crystal. τ_0 is the average shear stress required for slip in homogenous material. The

rule-of-mixture hardness of composites is 6.7 GPa. By using the shear modulus of Fe and W, b = 2.6 Å, $\alpha_1 = \frac{1}{4\pi}$, θ = 60º between two (110) plane, and using a Taylor factor of 3.1, and a Schmid factor of 2.7, we calculated the upper and lower bound of resolved shear stresses as shown in Fig. 4.7. The model describes the thickness dependent hardness of multilayers well when h ≥ 50 nm. However, the model overestimates the hardness of multilayers at smaller h, indicating that different strengthening mechanisms operate at smaller layer thicknesses.

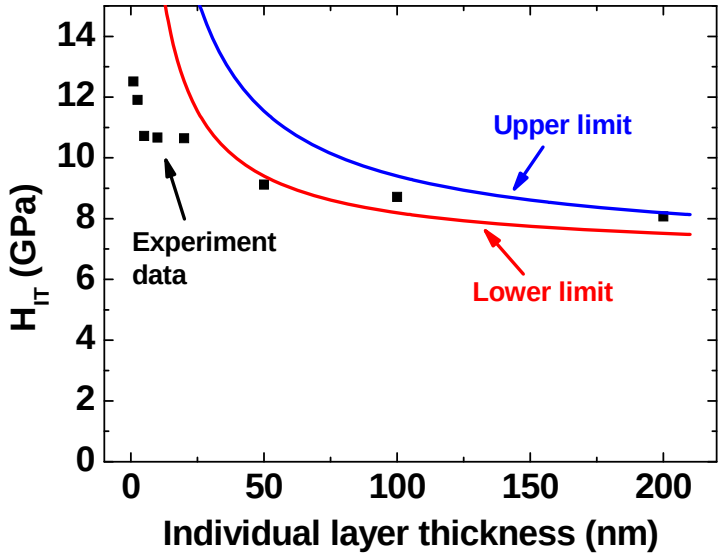

Figure 4.7 Simulation of layer thickness dependent film hardness of multilayers by using the upper and lower bound of calculations based on Chu-Barnett model described in text. The analytical model fits the hardness results better at larger layer thickness, but overestimates the hardness at smaller h.

Third, we will estimate the hardness of multilayer films at a few nm length scales. In numerous multilayers systems, the hardness of multilayers typically approaches a peak value (saturation) at h of a few nm length scales. In this study, the hardness of Fe/W increases monotonically, and exceeds 12 GPa when h is a few nm. At a few nm length scales, if the constituents of multilayers have rather significant difference in elastic modulus, Koehler stress due to the existence of image force of dislocations may create significant barrier to the transmission of single dislocations [38]. Specifically, given a large elastic modulus difference in multilayer systems, the resolved shear stress, $\tau_{r,}$ required to drive the dislocation to within the interface can be expressed by [38]

$$\tau_r = bR\mu_{Fe} \sin\theta / 4\pi h_r \qquad (4.9).$$

where b is the Burgers vector, $R = (\mu_W - \mu_{Fe}) / (\mu_{Fe} + \mu_W)$, h_r is the distance of dislocation from interface, and θ is the smallest angle between the interface and the glide planes of crystal with lower elastic constants. When the distance of the dislocation to the interface is equal to the core radius $h_r \approx 2b$, a maximum resolved shear stress, τ_r^{max}, is achieved. Using the shear modulus of Fe and W, and θ = 60º between two (110) plane, τ_r^{max} in Fe/W system is calculated to be ~ 0.9 GPa. Considering a Taylor factor of 3.1, and a Schmid factor of 2.7, we estimate that the enhancement of film hardness due to image force is ~ 7.5 GPa. The peak hardness of Fe/W multilayer films shall therefore be approximately the sum of rule-of-mixture hardness and the Koehler's image force,

approximately 14 GPa, close to the experimental value of 12.5 GPa for h = 1 nm. Such analysis indicates that the peak hardness in Fe/W multilayer films is dominated by Koehler stress due to a large mismatch in elastic modulus of Fe and W. Coherency stress due to small lattice mismatch should be insignificant in this case, because the lattice mismatch between Fe and W is approximately 10%, too large to be accommodated coherently along layer interface. In fact, as shown in Fig. 4.4(c), misfit dislocations were observed along the Fe/W interface when h = 1 nm, and they could relieve coherency stress considerably.

Finally we will compare the mechanical properties of several W based metallic multilayer systems, including Fe/W, Cu/W and Mo/W. Table 4.1 lists elastic moduli, lattice parameters and crystal structures of layer constituents. Table 4.2 provides average elastic modulus, peak hardness and lattice mismatch for these multilayer systems. In W based multilayers, since the modulus of W is much higher than the other component, Koehler stress induced strengthening is one of the major mechanisms to increase the peak hardness of multilayers. But for Mo/W multilayers, because of their small lattice mismatch, ~ 0.4%, significant coherency stress arises at small layer thickness. Both Koehler stress and coherency stress lead to much pronounced peak hardness in Mo/W multilayer system. Whereas in Fe/W system, peak hardness is mainly dominated by Koehler stress. In Cu/W multilayers, a supermodulus effect is observed when layer

thickness decreases [23]. However, we did not observe significant modulus change as a functional of layer thickness in Fe/W multilayers. The greater peak hardness of Fe/W than that of Cu/W could be a result of higher average biaxial modulus in Fe/W system.

Table 4.1 Modulus and crystal structure of metallic materials

Metal	Elastic Modulus (GPa)	Shear Modulus (GPa)	Lattice parameter (Å)	Crystal Structure
Fe	200	78	2.866	BCC
W	400	156	3.164	BCC
Mo	275	120	3.15	BCC
Cu	110	46	3.61	FCC

Table 4.2 A comparison of peak hardness of several multilayers

System	Average elastic modulus (GPa)	Peak hardness (GPa)	Lattice mismatch * (%)
Fe/W	300	12.5	9.9
Cu/W	255	8.9	7.0
Mo/W	338	19.4	0.4

* Calculated according to fcc {111} // bcc {110}, bcc {110} // bcc {110} interplanar spacing

4.6 Conclusions

Sputter-deposited Fe/W multilayer films with individual layer thickness greater than 10 nm have incoherent bcc/bcc type interfaces, and distorted Fe and W crystal

structures are observed at smaller individual layer thickness. The significant evolution of XRD profiles at smaller individual layer thickness is simulated well by using the Schuller's model, indicating strong constraints along layer interfaces. High resolution TEM studies reveal that layer interface in Fe/W 1 nm is semi-coherent with a few misfit dislocations at layer interfaces. The evolution of film hardness at greater layer thickness is simulated by using the Chu and Barnett model. The interface barrier strength estimated from Hall-Petch slope indicates that the Fe/W interface is a strong barrier to the transmission of dislocations. A maximum film hardness of 12.5 GPa is achieved when the individual layer thickness decreases to 1 nm. Koehler stress due to a large elastic modulus difference between Fe and W appears to be the major mechanism for determining the peak hardness in Fe/W multilayers.

CHAPTER V

HE ION IRRADIATION TOLERANCE OF AL/NB (FCC/BCC) INTERFACE*

5.1 Overview

We investigated the evolution of microstructure and mechanical properties of sputter-deposited Al/Nb multilayers with individual layer thickness, h, of 1-200 nm, subjected to helium ion irradiations: 100 keV He^+ ions with a dose of $6\times10^{16}/cm^2$. Helium bubbles, 1-2 nm in diameter, were observed. When h is greater than 25 nm, hardnesses of irradiated multilayers barely change, whereas radiation hardening is more significant at smaller h. Transmission electron microscopy and scanning transmission electron microscopy studies reveal the formation of a thin layer of Nb_3Al intermetallic along the Al/Nb interface as a consequence of radiation induced intermixing. The dependence of radiation hardening on h is interpreted by using a composite model considering the formation of the hard Nb_3Al intermetallic layer.

5.2 Introduction

In general heavy ion irradiation of crystalline metallic alloys can cause dramatic variations, including amorphization or phase change [51]. Radiation with lighter ions, such as helium (He), can induce a large number of point defects as a consequence of

*Reprinted with permission from "He ion irradiation damage in Al/Nb multilayers" by N. Li, M.S. Martin, O. Anderoglu, A. Misra, L. Shao, H. Wang, X. Zhang, 2009, Journal of Applied Physics, 105, 123522, Copyright [2010] by American Institute of Physics.

nuclear collisions, including vacancies and interstitials, and defect clusters, such as He bubbles, voids and dislocation loops [134 - 136]. Interplay of these defects can eventually lead to swelling [137 - 140], blistering of metal surfaces [141], and radiation embrittlement [142]. Hence particle irradiation has deleterious effects on the mechanical integrity and dimensional stability of structural metals and reduces their service time in nuclear reactors. Understanding the mechanisms of radiation induced damage in metallic materials is of great significance and could potentially lead to the discovery and development of radiation tolerant materials. Under this context, a unique approach has recently been proposed, i.e., to study layer interface mitigated radiation damage in metallic multilayers [19, 143 - 146]. The anticipation of enhanced radiation tolerance in metallic nanolayers is based on the following rationale: interfaces act as sinks for radiation induced point defects and external species (such as He), and the enhanced diffusivity of point defects along interfaces could promote rapid recombination of unlike point defects, and result in radiation tolerance superior to conventional single-phase bulk metals [19, 143 - 146]. Such concept has been tested in Cu/Nb multilayer system. The study shows that room temperature irradiated (He ions at 33 keV and a total flux of $1.5 \times 10^{17}/cm^2$) Cu/Nb multilayers with 4 nm individual layer thickness do not exhibit blistering upon annealing at 600 ºC, whereas blistering is observed in single layer Cu or Nb, and Cu/Nb multilayers with 40 nm individual layer thickness [144]. In parallel, our

recent studies on Cu/V and Fe/W multilayers have shown that void swelling as well as radiation hardening have been significantly suppressed in these fine multilayers [146, 147].

In this paper, we investigate radiation damage in Al/Nb multilayers for the following purposes. First, Al/Nb has a unique fcc/bcc interface, where the interatomic spacing of Al (111) is essentially the same as that of Nb (110), whereas the mismatch between Cu (111) and V (110) is approximately 2.3%, and the mismatch is 11.2% in the case of Cu and Nb. Second, Al-Nb is a chemically miscible system with a negative heat of mixing of -18 J/mol [80], distinctively different from that of immiscible Cu/V, 5 J/mol [80] and Cu/Nb 3 J/mol [80]. Hence the strength of Al-Nb interatomic bond at interface should be stronger than that of Al-Al and Nb-Nb bonds. Both characteristics imply that interactions of radiation induced point defects with Al/Nb interface could be largely different than those in Cu/V and Cu/Nb system. Finally the microstructure and mechanical properties of as-received Al/Nb systems have been studied systematically, providing a base line for studying He ion irradiation induced damage in Al/Nb multilayers [148]. In this study, we reveal the retention of layer morphology in Al/Nb multilayers after significant He ion irradiation damage. Radiation hardening mechanisms due to the formation of Nb_3Al along layer interface and other defects are discussed.

5.3 Experimental

Al/Nb multilayers were deposited by magnetron sputtering at room temperature on SiO_2 substrates. The vacuum chamber was evacuated to a base pressure less than 5×10^{-8} torr prior to deposition. The constituents within the multilayers have equal layer thickness, varying from 1 to 200 nm. The total film thickness was about 2 μm. After deposition, films were implanted at room temperature with 100 keV He^+ ions to a dose of $6\times10^{20}/m^2$. The beam current is around 6 microamperes, and the temperature rise of the sample stage is around 50^oC during implantation. Transmission electron microscopy (TEM) and high resolution transmission electron microscopy (HRTEM) were performed on JEOL 2010 and JEOL 3000F microscopes operated at 200 and 300 kV, respectively. Selected area diffraction studies were performed with an aperture of 100 nm in diameter. Scanning transmission electron microscopy (STEM) was performed on FEI Tecnai G2 F20 FE-TEM with an imaging resolution of 0.23 nm, and a nanoprobe size of a few nm was used for energy dispersive x-ray spectroscopy (EDX) analysis. X-ray diffraction (XRD) experiments were performed on Bruker D8-Focus Bragg-Brentano x-ray diffractometer. The hardness and elastic modulus of multilayers before and after irradiation were measured, at room temperature, by Fischerscope HM2000XYp with Vickers indenter at an indentation depth down to 250 nm. A minimum of nine indents were performed at the same depth on each specimen to get an average hardness value.

5.4 Results

5.4.1 Microstructural evolution of He ion irradiated Al/Nb multilayers

Cross-sectional TEM (XTEM) images, in Fig. 5.1, reveal the microstructure of as-deposited Al 5 nm/Nb 5 nm (referred to as Al/Nb 5nm thereafter), and Al/Nb 50 nm multilayers. As-deposited multilayers have chemically abrupt layer interfaces with columnar grains sizes comparable to or greater than individual layer thickness, h. The inserted selected area diffraction pattern (SAD) indicates a strong Al {111} and Nb {110} fiber texture. Given the essentially identical interatomic spacing of Al {111} (0.2338 nm) and Nb {110} (0.23378 nm), the diffraction spots of the two can not be distinguished. High resolution TEM (HRTEM) micrograph of Al/Nb, shown previously [148], confirms the Kurdjumov-Sachs (K-S) orientation relationship along Al/Nb layer interfaces, i.e. Al {111} // Nb {110} and Al <110> // Nb <111>.

SRIM [149] calculation of He ion-irradiations was performed on Al/Nb multilayers with a nominal layer thickness of 50 nm. Fig. 5.2 shows the variation of He concentration versus implantation depth. The simulation predicts that peak He concentration, 5-6 at.%, occurs at approximately 400 nm underneath the surface, with a peak displacement per atom (DPA) of ~ 5.

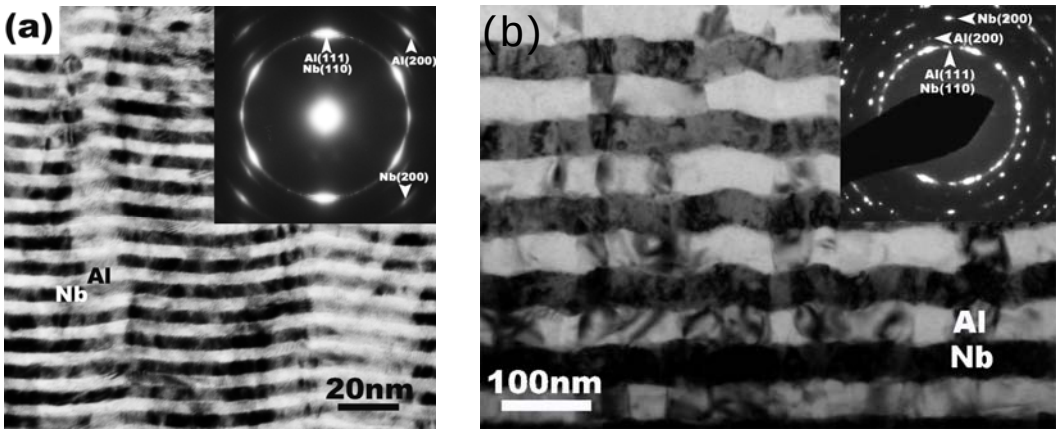

Figure 5.1 XTEM micrographs of as-deposited (a) Al/Nb 5nm multilayer films with Kurdjumov-Sachs orientation relationship between bcc Nb and fcc Al grains, and (b) Al/Nb 50nm multilayers with column grain size of less than 100 nm.

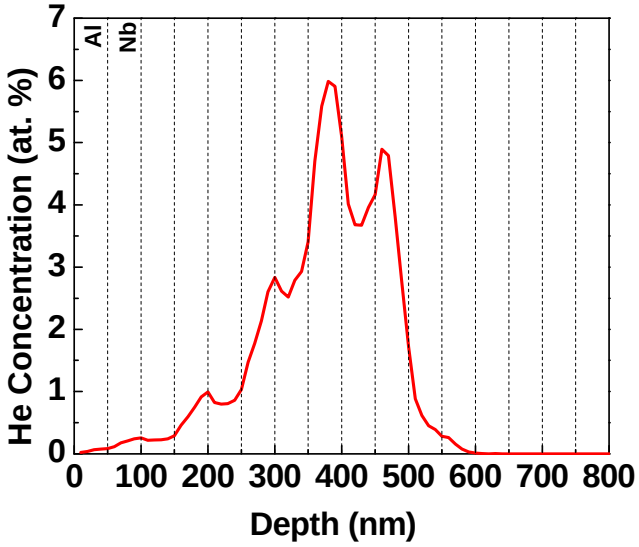

Figure 5.2 A SRIM calculation simulates the variation of He concentration versus radiation depth for He ions of 100keV and flux of $6\times10^{16}/cm^2$, same as the experimental condition, in Al/Nb 50 nm multilayers.

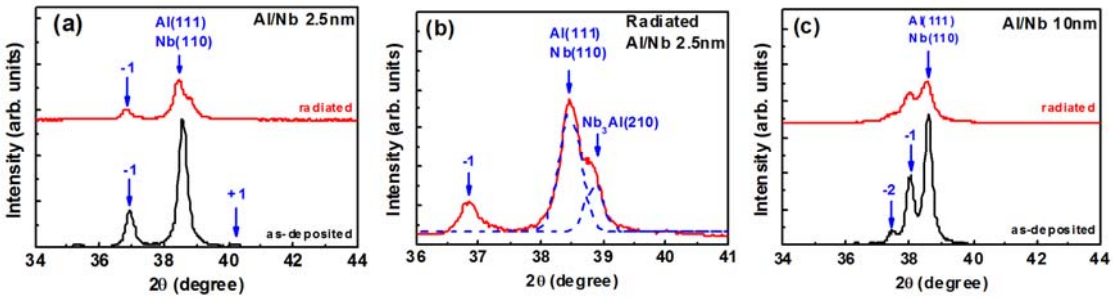

Figure 5.3 X-ray diffraction patterns of (a) Al/Nb 2.5 nm multilayers, and (c) Al/Nb 10 nm multilayers before and after He ion irradiations. Radiation induces a reduction of peak intensity and slight decrease of peak positions of Al (111) or Nb (110). (b) Deconvolution of XRD peaks in radiated Al/Nb 2.5 nm specimen shows the formation of Nb_3Al (210).

A series of XRD experiments were performed to study the evolution of microstructures after radiation. XRD patterns of pure Al and Nb film, not shown here, show negligible peak position variations after radiation. In as-deposited Al/Nb 2.5 nm and Al/Nb 10 nm multilayers, XRD patterns reveal overlapped Al (111) and Nb (110) peaks together with first order (Fig. 5.3(a)) and second order (Fig. 5.3(c)) superlattice peaks, consistent with observations in the literature [150]. The bilayer thicknesses estimated from superlattice peak positions are essentially the same as those measured from XTEM studies. After radiation, the peak intensity of all Al, Nb peaks, including superlattice peaks, decreased. The peak positions of Al (111) and Nb (110) slightly decreased to lower angles. Also, when h is 2.5 nm, radiation induced a peak split at the original position of Al (111). Peak devolution was performed for irradiated Al/Nb 2.5nm multilayer, as illustrated in Fig. 5.3(b), and such analysis revealed the existence of Nb_3Al

intermetallic compound after radiation.

Microscopy experiments were performed to unravel the evolution of microstructures after radiation in detail. Fig. 5.4 shows underfocused bright-field TEM images of ion irradiated Al/Nb 100 nm specimens. Close to the surface of the film, as shown in Fig. 5.4(a), few He bubbles are observed. In a region in which the He concentration is predicted to be the highest by SRIM simulation, as presented in Fig. 5.4(b), a maximum He bubble density, ~ 5.5×10^{24} m^{-3} (assuming the thickness of the sample is 25 nm), is indeed observed in both Al and Nb. The diameter of the He bubbles in Al and Nb is approximately 1 nm. At a depth of ~ 1100 nm underneath the film surface, essentially away from the SRIM predicted radiation damage zone across a depth of 0-700nm, Al and Nb individual component, and their interfaces are essentially intact without signs of radiation damage, as shown in Fig. 5.4(c). Fig. 5.5 illustrates the interplanar spacing of the smallest diffraction ring in SAD patterns captured with an aperture of ~ 100 nm in diameter. It is evident that the calculated inter-atomic spacing aligns well with that of Al (111) and Nb (110) at both ends except the occurrence of a sharp decrease at 300-500 nm underneath the film surface. The values of interatomic spacing at the trough approach that of Nb_3Al (210) diffraction. The position of the trough minimum coincides with the superimposed maxima of He concentration as predicted from SRIM calculation.

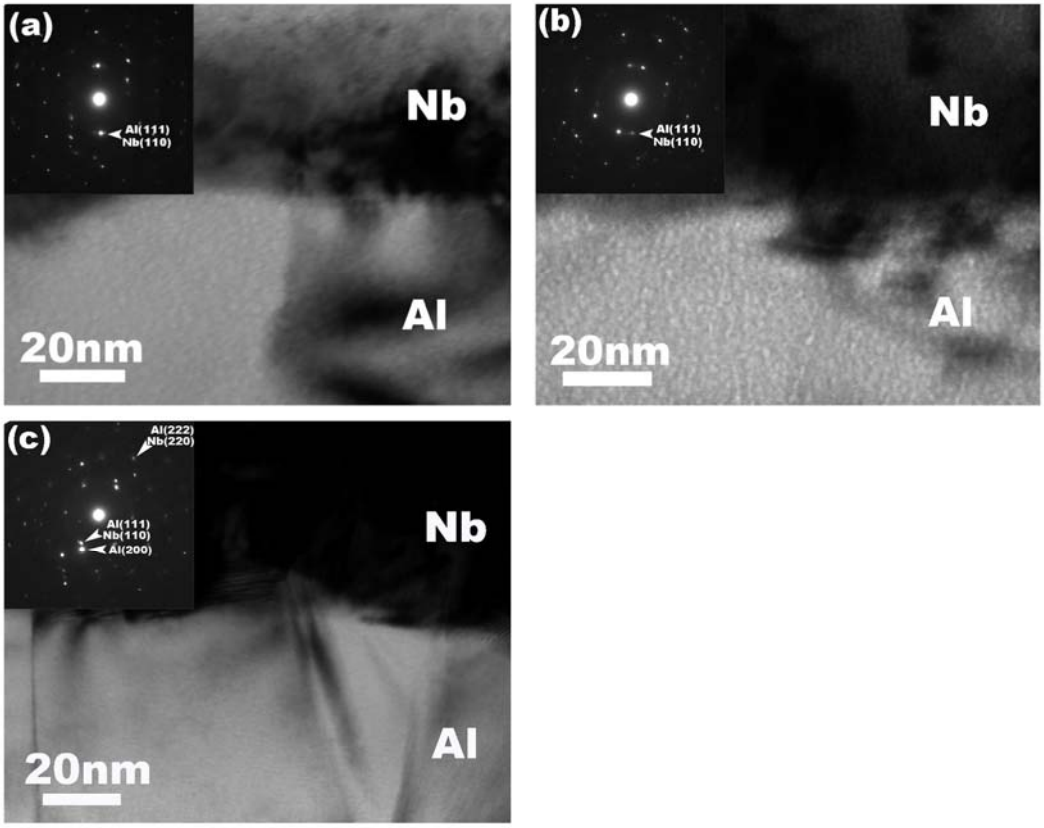

Figure 5.4 XTEM image of Al/Nb 100nm after radiation. (a) At 100 nm below the surface, few He bubbles can be seen primarily in Al layer. (b) In the peak damage region, 400nm in depth, a large number of He bubbles are observed. (c) At a depth of 1100 nm, essentially no damage is observed.

Extensive XTEM studies were carried out on ion irradiated Al/Nb 2.5 nm multilayers. Underfocused XTEM micrographs are shown in Fig. 5.6 (a), (b) and (c), corresponding to the surface, peak damage and essentially unirradiated regions, respectively. Discrete layer structure is retained after radiation in all regions. At the surface region, He bubbles are barely detectable, whereas a He bubble density of $1.9\times10^{24}m^{-3}$ is observed in the peak damage region, and most He bubbles appear along

layer interfaces. HRTEM studies of the same specimen are shown in Fig. 5.6 (a') - (c') in the three corresponding regions.

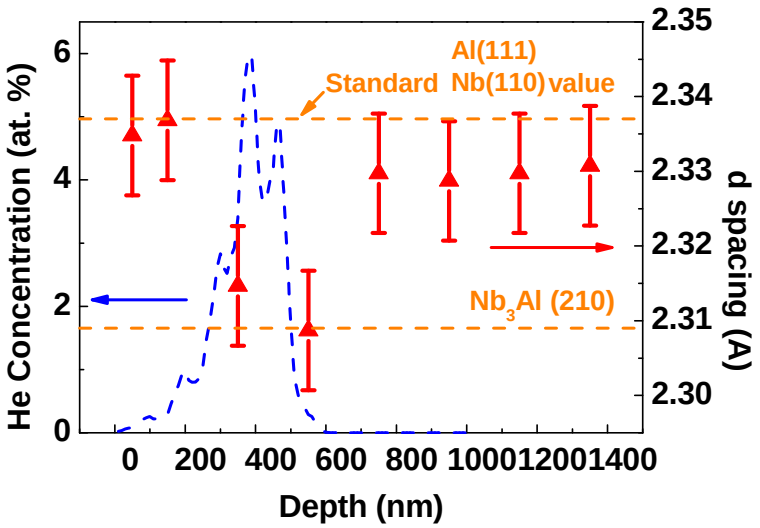

Figure 5.5 Variations of lattice spacing, along implantation path, of the first ring in SAD patterns examined in XTEM studies with an aperture of 100 nm in diameter. Superimposed is the SRIM calculation of He concentration profile. The lattice spacing is indexed to be either Al (111) and/or Nb (110). A minimum lattice spacing is observed at the peak He concentration region, corresponding to the value of Nb_3Al (210).

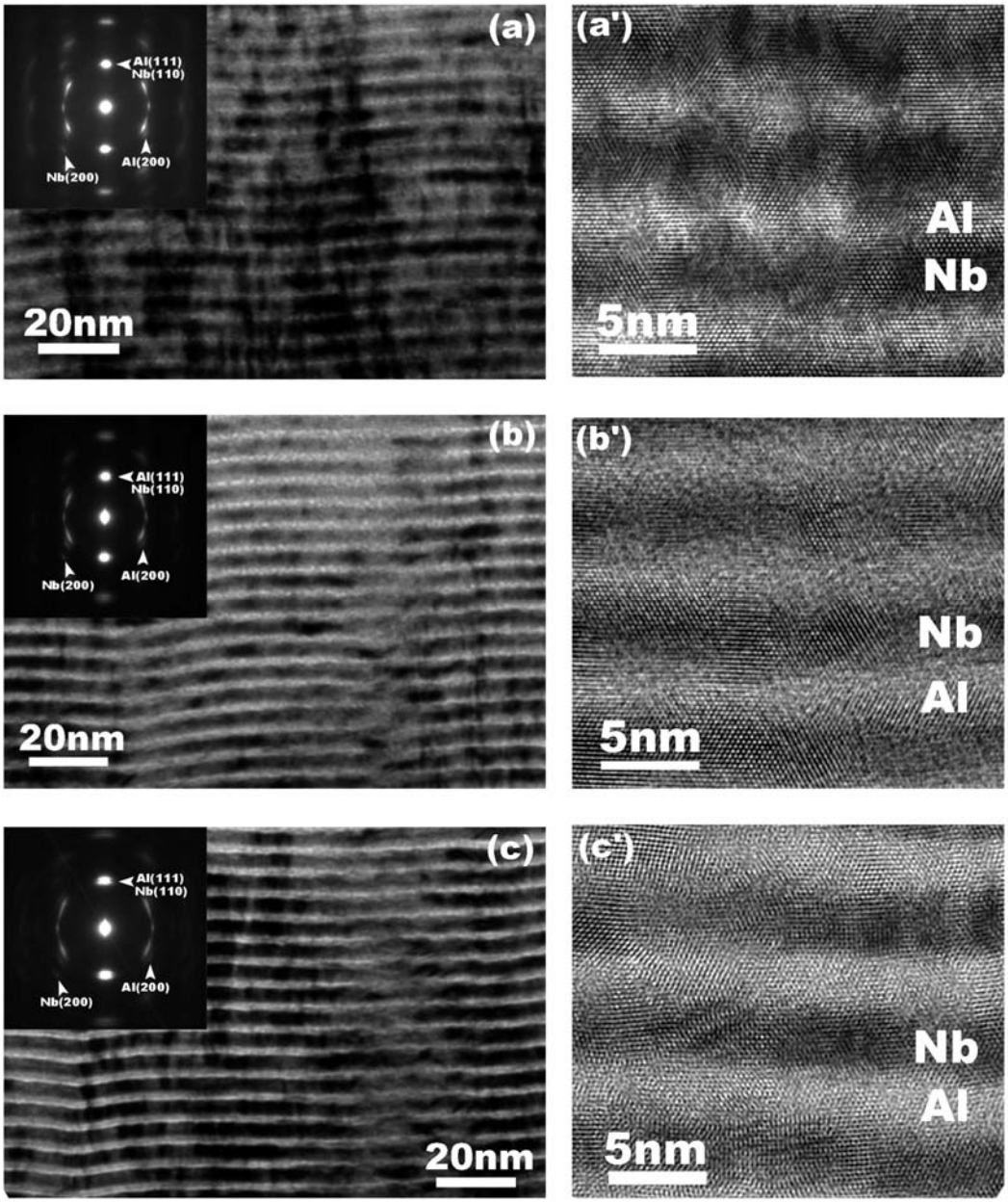

Figure 5.6 Underfocused XTEM images of irradiated Al/Nb 2.5nm show the retention of layer interface at (a) surface, (b) peak damage, and (c) unirradiated regions. He bubbles are observed primarily in peak damage regions. HRTEM micrographs of the corresponding regions shows rough interface in (a') and (b'), and (c') crystallographically well-defined interface in unirradiated region.

5.4.2 Chemical analysis of irradiated Al/Nb multilayers

STEM studies with 0.23nm resolution in image mode and EDX analysis with a few nm probe size were performed to examine the integrity of irradiated layer interface. Fig. 5.7(a) shows a STEM image of the ion irradiated Al/Nb 100nm multilayers. The darker layer is Al, as the contrast scales with atomic number in STEM mode. Interfaces close to the surface seem to be less wavy. Two straight lines, b and c, were drawn normal to the layer interfaces to perform chemical analysis via EDX line scan method. The compositional variation along line b, close to the film surface, is shown in Fig. 5.7(b). The width of the interface, estimated by using 10-90 at.% cut-off criterion, is approximately 11 nm. The EDX scan of line c in the peak damage region, shown in Fig. 5.7(c), yields an interface width of ~ 14 nm.

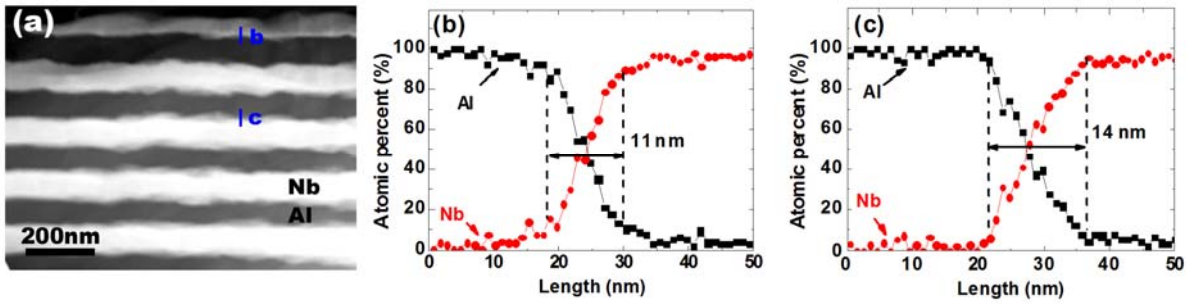

Figure 5.7 Chemical analysis of layer interface in irradiated Al/Nb 100 nm multilayers. (a) STEM image reveals chemically abrupt interface close to surface, and wavy interfaces in peak damage region. EDX composition profiles along line b and c normal to layer interfaces show the interface width of ~ 11 nm (b) and 14 nm (c) by using a cut-off criterion of 10-90%.

Similar STEM studies were carried out on ion irradiated Al/Nb 2.5 nm multilayers. Fig. 5.8(a)-5.8(c) are the STEM micrographs of the same specimen at locations close to the surface, peak damage and bottom (unirradiated) regions, respectively. In all the cases the layer interfaces are clearly distinguishable. The layer interfaces in the peak damage region, as shown in Fig. 5.8(b), appear slightly rougher. EDX chemical analyses were performed along solid lines marked in each micrograph with the line direction normal to the layer interfaces. The corresponding compositional profiles are shown in Fig. 5.8(a')-(c'). In 5.8 (a') and 5.8(c'), the composition profiles of Al and Nb vary alternatively along the path of line scans, whereas in the peak damage region, as shown in Fig. 5.8(b'), the compositional profile is more complicated, with intermingled Al and Nb signals.

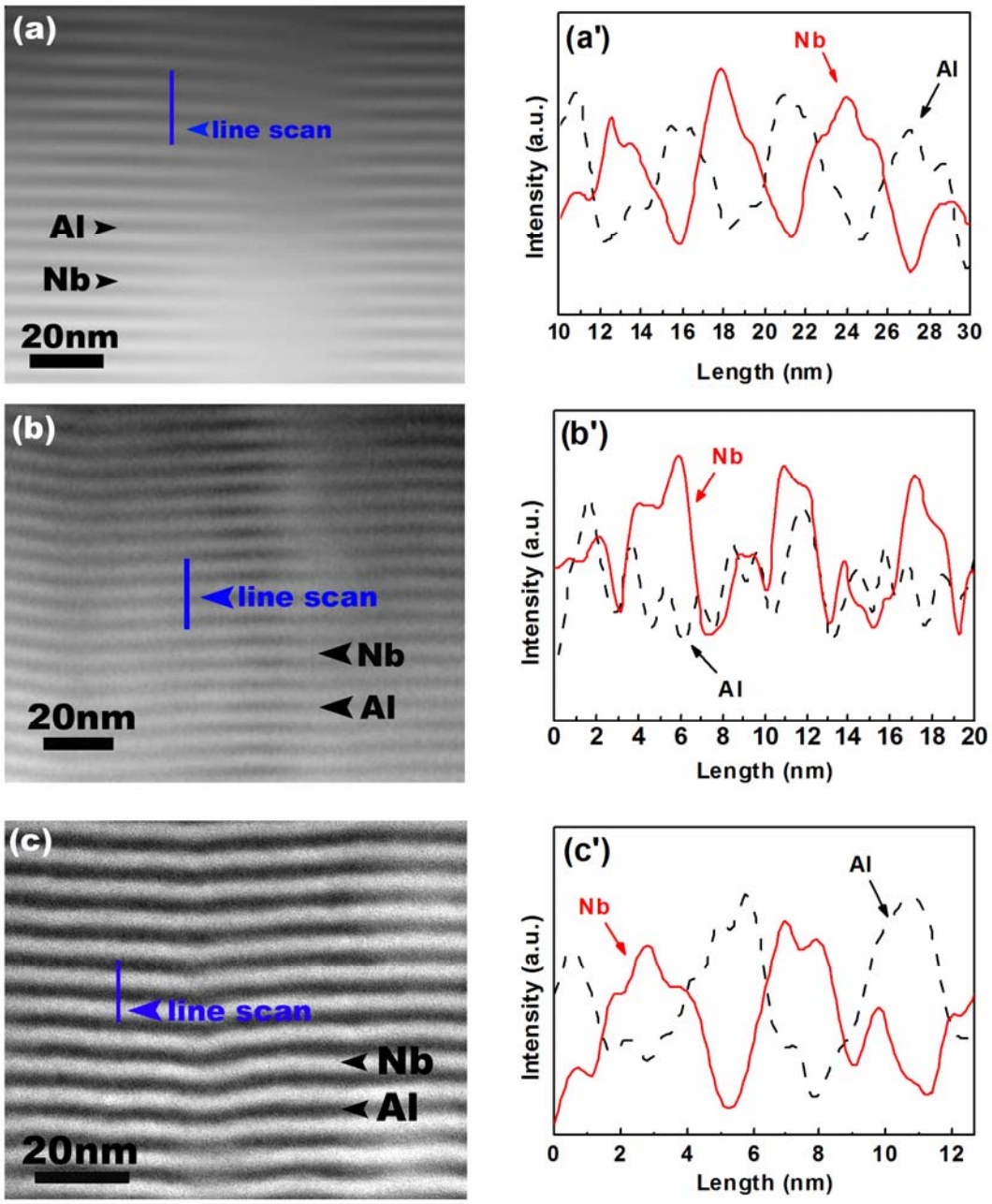

Figure 5.8 STEM micrographs of irradiated Al/Nb 2.5nm multilayers at different depth. (a) surface, (b) peak damage region, and (c) unirradiated region. The corresponding EDX analyses along line markers show alternating Al and Nb compositions in (a') and (c'), and intermixing along interface in the peak damage region (b').

5.4.3 Mechanical properties

The hardness of as-deposited (solid squares) and ion-irradiated (solid circles) Al/Nb multilayer films are compared in Fig. 5.9(a) as a function of $h^{-1/2}$, where h is the thickness of individual layers. In as-deposited multilayers, when h is 25 nm or greater, the hardness of multilayers scales approximately linearly with $h^{-1/2}$, following a Hall-Petch relationship, with a Hall-Petch slope of 13 GPa·$nm^{0.5}$. As h decreases even further, the film hardness increases nonlinearly, and reaches a peak value of ~ 5.6 GPa at h = 1 nm. As shown in Fig. 5.9(a), after radiation, when h is greater than 25 nm, the hardnesses of Al/Nb multilayer films vary slightly compared to that of as-deposited films with identical layer thickness, and almost the same Hall-Petch slope is obtained (the Hall-Petch slope is ~ 12.9 GPa·$nm^{0.5}$). When h is 10 nm or less, radiation clearly leads to hardening and the hardening is more significant at smaller h. The evolution of film hardness, ΔH, is manifested vs. $h^{-1/2}$ in Fig. 5.9(b). Radiation hardening is negligible when h is 25 nm or greater, and increase monotonically thereafter with reducing h, and the magnitude of radiation hardening approaches a maximum of 2 GPa when h = 1 nm. Also shown in the same plot are two horizontal dash lines, representing the hardness variations (enhancement) of single-layer pure Al and Nb films after radiation, measured to be 0.23 and 0.77 GPa, respectively.

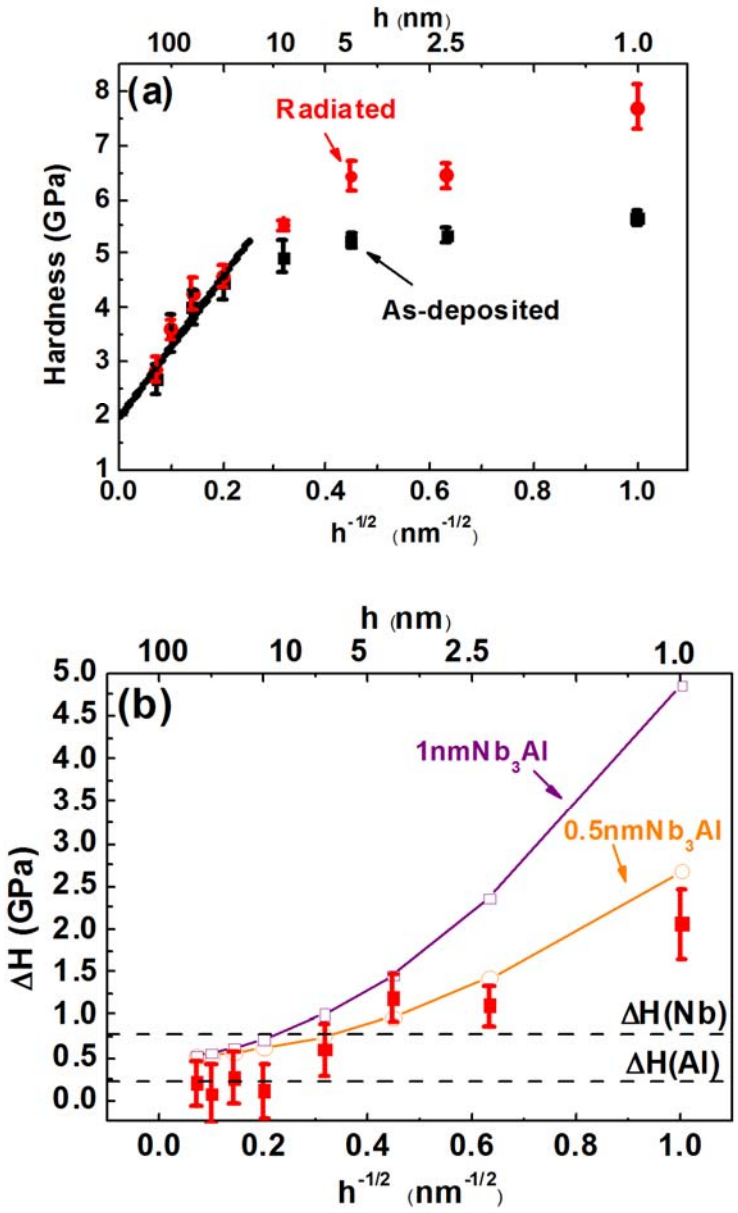

Figure 5.9 (a) Comparisons of hardness vs. $h^{-1/2}$ for as-deposited (solid squares) and ion-irradiated (solid circles) Al/Nb multilayer films. The hardnesses of multilayers with layer thickness of greater than 20 nm are best fitted by using solid lines. (b) Hardness enhancement vs. h shows that the hardness increases slightly when h is > 20 nm, whereas radiation hardening is significant and increases monotonically at smaller h. Two dash lines indicate radiation hardening of single layer Al and Nb films. Calculated radiation hardening by considering defects, and using a simple model based on the formation of 0.5 and 1 nm thick Nb_3Al intermetallic layer along interface.

5.5 Discussions

5.5.1 Microstructural evolutions

We now examine the evolution of microstructures after radiations from perspectives of the morphological stability of interfaces, the formation of new phases along interfaces, and radiation induced defects. These analyses are crucial in interpreting the hardness evolutions in irradiated Al/Nb multilayers.

Morphological stability of layer interfaces: It is evident from XTEM and STEM studies that nanolayer structures are retained in all films even in the peak radiation damage region. The retentions of layer morphology in immiscible Cu/Nb and Cu/V nanolayer system after heavy He ion irradiation (peak dose of 5-8 dpa) have been observed and is rationalized based on the fact that both systems are immiscible [143, 147]. Al and Nb have a positive heat of mixing [80], and hence the formation of intermetallic phases, to be discussed later, is expected. Such an effect accompanied by SRIM predictions of ballistic intermixing at a few dpa level could lead to a complete loss of interfaces in heavily radiated region. The retention of interfaces in Al/Nb 2.5 nm nanolayer system even in the peak damage regions is thus an intriguing observation. On the other hand, radiation damage in the form of ballistic intermixing is manifested by ~ 1 nm increase in interface roughness, as observed in Fig. 5.6(a') and 5.6(b'). Quantitative chemical analyses of irradiated Al/Nb 100 nm layer interfaces also indicate a slight

increase in the width of interface (Fig. 5.7(b) and 5.7(c)) after radiation, another evidence of radiation induced irregularity along interfaces.

Radiation induced formation of new phase, Nb_3Al, along the interfaces: As shown in the equilibrium phase diagram, the Al-Nb system contains three intermetallic compounds: Nb_3Al (A15 structure), Nb_2Al (σ structure) and Nb Al_3 (DO_{22} structure) [151]. Thermal stability of Al/Nb multilayer films have been investigated by Barmak's group [150, 152, 153]. In a series of annealing experiment, they found that new phases formed in a sequential rather than a simultaneous manner. The $NbAl_3$ was the first phase observed, followed by Nb_3Al at a later annealing stage, i.e. at higher annealing temperature [153]. Our XRD and TEM analyses confirm the formation of Nb_3Al after He ion irradiation of all Al/Nb multilayers. As shown in Fig. 5.5, the reduction of lattice parameter (measured from the smallest diffraction ring) in the peak radiation damage region is due to the formation of Nb_3Al (210). Our study is thus different from the observations in the thermal annealing studies of Al/Nb multilayers. Phase transformation induced by ion mixing can be very different from that created by equilibrium thermal annealing processes [154, 155]. For instance, in Al/Ni bilayer system, $NiAl_3$ is formed by thermal annealing, but NiAl is formed by ion irradiation [156]. STEM studies suggest that the Nb_3Al phase forms along layer interface due to radiation induced ballistic mixing, and the formation of the phase seems to increase the roughness of interface as

mentioned previously. STEM analysis of Al/Nb 2.5 nm multilayers in peak damage region as shown in Fig. 5.8(b) implies somewhat sharper layer interface than that of EDX analysis (as shown in Fig. 5.8(b')) from intermingled Al and Nb compositions. The image resolution of STEM is ~ 0.23 nm, whereas chemical analysis depends sensitively on probe size. A probe size of a few nm is used in this study, and hence leads to uncertainty in determining the thickness of intermetallic layer. STEM together with EDX line scan analyses indicate that the thickness of the Nb_3Al phase is approximately 1 nm in Al/Nb 2.5 nm multilayers, and greater in multilayers with larger h. Compared to Al, Nb_3Al is densely packed crystallographically with much stronger interatomic bonds. We suspect that such a dense intermetallic layer prevents further intermixing of Nb and Al during He ion irradiation experiments, i.e., Nb_3Al may have acted as a barrier to the interdiffusion of each constituent, and hence facilitate the retention of layer structure after radiation.

Radiation induced defects and their size dependence on h: The reduction of XRD peak intensity of Al (111) and Nb (110) after He ion irradiation is an indication of disordering of crystal lattices due to radiation induced point defects. Peak broadening was also observed in irradiated multilayers, and can be interpreted as a result of microstrain in lattices [157]. Lattice expansion is frequently observed as a result of entrapment of interstitials, and typically increases monotonically with the volume

change (expansion), $\Delta V/V$. The volume expansion of neutron radiated pure Al and Nb is estimated to be $(\Delta V/V)_{Al}$ = 1.4-1.7 [158, 159], and $(\Delta V/V)_{Nb}$ = 0.85 [160]. Slight lattice expansion is also observed from our XRD analyses. On other occasions, lattice expansions have also been observed in He ion irradiated Fe/W and Cu/V multilayers [146, 147]. The density of interstitial loops, 1-1.5 nm in diameter, in N ion irradiated single crystal Nb films is ~ 0.2-1.6 × $10^{24}/m^3$, and the density of vacancy clusters, 0.5 nm in diameter, is ~ 1 × $10^{25}/m^3$ [161]. In the current study, the concentration of He bubbles, N_{He}, in peak damage region is estimated to be ~ 5.5 × $10^{24}/m^3$ and 1.9 × $10^{24}/m^3$ in Al/Nb 100 nm and Al/Nb 2.5 nm multilayers, respectively. It is evident that He bubble density is lower in multilayers with smaller h. Our recent studies on radiation induced damage in Cu/V have shown a clear trend of reduction of overall He bubble density with reducing h [147]. Layer interface may act as sinks for radiation induced point defects, vacancies and interstitials. The diffusivity of point defects is also higher than inside lattices, and consequently dramatically enhances the probability of annihilating opposite type of point defects.

5.5.2 Analysis of radiation hardening mechanisms

We now attempt to estimate radiation hardening by considering the contributions from He bubbles, interstitials, as well as Nb_3Al intermetallic compound in irradiated Al/Nb multilayers.

He bubbles: For weak obstacles, such as He bubbles [67, 162 - 164], a hardening relationship developed by Friedel-Kroupa-Hirsch (FKH) is applied to describe the dependence of radiation hardening on He bubbles [165 - 167]:

$$\Delta\sigma = \frac{1}{8} M\mu b d N_{He}^{2/3} \quad (5.1),$$

where M is Taylor factor, 3.06 for FCC and BCC metal, μ is the shear modulus, b is the Burgers vector, and d is the diameter of defect clusters. By using b = 2.86Å, an average shear modulus of the composite is 31 GPa, d = 1 nm, and the peak density of He bubbles measured from XTEM, the increase in yield strength from FKH model is calculated to be ~ 0.11 GPa and 0.052 GPa for Al/Nb 100nm and Al/Nb 2.5 nm respectively. Correspondingly hardness enhancement of 0.33 GPa in Al/Nb 100nm, and 0.16 GPa in Al/Nb 2.5 nm is obtained assuming yield strength is one third of the film hardness. The estimated radiation hardening is in-line with that of measurement for Al/Nb 100 nm multilayers, but clearly underestimates the experimental measurement in Al/Nb 2.5 nm multilayers. Assuming the He bubble density in Al is on the same order of magnitude as that in Al/Nb 100 nm multilayers, $5.5 \times 10^{24}/m^3$, then the measured radiation hardening in pure Al films, ~ 0.23 GPa, aligns well with estimation of He bubble induced hardening, ~ 0.26 GPa.

Interstitial (dislocation) loops: Interstitial loops are typically considered as stronger barriers to the trespassing of dislocations. Based on a dispersed barrier hardening model

[45, 168, 169], the increase in yield strength $\Delta\sigma_y$ is equated to the increase in applied stress required to move a dislocation through a field of obstacles:

$$\Delta\sigma_y = M\alpha\mu b/l = M\alpha\mu b\sqrt{N_{loop}d} \quad (5.2),$$

where α is the barrier strength, and l is the average spacing between obstacles, and can be estimated as $1/\sqrt{Nd}$, where N_{loop} and d is the average loop density and loop diameter, respectively. Considering the typical barrier strength of dislocation loops, α is taken as 0.45 [170, 171]. An experimental determination of loop density is not yet available due to the difficulty of imaging dislocation loops in Nb with ~ 100 nm or less grain sizes and Al/Nb multilayers. As reported in literature the density of interstitial loop density is typically orders of magnitude lower than that of vacancy clusters (or He bubbles) in fcc metals [172]. Hence interstitial loop induced hardening in Al films is insignificant. However, in Nb, the density of interstitial clusters is comparable to that of vacancy clusters [161]. Assuming radiation hardening in Nb arrives primarily from He bubble (calculated to be ~ 0.39 GPa by assuming a bubble density of $5.5 \times 10^{24}/m^3$) and interstitial loops, then interstitial loop induced hardening shall be ~ 0.38 GPa, i.e., the difference between the measured hardening of 0.77 GPa and the calculated He bubble induced hardening. Such analysis in turn yields a dislocation loop density of $7.2 - 2.4 \times 10^{22} / m^{-3}$ in Nb, assuming the loop diameter is 1- 3 nm, a bit lower than the loop density of ~ $0.2\text{-}1.6 \times 10^{24}/m^3$ in N ion irradiated single crystal Nb films [161] (~17-190keV N

ions, and a fluence of 1-5 $\times 10^{19}/m^2$, and a peak damage of ~ 6dpa). This is not surprising as the atomic mass of N ions is much heavier than that of He ions, and hence defect density should be higher in N ion irradiated Nb films.

Radiation hardening due to the formation of Nb_3Al phase at layer interfaces: The aforementioned analyses of defects concentrations account for radiation hardening in single layer Al and Nb films. In multilayers, radiation induces the Nb_3Al phase along the Al/Nb interface with a finite thickness of ~1 nm or greater and the thickness of such compound reduces at smaller h as discussed in sec. 4.1 Based on these observation, we developed a composite model to interpret the radiation hardening in Al/Nb multilayers. The schematic of the composite architecture is shown in Fig. 5.10, where a 0.5-1 nm thick layer of Nb_3Al is sandwiched between Al and Nb interface after radiation. The volume fraction of Nb_3Al is clearly greater in multilayers with smaller h, and its influence on radiation hardening, in turn, should be more significant. Specifically, the hardness evolution due to the formation of Nb_3Al is estimated by:

$$\Delta H = \frac{h_{Nb_3Al}}{2h}(H_{Nb_3Al} - H_{as-dep}) \qquad (5.3),$$

where H_{Nb_3Al} and H_{as-dep} represent the hardness of Nb_3Al and as-deposited multilayers, respectively. Chung et al. measured the hardness of Nb_3Al and obtained a Vickers hardness number of 980 [173]. By using the hardness of bulk Nb_3Al, and considering the hardening due to average ROM (as estimated by the average ROM of

single layer Al and Nb), calculation were performed for the formation of 0.5 and 1 nm thick Nb_3Al layers and results are shown as two dash lines in Fig. 5.9(b). It is evident that simulated results capture the experimental trend, i.e. the monotonic increase of radiation hardening at smaller h. Calculated results based on 1 nm thick Nb_3Al fit experimental observation well at greater h, whereas they clearly overestimate radiation hardening at smaller h. Radiation induced intermixing seem to be more significant in multilayers of greater h (> 25 nm). Calculated radiation hardening based on an intermixing zone width of 3 nm is only slightly higher than the current calculation and hence results are not shown in the figure. The assumption of the formation of a thinner Nb_3Al layer, 0.5 nm in thickness, seems to fit radiation hardening better at smaller h, although the simulation also overestimates radiation hardening to some extent. This is probably because all calculations incorporate an average ROM hardening of single layer Al and Nb. As discussed previously, the density of He bubbles and interstitials loops both decrease considerably due to enhanced annihilation of opposite type of point defects along layer interfaces, and hence the composite model slightly overestimated radiation hardening in these fine nanolayers. The dependence of radiation hardening on h has recently been studied in He ion irradiated Cu/V nanolayers, where the exact opposite trend is revealed, i.e., the magnitude of radiation hardening is considerably less and decreases continuously at smaller h [147]. In the immiscible Cu-V system, radiation hardening is

dominated by the concentrations of defects - He bubbles and interstitials loops, both of which decreases monotonically with decreasing h [147].

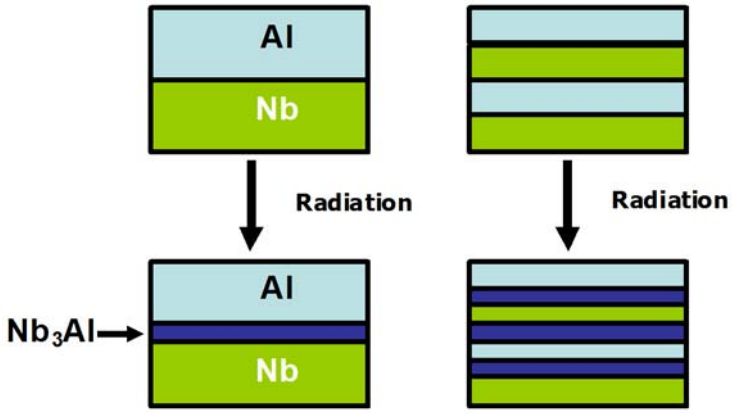

Figure 5.10 Schematics of a composite model that consists of a 0.5-1 nm thick Nb_3Al layer along the Al/Nb layer interfaces in irradiated Al/Nb mutilayers. The volume fraction of the intermetallic layer increases in multilayers of smaller h.

Finally we briefly comment on the measured Hall-Petch slope. The Hall-Petch slope of yield stress, k_σ, is a measure of interface barrier strength for slip transmission and can determine the rate of strength increase with decreasing h, and can be calculated by using

$$k_\sigma = 0.18G\sqrt{b} \qquad (5.4),$$

where G and b are the shear modulus and the magnitude of Burgers vector of the stiffer component of the multilayers, respectively [174]. The calculated value is similar to the experimental observation [147]. In spite of the formation of Nb_3Al intermetallic compound along layer interfaces, the Hall-Petch slope of as-deposited and ion irradiated

multilayers remain essentially the same, indicating the impact of the thin Nb_3Al intermetallic compound on the strength of composites is insignificant when h is greater than 25 nm.

5.6 Conclusions

The present studies reveal that He ion irradiation induces defects, such as He bubbles and interstitials, in Al/Nb multilayers. Extensive microscopy studies also confirm the formation of Nb_3Al intermetallic compound along Al/Nb interface as a consequence of radiation induced intermixing. The composite model suggests that the trend of enhanced radiation hardening at smaller h can be rationalized by the formation of a much harder Nb_3Al intermetallic phase, the volume fraction of which increases at smaller h.

CHAPTER VI

HE ION IRRADIATION TOLERANCE OF FE/W (BCC/BCC) MULTILAYERS*

6.1 Overview

We report on the evolution of microstructure and mechanical properties of Fe/W multilayers subjected to helium ion irradiations. Sputtered Fe/W multilayers with individual layer thickness, varying from 1 to 200 nm, were subjected to He^+ ion irradiation with a peak displacement per atom value of 6 at ambient temperatures. Helium bubbles, 1-2 nm in diameter, were observed in Fe and W, and more so along layer interfaces. The magnitude of hardness variation after radiation depends on individual layer thickness. Radiation hardening is observed in specimens with individual layer thickness of ≥ 5 nm. At smaller layer thickness, the hardness barely changes. Analysis indicates that radiation hardening may originate mainly from dislocation loops and only partially from He bubbles.

6.2 Introduction

High energy helium (He) ion irradiation of metals generates a large number of defects, including vacancies and interstitials, He bubbles and dislocation loops [135, 136, 175]. Radiation typically degrades the mechanical properties of metals, most notably an

*Reprinted with permission from "He ion irradiation damage in Fe/W nanolyer films" by N. Li, E.G. Fu, H. Wang, J.J. Carter, L. Shao, S.A. Maloy, X. Zhang, 2009, Journal of Nuclear Materials, 389, 233, Copyright [2010] by Elsevier.

increase in yield strength, and significant loss of ductility (embrittlement) [142]. Radiation induced defects in metals are of great interest, because these defects determine the performance of irradiated materials in nuclear reactor environment. He bubbles and dislocation loops are two major types of radiation induced defects. The solid solubility of He in metals is very low [176]. Thus, at relatively low concentrations of implanted He, it is easy to form He-vacancy clusters, which act as the nucleus for He bubble formation [177]. Once nucleated, in order to maintain a mechanical equilibrium between their internal pressure and the sintering stress, $2\gamma/r$, where γ is the surface energy and r is the bubble radius, the bubbles grow by absorbing He atoms and radiation-induced vacancies [162]. High energy He ion bombardment of metals also produces recoil interstitial metal atoms that collapse into prismatic dislocation loops. Different types of defects have different obstacle strengths for glide dislocations. In general, voids and large precipitates act like Orowan barriers and have large barrier strengths; small bubbles, small clusters and network dislocations have relatively small barrier strengths. Lucas reviewed the mechanical properties of austenitic stainless steels [67], and found that at low temperature (~373K), hardening was dominated by Frank loops at low dose, and by the network dislocations at higher dose. At higher temperature, ~ 673K, voids and bubbles begin to contribute to hardening, especially at high dose. Other studies on irradiated 316LN stainless steel show, at approximately 1 at.% He concentration, dislocations and

loops can be pinned by He bubbles in the lattice significantly [178].

Recent studies have shown that interfaces in composite materials can act as sinks for radiation induced defects, promote recombination of unlike point defects, and result in enhanced radiation tolerance as compared to conventional single-phase bulk metals [143 - 145]. For instance, He ion Cu/Nb multilayer films with a few nm layer thickness seem to suppress the burst of He bubbles after annealing [143]. In this study, we chose Fe/W multilayers for radiation damage studies. Compared to Cu, Fe and W have relatively high melting points, and more open crystal structure, bcc vs fcc. Molecular dynamics simulations suggest that the characteristics of interface could be a key factor in determining the accumulation of radiation damage in composite materials [179]. The lattice parameter difference between Fe and W is rather large (~ 10%), so the Fe/W interface is incoherent [180], and thus could enhance the capability of defect storage. The study will allow comparison of incoherent bcc/bcc Fe/W interfaces with incoherent bcc/fcc Cu/Nb interfaces.

6.3 Experimental

Fe/W multilayers were deposited by magnetron sputtering at room temperature on SiO_2 substrates. The vacuum chamber was evacuated to a base pressure less than 5×10^{-8} torr prior to deposition. The constituents within the multilayers have equal layer thickness, varying from 1 to 200 nm. The total film thickness was about 2 μm. After

deposition, films were implanted at room temperature with 100 keV He^+ ions to a dose of $6\times10^{16}/cm^2$. The beam current is around 6 microamps and the temperature of the stage is around 50 degree C during implantation. Transmission electron microscopy (TEM) was performed in a JOEL 2010 microscope operated at 200 kV. Selected area diffraction studies were performed with an aperture of 100 nm in diameter. X-ray diffraction (XRD) experiments were performed on Bruker D8-Focus Bragg-Brentano x-ray diffractometer. The hardness and modulus of multilayers before and after irradiation were measured, at room temperature, by Fischerscope HM2000XYp with Vickers indenter at an indentation depth down to 250 nm. The instrumented nanoindentation experiment is depth controlled with a typical load of 15 mN to achieve an indentation depth of 250 nm. A minimum of nine indents were performed at the same depth on each specimen to get an average hardness value.

6.4 Results

6.4.1 Microstructural evolution of irradiated Fe/W multilayers

Distinct Fe (110) and W (110) peaks are observed in XRD patterns of Fe/W 50 nm and Fe/W 5 nm multilayers as shown in Fig. 6.1. Fe/W 5nm multilayers seem to have stronger Fe (110) and W (110) texture than thicker films. In almost all cases, after ion implantation, peak intensity drops accompanied with peak shift to lower angle.

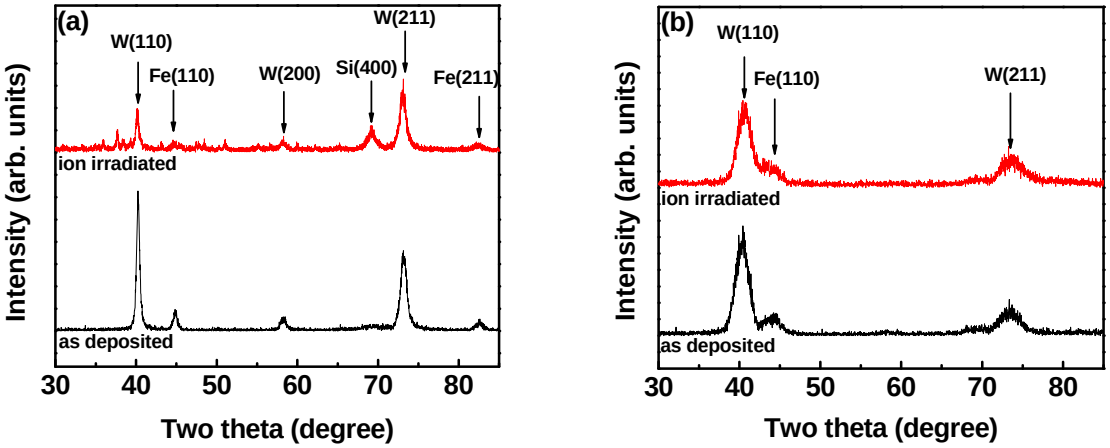

Figure 6.1 X-ray diffraction patterns of (a) Fe/W 50 nm multilayers, and (b) Fe/W 5 nm multilayers before and after He ion irradiations. Radiation induces reduction of peak intensity and a shift of peak position to lower angles.

Cross-sectional TEM (XTEM) images reveal radiation induced defects. Fig. 6.2 shows the microstructure of as-deposited Fe/W 50 nm multilayer film. Both constituents have polycrystalline microstructures, confirmed by inserted selected area diffraction pattern. The multilayer films have weak Fe and W {110} fiber texture perpendicular to the layer interfaces. The interface between Fe and W is chemically abrupt without signs of intermixing. For 50 nm layers, the in-plane grain sizes are on the order of layer thickness.

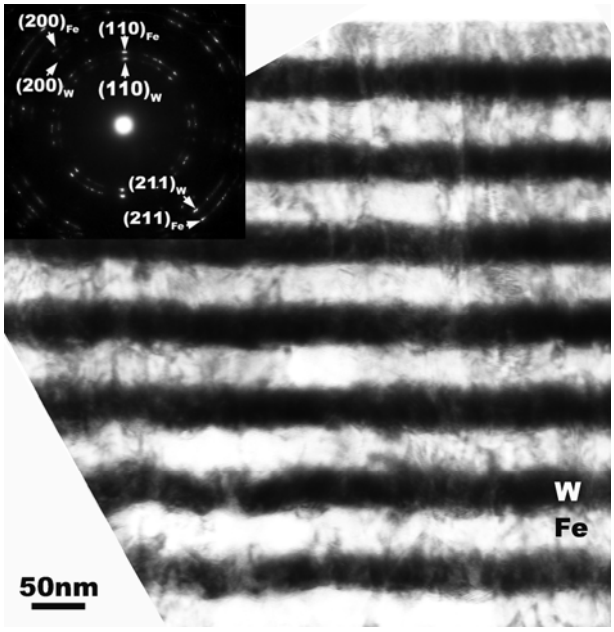

Figure 6.2 Cross-sectional TEM (XTEM) image of as-deposited Fe/W 50nm nanolayer shows clear and unmixed Fe and W layer interface with weak texture.

Fig. 6.3(a)-(c) show underfocused bright-field TEM images of ion irradiated Fe/W 50 nm specimens. Fig. 6.3(a) is taken from the surface region of the film. Limited He bubbles are observed in this region with relatively low bubble density. Fig. 6.3(b) is taken from the region in which the He concentration is predicted to be the highest by SRIM simulation (shown by a solid line in Fig. 6.4). Indeed a maximum He bubble density is observed in this region. The diameter of the He bubbles in Fe is about 1-1.5 nm, slightly greater than that in W. Furthermore the diameter of He bubbles seems to be larger when the bubbles are located along the interface compared to those inside the layers. “Black dots” observed from TEM micrographs in the underfocus conditions

could be point defect clusters and Frank dislocation loops. At ~ 600 nm underneath film surface, Fe and W layers and Fe/W interfaces are essentially intact with no signs of He bubbles, as shown in Fig. 6.3(c).

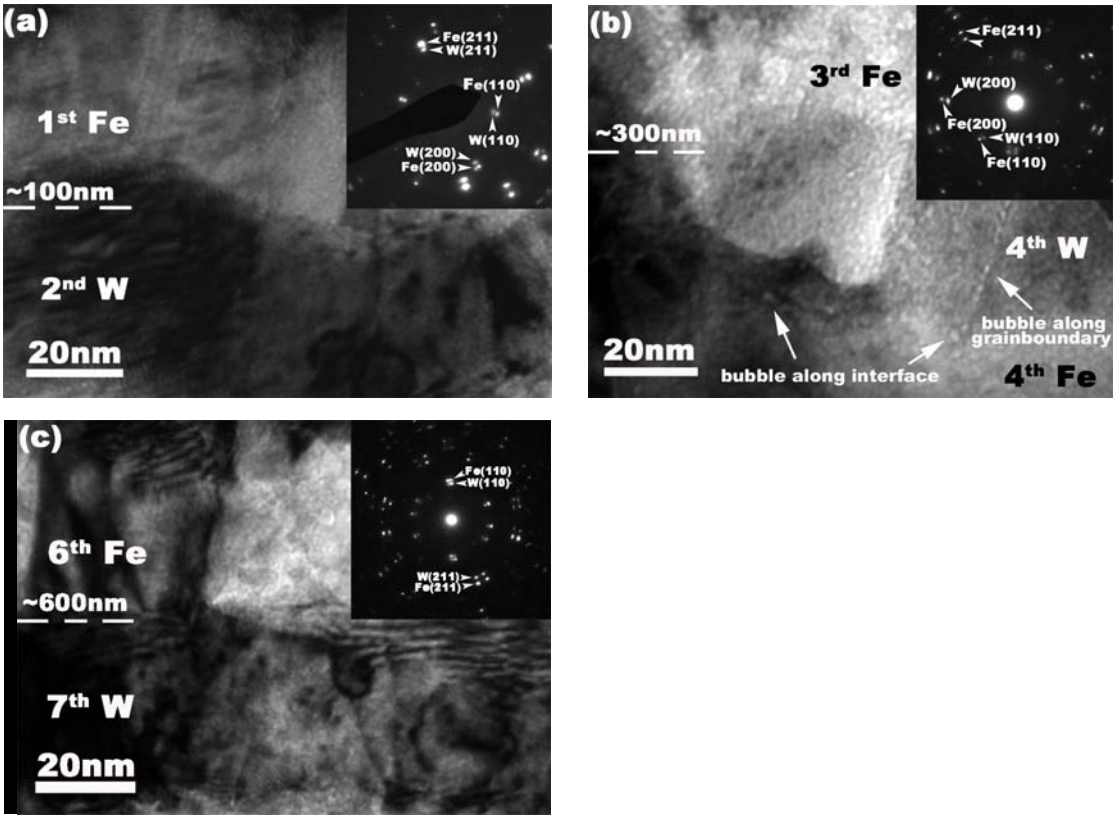

Figure 6.3 XTEM image of Fe/W 50nm nanolayers after ion irradiation. (a) In surface region, moderate amount of He bubbles was observed in Fe and W. (b) In a region of 300 nm underneath film surface, He bubble concentration increases dramatically, and He bubbles align along grain boundary and layer interfaces. (c) In the region of 600nm underneath film surface, away from radiation damage zone, multilayer films are essentially intact with clear Fe/W interfaces.

SRIM [149] calculation of He ion-irradiation has been performed on Fe/W multilayers with a nominal layer thickness of 50 nm. Fig. 6.4 shows the variation of He concentration versus implantation depth, together with the variation of lattice spacing of Fe (110) and W (110), which has been examined from XTEM studies. The simulation predicts that peak He concentration occurs at around 300 nm underneath the sample surface, with a peak displacement per atom (DPA) of around 6. Measurements of Fe (110) and W (110) interplanar spacing from selected area electron diffraction (SAD) patterns were performed with an SAD aperture size of 100nm in diameter. It can be seen that inter-atomic spacing of Fe (110) increases rapidly and quickly reaches a plateau at 300 nm, and remains largely distorted up to 500 nm in depth. Whereas lattice distortion in W (110) seems to take off at a bit deeper level and reach a peak value at ~ 500 nm. Lattice expansion maxima of approximately 3% were observed in the peak damage region from the examinations of Fe (110) and W (110) diffractions. Lattice expansions, 1-2%, are also observed (not shown here) from Fe and W (200) and (211) diffractions.

Similar XTEM studies were carried out on ion irradiated Fe/W 1nm multilayer films. Up to approximately 75 nm below the surface, as shown in Fig. 6.5(a), a discrete layer structure is not resolved and He bubbles were not detected. Fig. 6.5(b) shows the microstructure of films at a region approximately 340 nm below the surface, a region predicted to be heavily damaged based on SRIM simulations. A large number of He

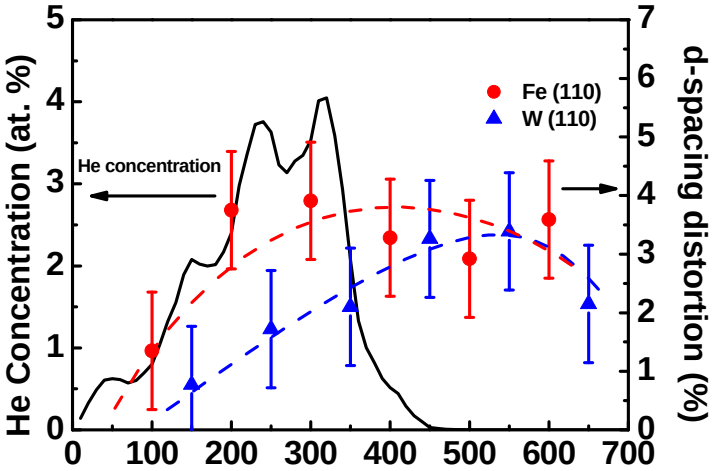

Figure 6.4 SRIM calculations that simulate the variation of He concentration versus radiation depth for He ions, 100keV/6×10^{16}/cm^2, same as the experimental condition. Variations of lattice spacing for Fe (110) and W (110) examined by detailed XTEM studies are also shown.

bubbles were observed in Fig. 6.5(b), without any clear resolution of the layer structures. The average He bubble size is ~ 1-2 nm in diameter. Fig. 6.5(c), taken at about 420 nm underneath the film surface, shows a reduction of He bubble concentration. Also the retention of layer structure at the bottom of this region indicates diminishing radiation damage. Radiation damage continues to decrease in deeper regions. At ~ 1200nm underneath the film surface, the microstructure is essentially identical to that of as-deposited specimens, i.e., the layer structure is clearly distinguishable without signs of radiation damage, as shown in Fig. 6.5(d).

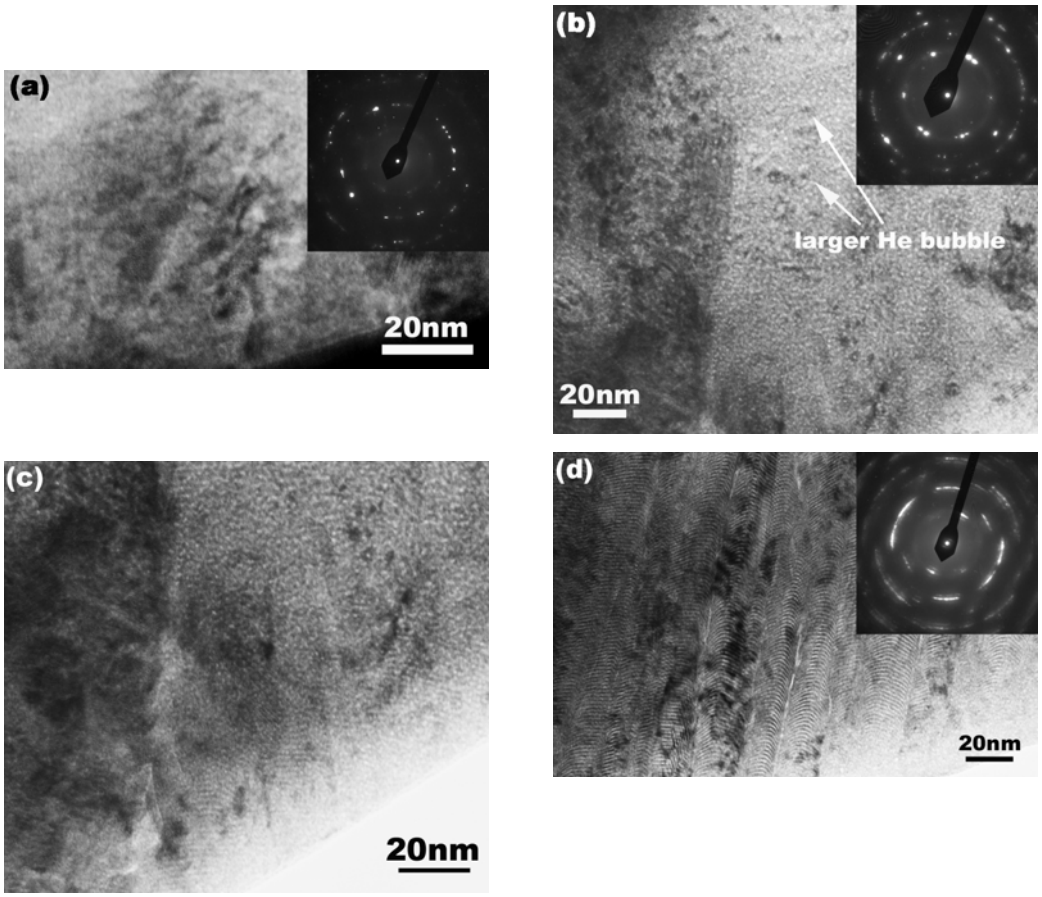

Figure 6.5 XTEM images of Fe/W 1nm multilayer film after He ion irradiation. (a) Microstructure in surface region, ~ 75 nm underneath the film surface, has little He bubbles and no clear sign of layer interfaces. (b) In heavily irradiated region, ~ 340 nm below film surface, He bubble density reaches a peak value. Fe and W interface can not be detected. (c) In a region of ~ 420 nm underneath film surface, the density of He bubbles decreases, and at the bottom of this region, layer structure is distinguishable. (d) In an essentially unirradiated region of ~ 1200 nm below surface, microstructure of multilayer is similar to those of as-deposited films.

6.4.2 Mechanical properties

The hardness of as-deposited and ion-irradiated Fe/W multilayer films are compared in Fig. 6.6(a) as a function of $h^{-1/2}$, where h is the thickness of individual layers. For as-deposited multilayers, when the individual layer thickness is 20 nm or

greater, the hardness of multilayers scales approximately linearly with $h^{-1/2}$, following a Hall-Petch relationship.

$$H = H_0 + kh^{-\frac{1}{2}} \quad (6.1),$$

where H is the hardness of the thin film, H_0 is film hardness at infinitely large layer thickness and k is the Hall-Petch slope, measuring the relative hardening contribution from layer interfaces. A linear fit to the experimental data is indicated by a solid line in the plot, yields H_0 = 6.9 GPa and k = 16.4 GPa·$nm^{0.5}$. As the individual layer thickness decreases even further, the film hardness increases nonlinearly, and reaches a peak hardness of 12.5 GPa at h = 1 nm. Radiation induces hardening in almost all multilayer films. When layer thickness is larger than 20 nm, the Hall-Petch relationship is also observed, as indicated by a dash line in the plot. The Hall-Petch slope of irradiated multilayers is 12.5 GPa·$nm^{0.5}$, smaller than that of as-deposited multilayer system. To compare the magnitude of radiation hardening, ΔH, a plot of ΔH vs. 1/ $h^{1/2}$ is shown in Fig. 6.6(b). Specifically, after He ion irradiation, the hardness of multilayers increases by 1.5-2 GPa when h ≥ 5 nm. Radiation hardening is less significant when h = 2.5 nm, and hardness barely changes when h = 1 nm.

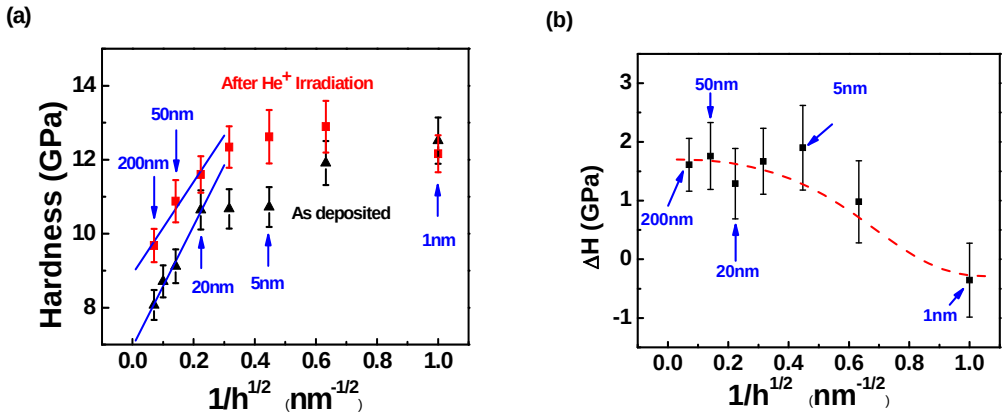

Figure 6.6 (a) Comparison of hardness as a function of $h^{-1/2}$ plots for as-deposited and ion-irradiated Fe/W multilayer films. The hardness of multilayers with layer thickness of greater than 20 nm is fitted by using a solid line, indicating that Hall-Petch dislocation pile-up model can describe strengthening in this regime. (b) Hardness enhancement vs. individual layer thickness showing that hardness increases by about 1.5 GPa for $h \geq 5$ nm specimens. When $h \leq 2.5$ nm, the hardness only increases slightly or barely changes.

6.5 Discussions

6.5.1 Microstructural evolutions

We will first examine radiation induced microstructure changes. XRD studies show that peak intensity of Fe (110) and W (110) decreases after He ion irradiation, and peak positions shift to lower angle. Reduction of peak intensity is an indication of disordering of crystal lattices due to radiation induced point defects, and peak broadening is often associated with microstrain due to entrapment of interstitials. Decrease of peak angle is an indication of enlargement of lattice spacing in a direction normal to interfaces. Radiation induced lattice expansion was also confirmed by selected area diffraction

patterns in TEM studies. Lattice expansion in Fe and W is likely to be a result of interstitials, including He interstitials and Fe and W self interstitials, and interstitial loops when loop diameter is on the order of nanometer length scale. Also intermixing of Fe and W due to radiation is likely to occur along layer interfaces, as Fe and W are miscible. Intermixing could lead to the formation of Fe-W solid solutions along interfaces and thus lead to distortion of lattices. XTEM studies show that the average bubble diameter in Fe is slightly larger than that in W. Based on the relationship: $p = 2\gamma/r$, where γ is the surface energy, and r is the radius of He bubble, the critical He concentration to nucleate He bubbles is proportional to γ, which typically scales proportionally with shear modulus [177]. Hence the difference in He bubble diameter may originate from the difference in shear modulus and surface energy between Fe and W [18]. Furthermore we noticed that He bubbles tend to have larger diameter with ellipsoidal shape along interface. This phenomenon has been observed in other systems [181]. A larger diameter (radius) of He bubbles along interface indicates that internal pressure and surrounding equilibrium pressure of He is lower.

6.5.2 Possible hardening mechanisms

We will first interpret radiation hardening in Fe/W 50 nm multilayers and then comment on size (layer thickness) dependent radiation hardening. During hardness measurement, the maximum indentation depth is set to 250nm to avoid substrate effect.

After ion irradiation, only the upper 600 nm thick films are irradiated (distorted), although the total film thickness is ~ 2 μm. Using a simple rule-of-mixture estimate, the hardness of films may be expressed as:

$$H_{IT} = \frac{1}{3} H_{rad} + \frac{2}{3} H_{matrix} \quad (6.2),$$

where H_{IT} is indentation hardness. Since H_{matrix} remains the same after ion irradiation, the variation of indentation hardness, ΔH_{IT}, is ~ 4.5 GPa (3 times of experimental hardness increase, 1.5 GPa for Fe/W 50nm multilayers).

Two major mechanisms have been proposed [45, 182] to explain radiation hardening: the dispersed barrier hardening, where radiation induced defects (such as vacancy or interstitial clusters) act as barriers to the movement of dislocations, and the source hardening, the increase in stress required to start a dislocation moving on its glide plane. Since the contribution of source hardening is relatively small, we will focus on dispersed barrier hardening model, which describes the flow stress required to sustain plastic deformation. In the case of Fe/W multilayers, radiation induced hardness variations are likely to originate from He bubbles, interstitial loops, He interstitials, and the microstructural evolution of layer interface (such as intermixing).

6.5.2.1 He bubbles

In order to estimate the hardness enhancement by He bubbles, it is necessary to obtain He bubble density. Assuming the thickness of TEM sample is around 100 nm,

from XTEM images at different depth, the density of He bubbles can be obtained and results are shown in Fig. 6.7. The cubic and triangle dots in Fig. 6.7 stand for He bubble density in Fe/W 50 nm and Fe/W 1 nm multilayers respectively, and the dash line and the dash-dot line are used as visual guides. The evolution of bubble density with depth is somewhat consistent with the SRIM prediction of He concentration vs. depth. The average He bubble concentration, N, is similar in both cases, namely $1.1 \times 10^{24}/m^3$ and $0.9 \times 10^{24}/m^3$ in Fe/W 50 nm and Fe/W 1 nm multilayers, respectively.

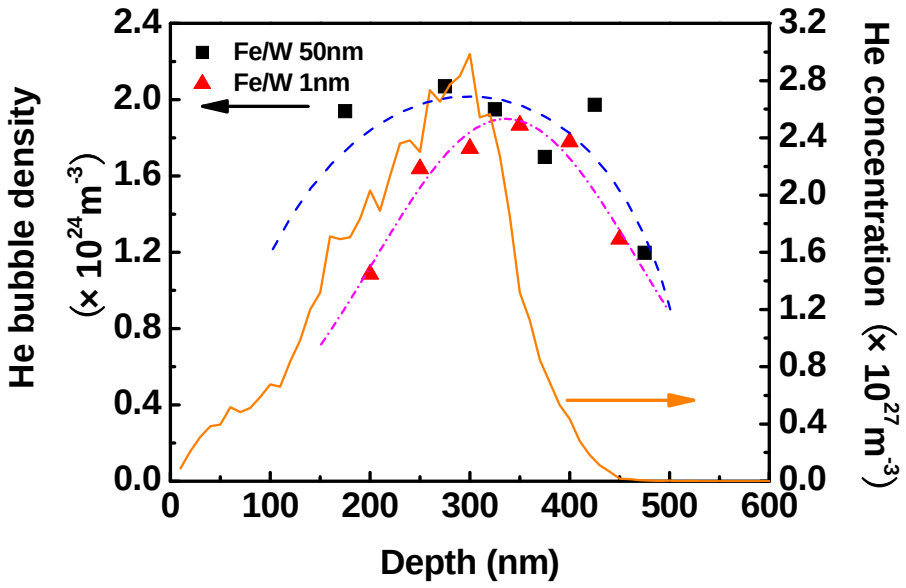

Figure 6.7 He bubble concentration profile vs. depth.

We now attempt to estimate He bubble induced hardening in Fe/W 50nm multilayers. For weak obstacles, such as He bubbles [67, 162, 183, 184], a hardening relationship developed by Friedel-Kroupa-Hirsch (FKH) can be used to describe the dependence of radiation hardening on He bubbles [166, 185, 186]:

$$\Delta\sigma = \frac{1}{8} M \mu b d N^{2/3} \quad (6.3),$$

where M is Taylor factor, 3.05 for BCC metal, μ is the shear modulus, b is the Burgers vector. The increase in yield stress from FKH model is calculated to be ~ 0.13 GPa, corresponding to a hardness increase of 0.4 GPa. Thus radiation hardening due to He bubbles is very small comparing to experimental values.

6.5.2.2 Dislocation loops

Based on a dispersed barrier hardening model [187], the increase in yield stress $\Delta\sigma_y$ is equated to the increase in applied stress required to move a dislocation through a field of obstacles:

$$\Delta\sigma_y = M\alpha\mu b/l = M\alpha\mu b\sqrt{Nd} \quad (6.4),$$

where α is the barrier strength, and l is the average spacing between obstacles, and can be estimated as $1/\sqrt{Nd}$, where N and d is the average loop density and loop diameter, respectively. Considering the typical barrier strength of dislocation loops, α is taken as 0.45 [188, 189]. An experimental determination of loop density is not yet available due to the difficulty of imaging dislocation loops in nanocrystalline metallic multilayers. We

assume that radiation hardening is originated primarily from dislocation loops, and such analysis yields a dislocation loop density of 1×10^{23} m^{-3} and the loop diameter is assume to be around 5 nm. Zinkle and Singh investigated the microstructure of neutron iron and found the defect cluster density and cluster loop diameter increase with increasing dose [190]. When the dose increased from 0.0001 dpa to 0.79 dpa, the loop density increased from 1×10^{21} to 6×10^{22} m^{-3} and the loop diameter increased from 1 nm to 4 nm. In irradiated Fe/W multilayers, the peak damage is ~ 6 dpa, and hence the estimated loop density is higher than that observed in neutron Fe.

6.5.2.3 He interstitials

Although some He atoms have been combined with vacancy to form He bubbles in the multilayer films, there are still a large number of isolated He atoms or He cluster in the system. Atomic simulations [191] show that at low temperature, He interstitials in the vicinity of a dislocation can easily migrate to the dislocation core, and thus resist the glide of dislocations. The binding energy of He to dislocation line is around 2 eV [191]. From Fig. 6.7, the average He concentration is calculated to be around $1\times10^{27}m^{-3}$, much higher than He atoms reside within He bubbles. Previous studies have shown that high concentration of He interstitials will lead to hardening especially when He concentration approaches a critical value, ~ 1 at% [162, 177, 178], or a critical dose of > 1 dpa. However quantitative analysis of He interstitial induced hardening is difficult given the

difficulty of determining He concentration within lattices.

Given the estimation of small radiation hardening from He bubbles and the difficulty in measuring dislocation loop density, the interpretation of radiation hardening mechanisms in Fe/W 50 nm multilayers is complicated. Nonetheless, radiation hardening may originate mainly from dislocation loops and partially from He bubbles and interstitials.

Hardness of irradiated Fe/W 1nm multilayers barely changes, very different from radiation induced hardening in films with $h \geq 5$ nm. XTEM studies show that in peak damage zone the layered structure cannot be resolved in through-focus images of Fe/W 1 nm multilayer presumably due to radiation induced intermixing. It is known that peak strength of as-deposited nanolayer films are determined by interface barrier strength to the transmission of single dislocations [101]. The loss of layer interface may degrade the hardness of multilayers. Such an effect may counteract radiation induced hardening. Finally a noticeable reduction of Hall-Petch slope after radiation indicates a less dependence of hardening on layer thickness as a result of abundance of radiation induced defects in multilayers. Details will be discussed elsewhere.

6.6 Conclusions

The present studies reveal that after He ion irradiation to a dose of $6\times10^{16}/cm^2$, a large number of He bubbles were observed in both Fe and W, and peak He bubble

density occurs at a similar location compared to the peak lattice distortion of Fe (110) and W (110). Radiation induces hardening in multilayers when $h \geq 5$ nm specimens. At such length scales, analyses indicate that radiation induced hardening may originate mainly from dislocation loops and only partially from He bubbles. Hardness barely changes in irradiated Fe/W 1 nm specimens as a result of diminishing discreteness of layer interfaces due to intermixing.

CHAPTER VII

HE ION IRRADIATION TOLERANCE PROPERTIES OF CU/MO INTERFACE – INTERFACE EFFECT ON THE FORMATION OF BUBBLES IN HE ION IRRADIATED CU/MO MULTILAYERS

7.1 Overview

The evolution of microstructure of sputter-deposited Cu/Mo 5 nm multilayers with immiscible interface has been investigated after helium (He) ion irradiations. The immiscible Cu/Mo interface with Kurdjumov-Sachs orientation relation possesses a much higher He solubility than bulk lattices. A large number of He bubbles align along interface in regions with higher He/vacancy ratio, whereas in regions with identical He concentration but a lower He/vacancy ratio, He bubbles distribute uniformly throughout the layers. A threshold He concentration, ~ 0.4 at.%, is identified, below which He bubbles are not detectable in the multilayer. At the peak damage region, the greater diameter of He bubbles in Cu than Mo originates from the ease of bubble growth via a dislocation loop punching mechanism.

7.2 Introduction

High rate of production of helium (He) is one major problem for the integrity of the structural materials under neutron radiations [5, 192]. Because of low He solubility in metals [177, 193], He atoms tend to combine with radiation induced vacancy clusters to

form He bubbles or voids [194 - 199]. These defects together with dislocation loops can significantly degrade mechanical properties [45, 142], in form of embrittlement, typically accompanied by radiation hardening. Interfaces can act as effective sinks to absorb radiation induced defects and He atoms because of a much lower defect formation energy at interfaces than inside bulk lattices [18, 102], Meanwhile certain type of interfaces, such as Cu/Nb, can adopt several mutable atomic structures with nearly degenerate energies, stimulating the delocalization of point defect within interface, and consequently promote the annihilation of vacancies and interstitials [19]. Recent studies show that immiscible Cu/Nb multilayers are extremely resistant against He irradiation [144]. Cu/Nb interface maintains morphological stability of the composites during radiation, suppresses bubble nucleation and restrains the growth of He bubbles at elevated temperatures [200], and also serves as fast diffusion pathways for the removal of implanted He from multilayers [201]. When individual layer thickness decreases to 2.5 nm, He bubbles are barely detectable in irradiated Cu/Nb multilayers [143, 145], indicating a significantly higher He solubility at interface.

Previous studies show that multilayer interfaces with negative heat of mixing tend to intermix during radiation [146, 202], and chemical and morphological stability of interfaces are necessary for continuous absorption and annihilation of radiation induced point defects [145]. Although molecular dynamics (MD) simulation studies have

suggested clear differences in defect production for different type of interfaces [203], experimental evidence on the roles of different type of interfaces and density of interface dislocations on He ion irradiation tolerance remains scarce. In this letter, we investigate He ion radiation damage in Cu/Mo 5 nm multilayers. Cu/Mo interface is selected because of its greater positive heat of mixing, 18 J/mol [80], than that of Cu/Nb, 3 J/mol [80]. The influences of interface, and He and vacancy concentration on the formation and distribution of He bubbles are also discussed.

7.3 Experimental

Cu/Mo multilayer films with individual layer thickness of 5 nm were synthesized on HF etched Si (100) substrates by using the DC magnetron sputtering technique at room temperature. The vacuum chamber was evacuated to a base pressure less than 5×10^{-8} torr prior to deposition. The total film thickness is ~ 1.2 μm. After deposition, films were implanted at room temperature with 100 keV He^{+} ions to a dose of $6\times10^{20}/m^{2}$. The beam current is approximately 6 microamperes, and the temperature rise of the sample stage is ~ 50^{o}C during implantation. Transmission electron microscopy (TEM) and scanning transmission electron microscopy (STEM) experiments were performed on JEOL 3000F and FEI Tecnai G2 F30 microscopes, respectively.

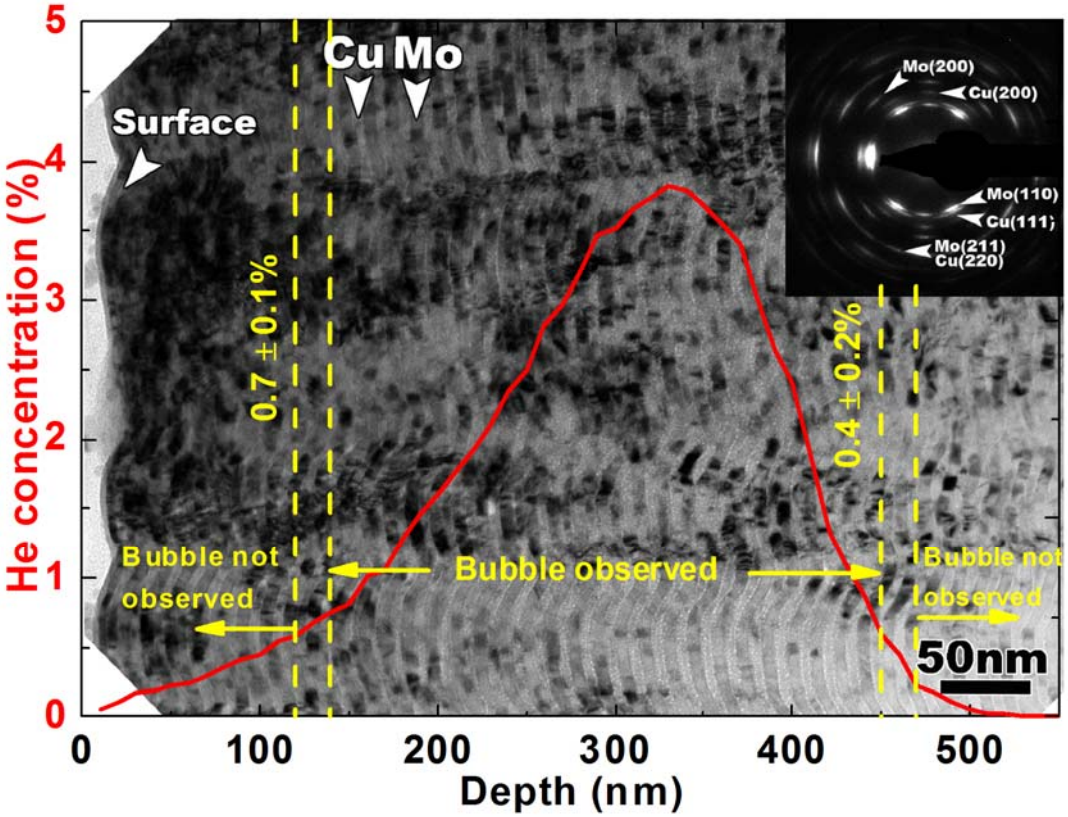

Figure 7.1 Bright field cross-sectional TEM (XTEM) image of ion irradiated Cu/Mo 5 nm. The inserted selected area diffraction pattern (SAD) indicates a strong Cu {111} and Mo {110} fiber texture. The average columnar grain size is 75 nm, much greater than the individual layer thickness. Superimposed on the image is the depth profiles of He concentrations obtained from SRIM simulations. The simulated maximum He concentration is ~ 4 at.% at a depth of ~ 350 nm underneath film surfaces. XTEM images show that the layer interfaces remain distinct after radiation. Minimum He concentration comes to observe He bubble is ~ 0.7 at.% close to the surface and ~ 0.4 at.% at the bottom.

7.4 Results

Cross-sectional TEM (XTEM) image, in Fig. 7.1, reveals the microstructure of irradiated Cu/Mo 5 nm multilayers. The inserted selected area diffraction (SAD) pattern indicates a strong Cu {111} and Mo {110} fiber texture. The average columnar grain size, ~ 75 nm, is much greater than the individual layer thickness. Depth profiles for the implanted He concentration were calculated using the SRIM Monte Carlo code [149] and was superimposed on the XTEM image. The simulated maximum He concentration is ~ 4 at.% at a depth of ~ 350 nm underneath the film surface. The layer interfaces remain distinct throughout the radiated regions. He bubbles were observed within the 130 - 460 nm region underneath the film surface. The He concentration is 0.7±0.1 at.% at ~ 130 nm, and 0.4±0.2 at.% at ~ 460 nm from surface.

Fig. 7.2(a) shows the depth profiles of He concentration (solid curves) and the vacancy density profile (dash line). The peak vacancy density is approximately $4 \times 10^{23} cm^{-3}$ at a depth of ~ 270 nm below. A series of TEM images at different depth underneath the surface, corresponding to the arrows in Fig. 7.2(a), are shown in Fig. 7.2(b) – 7.2(f). At ~ 130 nm from surface, as revealed in Fig. 7.2(b), no He bubbles are detectable in Mo, whereas the density of He bubbles is very low in Cu, with an average diameter of ~ 0.8 nm. At 200 nm underneath the surface, Fig. 7.2(c) shows He bubbles in both Cu and Mo. The density of He bubbles in Cu layer is higher than that shown in

7.2(b), and the average diameters of He bubbles in both Cu and Mo are nearly identical, ~ 0.8 nm. In a high He concentration (~ 3.5 at% He) region d as shown in Fig. 7.2(d), the diameter of He bubbles are greater, ~ 1.5 nm, both inside Cu and along interfaces than that in Mo, where the diameter of He bubbles remains 0.8 nm. Arrows in Fig. 7.2(d) point to several larger He bubbles typically observed along interfaces. In the peak He concentration region, ~ 350 nm below the surface as shown in Fig. 7.2(e), He bubbles along interface continues to grow to over 1.5 nm, and more so into the Cu layer. In a region ~ 420 nm from surface, He bubbles align along interfaces as shown in Fig. 7.2(f). The density of He bubbles inside Cu and Mo layers in region f is much lower than those in region c (Fig. 7.2(c)), even though the He concentration obtained from SRIM calculation is approximately the same in both regions. Typical HRTEM image of an interfacial He bubble in the peak damage region is shown in Fig. 7.3(a) – (c) at different focus condition. It is evident that the geometry of bubbles is non-spherical at interface, and the bubble resides predominantly inside Cu.

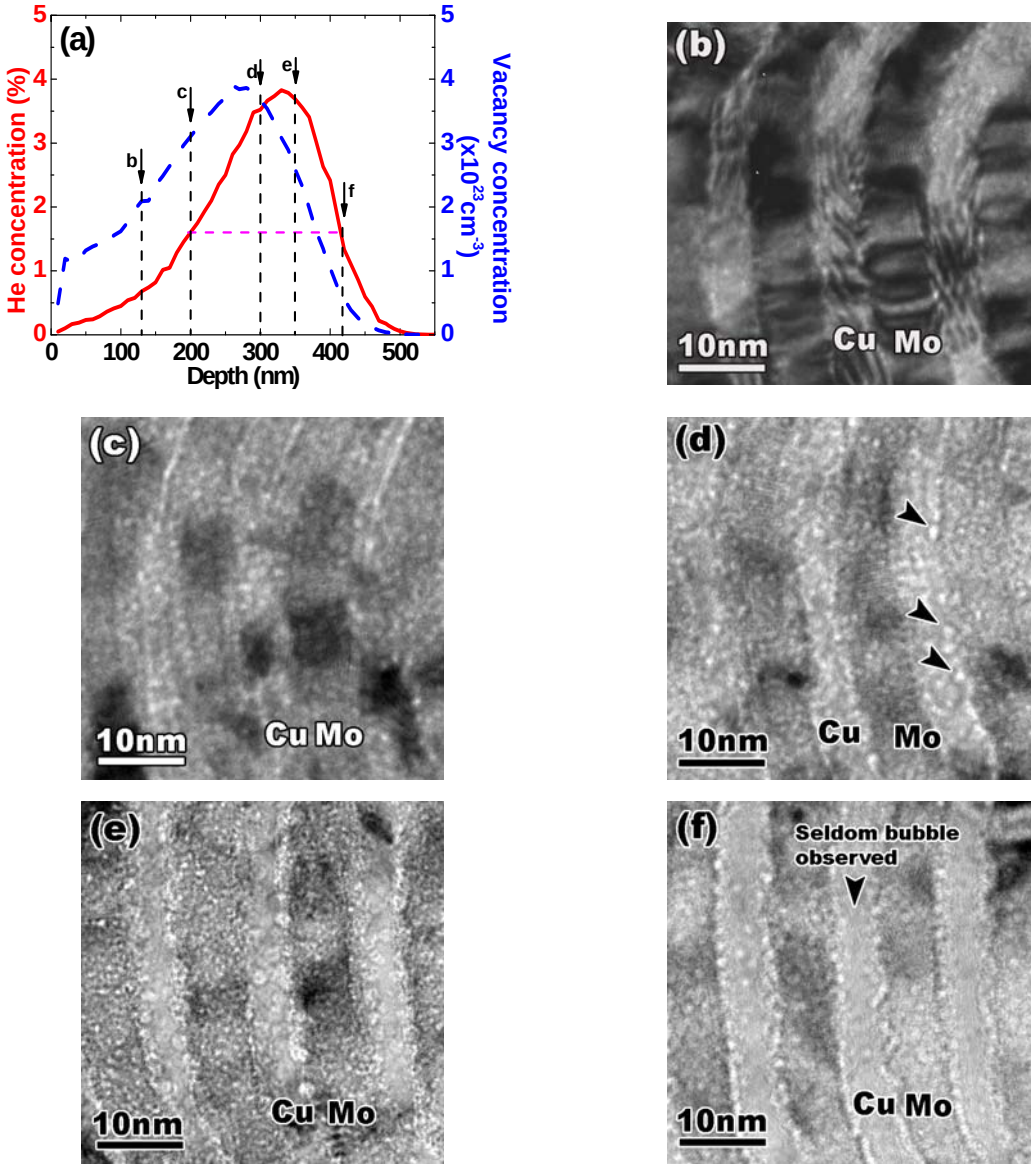

Figure 7.2 (a) The depth profiles of He concentration (solid curves) and the vacancy density profile (dash line). Arrows in (a) mark the position with different depths where corresponding TEM images are shown. (b) Bubbles only are observed in Cu and at the interface. (c) Bubbles begin to show in Mo layer. (d) Bubbles begin to grow. Enlarged He bubbles are marked by the arrow. (e) Bubble density reaches the peak value. The bubbles at interface are tangent at the interface and inside Cu layer. (f) Most of He bubbles are aligned along the interface, with a lower density of He bubbles within both Cu and Mo layers.

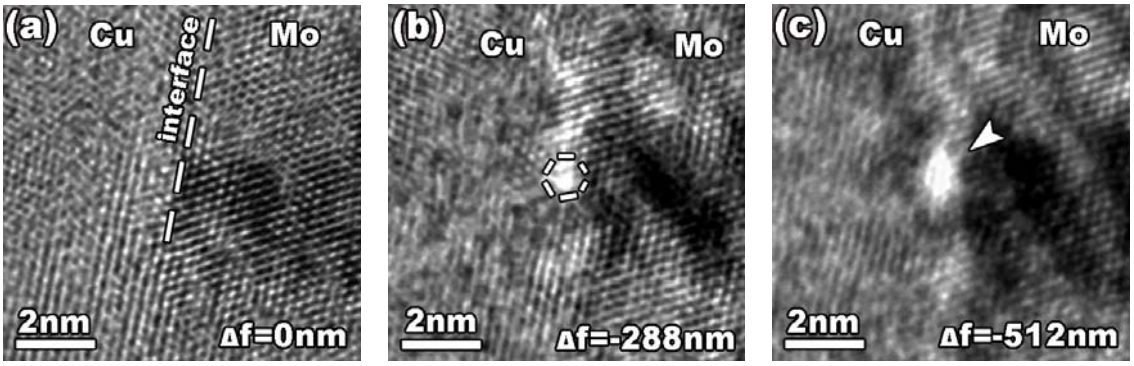

Figure 7.3 (a) - (c) HRTEM image of the same position at different focus conditions. (a) At in-focus condition Cu/Mo interface are resolved. (b) An under-focus (Δf=-288nm) image reveals a white dot at layer interface. (c) At further under-focus (Δf=-512nm) condition, an arrow shows the position of He bubble, which is tangent at the interface and inside Cu layer.

STEM studies with 0.23nm resolution in image mode and energy dispersive x-ray (EDX) analysis with a 2 nm probe size were performed to examine the integrity of layer interfaces after radiation, and results are shown in Fig. 7.4. The layer interfaces are clearly distinguishable throughout the entire irradiated region. Three different regions were examined: near the film surface, peak damage region and a region with little damage (~ 460 nm below surface), as shown in Fig. 7.4(b)-(d), respectively. Chemically abrupt layer interfaces were observed in all three regions. The composition profile in the peak damage region appears a bit rougher than the other two regions as a result of increasing disturbance from He bubbles along the interface.

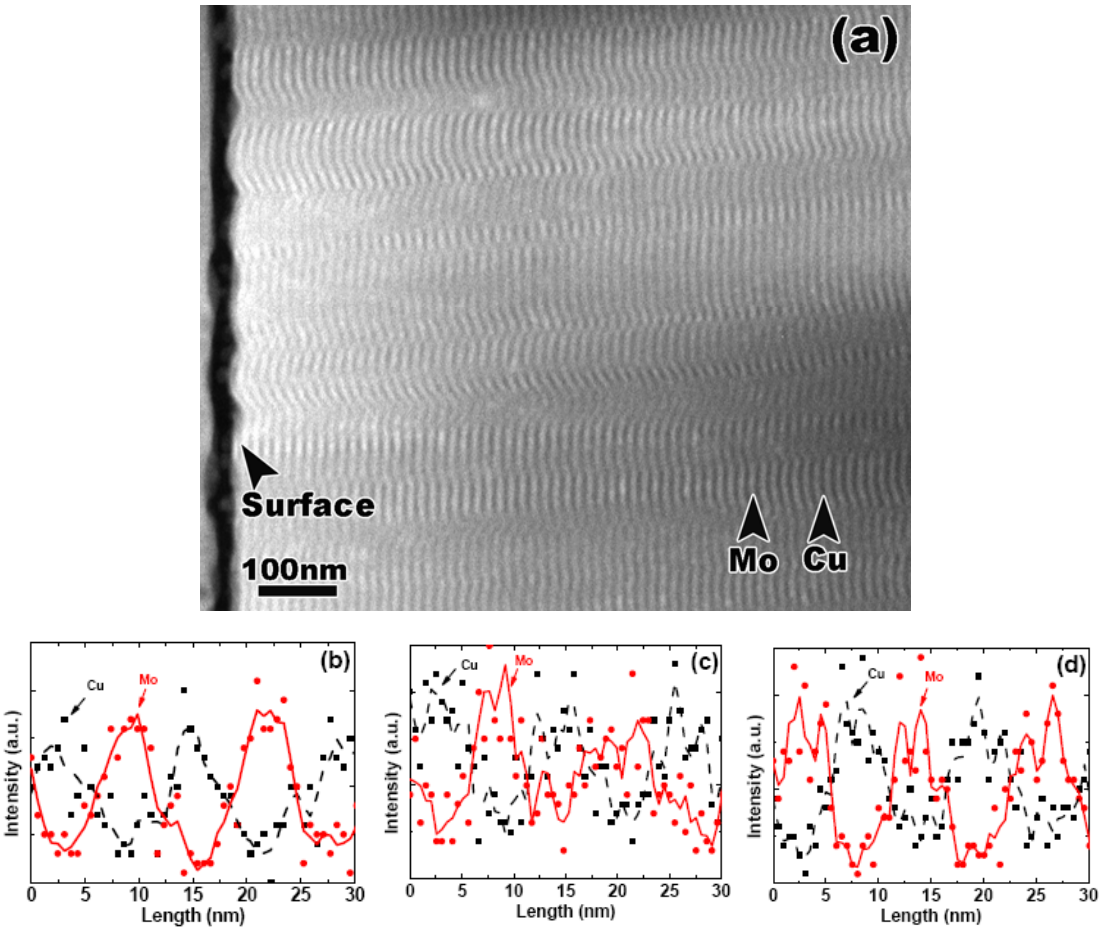

Figure 7.4 (a) Scanning TEM micrographs of irradiated Cu/Mo 5nm multilayers. EDX chemical analyses along a straight line normal to the layer interface at ~ 120 nm below the surface (b), around peak damage region (c), and (d) at in a region with less damage, show that there is an insignificant change in the concentration gradient profile, indicating the retention of layer interface after radiation.

7.5 Discussions

One prominent feature revealed from microscopy studies is the different He bubble distribution in regions of identical He concentration (c and f in Fig. 7.2): ~ 80% of He bubbles at interface in region f, versus uniformly distributed He bubbles in region c. The major reason behind the difference is large difference in vacancy concentration (or different He/vacancy ratio). During radiation the forward momentum imparted to the interstitials causes their penetrations to be deeper than that of vacancies. Therefore an excess vacancy region was formed close to the surface [204]. Region c has a much greater vacancy concentration (or lower He/vacancy ratio) inside the layer than that in f. Hence in region c there is a greater probability for He interstitials to bind with vacancies, significantly reduce the mobility of vacancy clusters [205]. The bubbles may thus form uniformly throughout the layers in this region. However, in region f with a much lower vacancy concentration, He interstitials and vacancies could quickly migrate to the layer interface, where their combinations lead to the formation of bubbles. The same rationale also helps to elucidate the observation of two He concentrations, 0.7±0.1 at.% at ~ 130 nm, and 0.4±0.2 at.% at ~ 460 nm from surface, below which He bubbles are not detected. Close to film surface a higher vacancy concentration consumes more He atoms, hence a higher He concentration is necessary to nucleate He bubbles. Whereas at a much lower vacancy concentration close to the tail of the irradiated region, a lower He

concentration is sufficient to nucleate He bubbles at interfaces. Assume that a majority of the 0.4 at.% He atoms diffuse to the interface and the thickness of the interface is ~ 0.5 nm, the He solubility at Cu/Mo interface is estimated to be 4 at.%, several orders of magnitude larger than those in crystal lattices. For instance the He solubility in Ni found to be 10^{-3} ppm [206].

We now examine the formation of He bubbles along interface. First, the He bubbles along layer interfaces, as shown in Fig. 7.2 (d) and (e) are typically greater than those formed elsewhere. A higher He concentration at layer interface as discussed previously will increase the pressure of He inside the bubbles and in turn promote their coarsening. Similar observation has been reported in polycrystalline metals, where the diameter of bubbles adjacent to grain boundaries is in general greater those in the interior of grains [207]. The fact that bubbles along interfaces reside predominantly inside Cu layer indicates a preferential growth of He bubbles into Cu. At low temperature, bubble growth is typically dominated by the dislocation loop punching mechanism [45, 208]. During radiation the continued increase in He pressure inside the bubble may reach a stress level to activate dislocation sources. The stress required to operate a Frank - Read source is ~ $\mu b/r_0$, where μ is the shear modulus of the solid, b is the Burgers vector of a dislocation, and r_0 is the radius of He bubble. Because μ_{Mo} is much larger than μ_{Cu} (μ_{Mo} = 120 GPa, μ_{Cu} = 46 GPa), the interfacial bubbles are easier to punch dislocation loops into

Cu, and hence grow into the Cu layer. Additionally the higher surface energy of Mo (γ_{Mo} = 3000 mJ/m^2 [209]) than Cu (γ_{Cu} = 1825 mJ/m^2) also prohibits the growth of He bubbles into Mo. The preferential growth of He bubbles into a soft component was not observed in Cu/Nb and Cu/V multilayers irradiated at room temperature [145, 147], presumably because a small disparity between the shear modulus of individual components and relatively higher He solubility.

The He solubility at the Cu/Mo interface is lower comparing to that at Cu/Nb interface, ~ 24 at.% [210]. Such a difference can be explained by a difference in interface dislocation densities. Fig. 7.5(a) is the HRTEM image of a Cu/Mo interface from an un-implanted region. A sharp interface with Kurdjumov-Sachs (K-S) orientation relation is identified, i.e., Cu $(\bar{1}1\bar{1})$ || Mo $(01\bar{1})$ || interface plane, and Cu [110] || Mo [111] in the interface plane. Cu/Nb interface also possesses a K-S configuration [16]. Fig. 7.5(b) and 7.5(c) show the K-S interface configuration of Cu/Mo and Cu/Nb, respectively, examined along a direction normal to the interface plane. Patches, outlined by circles or ellipses, are identified where Cu and Mo (or Cu and Nb) atoms are well aligned along the interface normal direction. Previous MD simulation studies on Cu/Nb interfaces have shown that each patch is typically associated with one interface

dislocation intersection [16, 102]. Furthermore dislocation nodal points whether present in dislocation walls or in grain boundaries would be the most favorable sites for He bubble nucleation [177, 211]. Hence the He solubility shall be proportional to the density of dislocation nodal points. Because of relatively greater lattice mismatch, Cu/Nb interface has a smaller patch area (3.5 nm^2) than that at Cu/Mo interface (6.3 nm^2), and correspondingly a higher patch density. Therefore He solubility is higher at Cu/Nb interface. Obviously, other factors, such as the type of interfaces and the core structure of interface dislocations may also affect the He solubility at interface. These factors are not considered here, but will be investigated in our future studies. Finally, STEM studies show that there is insignificant change in the layer structure and chemistry along interface after He ion irradiation, indicating superior properties of the chemically immiscible Cu/Mo interface in continuously trapping and annihilating radiation induced point defects.

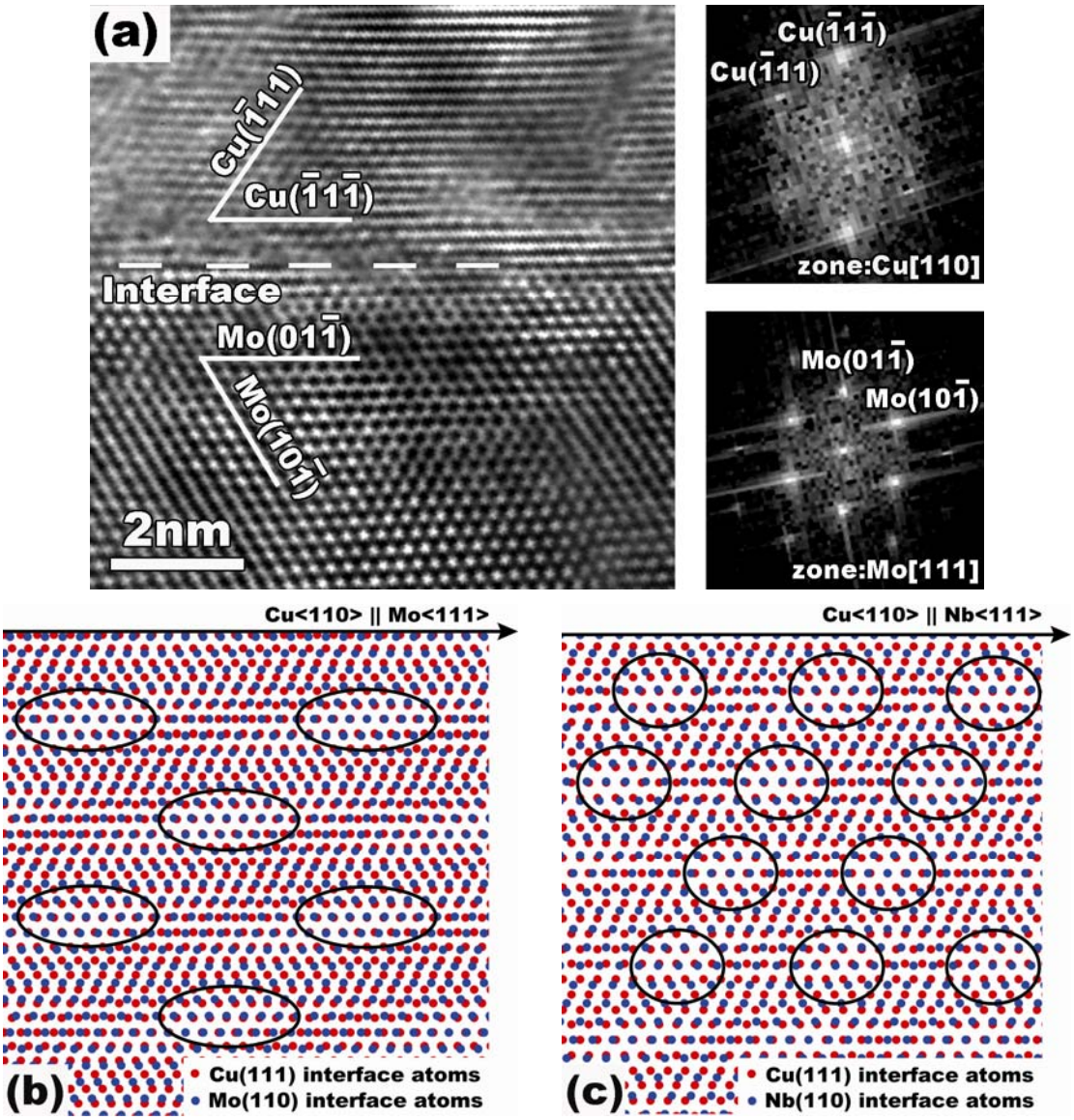

Figure 7.5 (a) HRTEM image of a Cu-Mo interface from an un-implanted region showing sharp interface with indicating that the interface adopts the Kurdjumov-Sachs (KS) orientation relation, corresponding to Cu $(\bar{1}1\bar{1})$ || Mo $(01\bar{1})$ || interface plane, and Cu [110] || Mo [111] in the interface plane. (b), (c) Visualization of the KS interface configuration of Cu-Mo and Cu-Nb, looking normal to the interface plane. Patches which is the proximity of locations where an interface Cu and Mo atom or Cu and Nb atom are positioned nearly 'on top' of each other are identified by circled regions.

7.6 Conclusions

In conclusion, the present studies reveal that Cu/Mo interface has strong capacity to store radiation induced point defects and He interstitials. The formation of He bubbles inside the layers and at interface is determined by He as well as vacancy concentrations. A large modulus difference leads to the preferential growth of interfacial He bubbles into the softer component, Cu, via the dislocation loop punching mechanism. The immiscible K-S type of interface with higher interface dislocation density possesses greater He solubility.

CHAPTER VIII

IN SITU STUDIES OF HE BUBBLE MIGRATION AND GROWTH MECHANISMS IN ION-IRRADIATED SINGLE CRYSTAL CU FILMS

8.1 Overview

We investigated He bubble migration and growth mechanisms in irradiated Cu (100) single crystal films via in situ heating inside transmission electron microscopes. Single crystal Cu films were subjected to helium (He) ion irradiations: 100 keV He^+ ions at a fluence of $6 \times 10^{20}/m^2$. During annealing inside the microscope, the diameters of He bubbles increase continuously from 1 nm at room temperature to tens of nm at ~1030 K. We identify the transition of He bubble growth mechanisms from dislocation loop punching at low temperature to coalescence of bubbles at higher temperature (> 670 K). The activation energy for bubble growth is ~ 0.02 eV for the dislocation loop punching mechanism. At higher temperatures, the activation energy for bubble coalescence is ~ 0.22 eV inside crystal, and 0.34 eV close to surface. The migration mechanisms of He bubbles involve continuous as well as Brownian movement.

8.2 Introduction

In general, the inert gases, particularly helium (He), have low solubility in metals [193]. Radiation of He in metals can induce a large number of point defects as a consequence of nuclear collisions, including vacancies and interstitials, and defect

clusters, such as He bubbles, voids and dislocation loops [135, 136, 212, 213]. Interplay of these defects, especially the existence of a large number of He bubbles, can eventually lead to swelling [214], blistering of metal surfaces [215], and radiation embrittlement [142]. Based on their dimensions, He bubbles can be divided into three groups, small, intermediate and large [136]. When the radius of bubble is small, less than 1 nm, bubbles exist in nucleation stage, and He - metal interactions are very important. However, since bubble size is too small to be unambiguously examined by most experimental techniques, a majority of the work on the nucleation of He bubbles are based on computer simulations [216 - 218]. For the intermediate bubble size, ~ 1 - 100 nm, bubbles are typically named as non-ideal gas bubbles, because the internal pressure is so high that neither the ideal nor the Van der Waals gas law is valid. Mills et al performed extensive studies on the equation of state (EOS) of He at an internal pressure of 0.2 - 2 GPa and a temperature range of 75 - 300 K [219, 220]. When the radius of bubbles exceeds 100 nm, they are referred to as ideal gas bubbles, since the ideal gas law can now be directly applied to describe the internal pressure.

Existing bubbles in as-irradiated materials or bubbles formed at the early stage of annealing tend to coarsen at a constant He content, indicating that their average size increases while their density decreases [177]. With the assistance of in situ heating stage in transmission electron microscope, the movement and diffusion state of He bubbles in

certain elemental metals have been investigated. Brownian motion of He bubbles has been observed in Cu at 0.79 T_m [221], V at 0.55 T_m [222], and Al at 0.88 T_m [223]. Ono et al. [224] also investigated the Brownian motion of He bubbles in Al and they found the diffusivity of He bubbles along grain boundary is much higher than that in lattice. Instead of gliding on the surface, the bubbles in solid Al can move freely as they do in liquids. All that is necessary is a flow of vacancies from one side of the bubble surface to the diametrically opposite surface. Then the whole bubble will move in the direction of the vacancy flux [225].

Although Barnes and Mazey [221] demonstrated the migration and coalescence of He bubbles in Cu, the bubble migration was driven by a temperature gradient imposed by pulse heating which induced an inhomogeneous temperature gradient in specimens. Hence the study on bubble migration and coarsening mechanisms could be compromised. In this paper, we investigate systematically the Brownian motion of He bubbles under isothermal annealing conditions at different temperatures, 300 - 1030 K. We identified the temperature dependent transition of bubble growth mechanism, and derived the characteristic activation energy associated with different growth mechanisms. We also provide some insight in investigating several bubble migration and coalescence events.

8.3 Experimental

A 99.999% pure copper target was sputtered to deposit Cu films on single crystal Si

(100) substrate by using a custom-designed magnetron sputtering system. Prior to deposition, the sputter system was evacuated to a base pressure of 2 - 3 × 10^{-8} torr. The substrates were etched in HF - deionized water solution to remove a thin silicon dioxide layer on the substrate surface. Substrate were neither heated nor cooled during depositions. The total film thickness was kept at ~ 1.6 μm. After deposition, Cu films were implanted at room temperature with 100 keV He^+ ions to a fluence of $6\times10^{20}/m^2$. The beam current is kept at ~ 6 microamperes, and the temperature rise of the sample stage is ~ 50 ^oC during implantation. The microstructure of Cu films was characterized by a Bruker-AXS D8 advanced Bragg-Brentano X-ray diffractometer (XRD). The evolution of microstructures with annealing temperature was examined in situ by using the transmission electron microscopy (TEM) technique and recorded by digital videos through a Gatan CCD camera in a JEOL 2010 transmission electron microscope operated at 200 kV. Isothermal annealing experiments were performed inside the microscope by using an in situ heating stage at selected temperatures, up to 1030 K (0.76 T_m for Cu, where T_m is the melting temperature of Cu, 1084^oC), for ~ 30 min to ensure that the samples reach the desired constant temperatures uniformly.

8.4 Results

8.4.1 The continuous growth of He bubbles up to an annealing temperature of 923 K

XRD studies (not shown here) confirm that single crystal Cu (100) thin films were

synthesized on Si (100) substrates. SRIM simulation based on Monte Carlo method [149] shows that the peak He concentration in the current experiment approaches 2.9 at.% at ~ 370 nm underneath film surface, and the peak damage, approximately 5.7 displacement per atom (DPA), occurs at the similar depth. We examined the radiated Cu from surface to approximately 400 nm underneath. A series of cross-sectional TEM (XTEM) images, as shown in Fig. 8.1, reveal microstructures of radiated single crystal Cu film at different annealing temperatures, varying from 300 to 923 K. At 300 K, the as-irradiated Cu film in Fig. 8.1(a) has a high density of He bubbles, with an average bubble diameter of ~ 1.2 nm. The inserted selected area diffraction pattern (SAD) in Fig. 8.1(a) shows the diffraction from single crystal Cu examined along a <100> zone axis. After in situ annealing at 525 K (0.39 T_m) for 30 min, the diameter of He bubbles increases slightly to ~ 1.8 nm as shown in Fig. 8.1(b). When the annealing temperature increases to ~ 700 K (0.51 T_m), Fig. 8.1(c) shows evident coarsening of He bubbles. The average diameter is ~ 2.5 nm in the peak damage region, wherein region close to the surface, the diameter of He bubbles becomes somewhat larger, ~ 3.5 nm. Significant coarsening was observed after annealing at ~ 923 K as shown in Fig. 8.1(d). Close to surface, the diameters of several bubbles approach or exceed 20 nm, wherein regions away from (underneath) surface, a majority of He bubbles have diameters of ~ 6 nm or less.

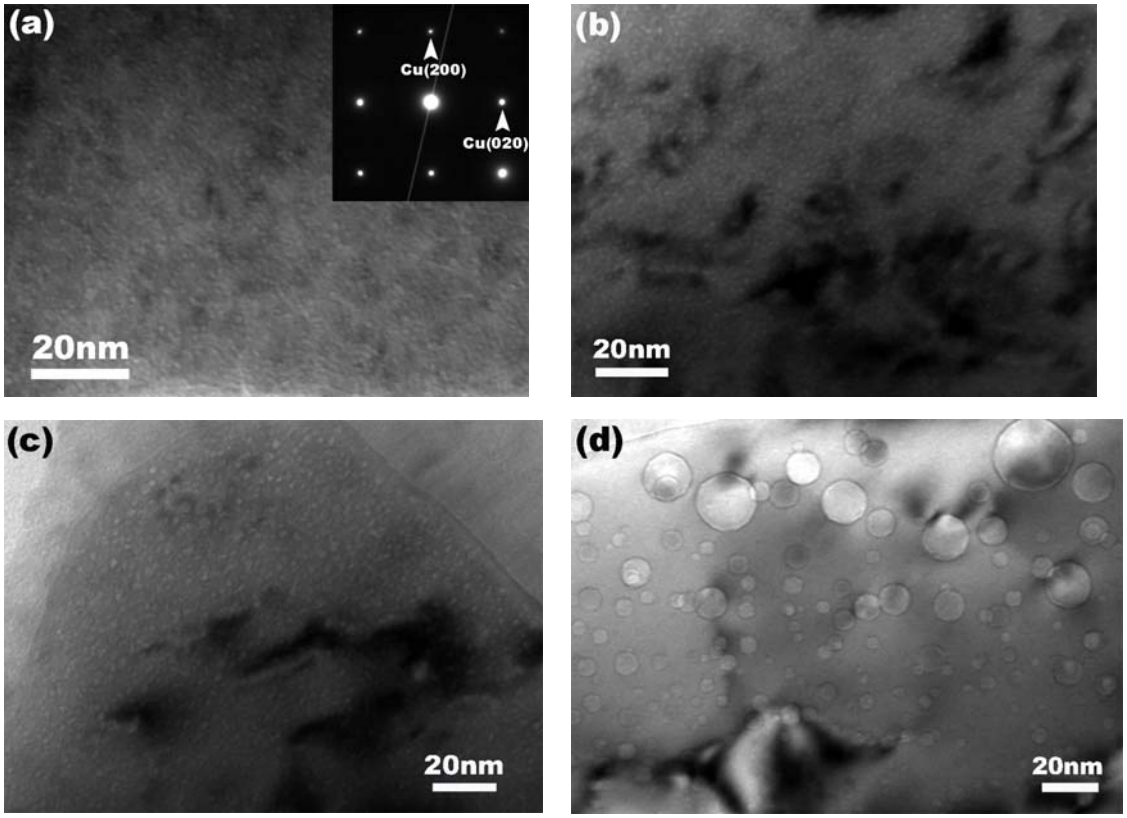

Figure 8.1 Cross-sectional TEM (XTEM) micrographs of as-irradiated and in situ annealed single crystal Cu (100) film examined at different annealing temperatures. (a) The average diameter of He bubbles in the as-irradiated single crystal Cu (100) film, examined at 300 K, is ~ 1.2 nm. The inserted selected area diffraction (SAD) pattern shows the diffraction of single crystal Cu examined along a <100> zone axis. (b) During in situ annealing at 525 K, the diameter of He bubbles increased to ~ 1.8 nm. (c) At the annealing temperature of ~ 700 K, the average size of He bubbles increases to ~ 2.5 nm away from surface, whereas it is ~ 3.5 nm close to the surface. (d) At 923 K, close to the surface, the average diameter of He bubble increases to ~ 11 nm, wherein regions inside the films, the average diameter is ~ 6 nm.

We examined the dependence of bubble diameters on the distance to film surface, and an example is given in Fig. 8.2 for Cu films annealed at 923 K. The XTEM micrograph (Fig. 8.2(a)) shows the existence of He bubbles in a region within 75 nm

from surface. Statistical analysis shows a broad distribution of bubble diameter, 5 - 20 nm, with an average bubble diameter of ~ 12 nm. Fig. 8.2(c) shows a narrower distribution of bubble size and a smaller average diameter of ~ 6 nm, in regions of similar width ~ 75 nm, but further away from surface. Additionally we identify a preferential segregation of He bubbles to dislocations from TEM studies (not shown here), and He bubbles along dislocations have approximately the same diameter comparing to those away from dislocations.

8.4.2 Migration and coalescence of He bubbles at higher annealing temperature (> 930 K)

Our in situ studies show that migration and interaction of He bubbles become more significant at higher annealing temperatures. The following sections show several typical scenarios captured by using a digital video imaging technique.

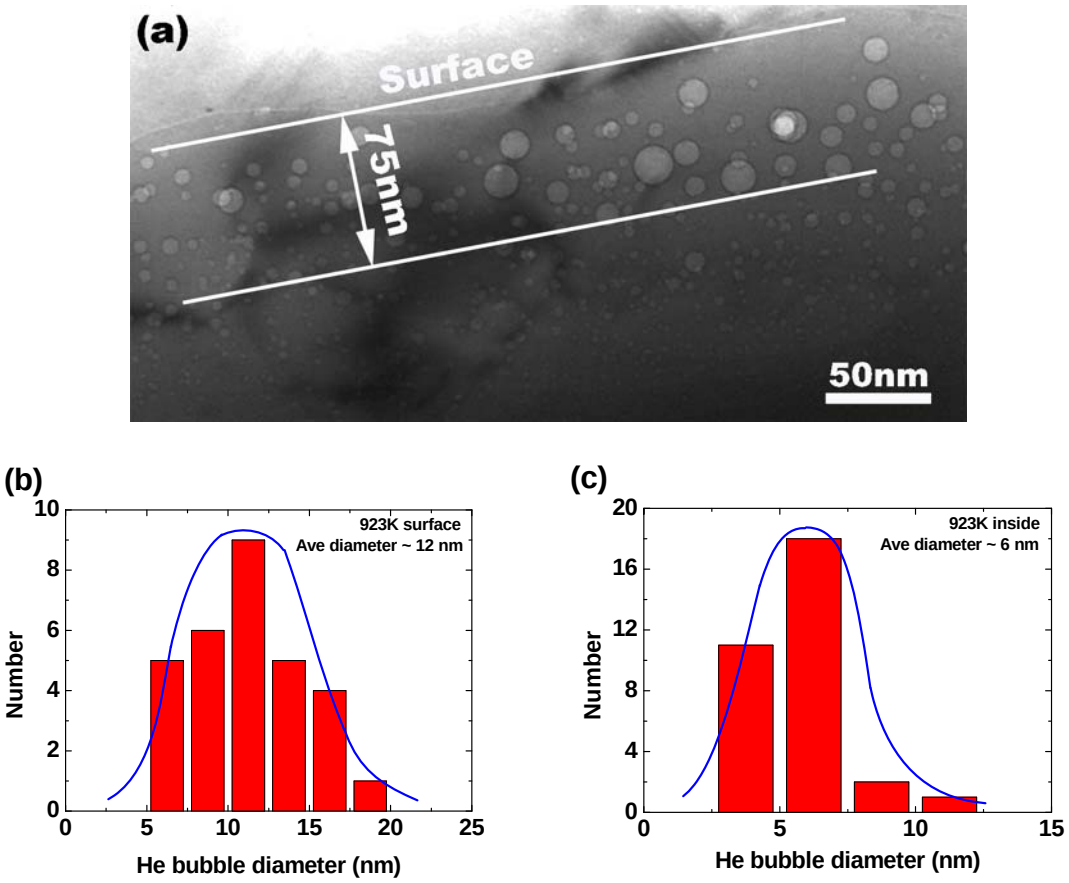

Figure 8.2 (a) XTEM micrograph of the surface region of the irradiated single crystal Cu film recorded at 923 K during annealing. He bubbles with various diameters are observed in this region. (b) and (c) are the corresponding size distribution of He bubbles at 923K close to the surface and inside the films respectively. The average bubble size is ~ 12 nm close to the surface, and ~ 6 nm inside the films.

8.4.2.1 Hopping and coalescence of He bubbles

Fig. 8.3 shows the migration and coalescence of He bubbles at 945 K by extracting a series of images from a digital video. To trace the migration of He bubbles, four bubbles are labeled, 1 through 4, with a diameter of 7.5, 10.8, 11.2 and 14.3 nm respectively as shown in Fig. 8.3(a). In 0.07 s, bubble 2 hopped towards bubble 1 and 3,

as shown in Fig. 8.3(b). The hopping speed is estimated to be 107 nm/s. Meanwhile, bubble 4 escaped out of the Cu foil. The circle in Fig. 8.3(b) indicates the original position of bubble 2. Fig. 8.3(c) shows that after 2.47 s, bubble 1, 2, and 3 merged together instantly to form a new larger bubble, number 5, with a diameter of 14.4.nm.

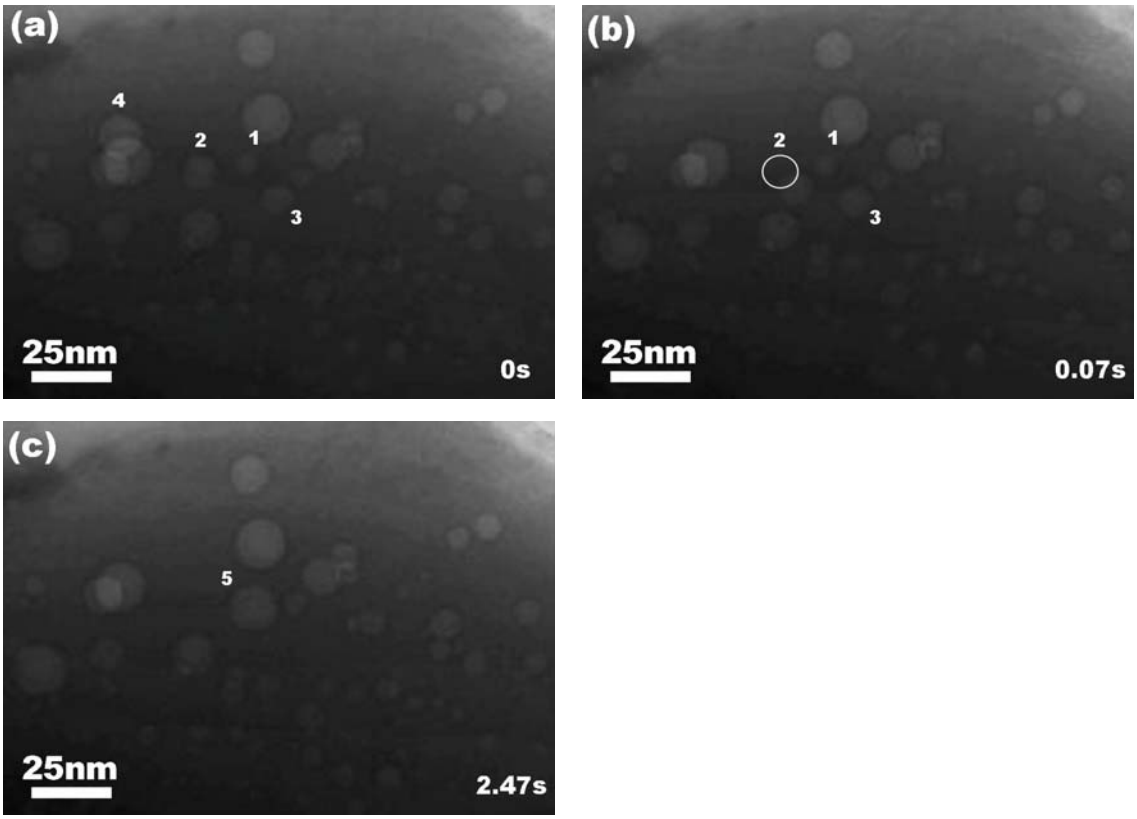

Figure 8.3 A series of XTEM images extracted from a digital video-tape show the migration and coalescence of He bubbles in the Cu film annealed at 945 K. (a) Bubbles of interest are labeled as 1 through 4. The diameters of bubble 1, 2 and 3 are 7.5, 10.8, and 11.2 nm respectively. (b) Bubble 2 hopped towards bubble 1 and 3 at a velocity of ~ 107 nm/s. The circle in (b) outlines the original position of bubble 2 in (a). Also bubble 4 escaped from the Cu film. (c) Bubble 1, 2 and 3 merged simultaneously to form the bubble 5 with a diameter of 11.2 nm.

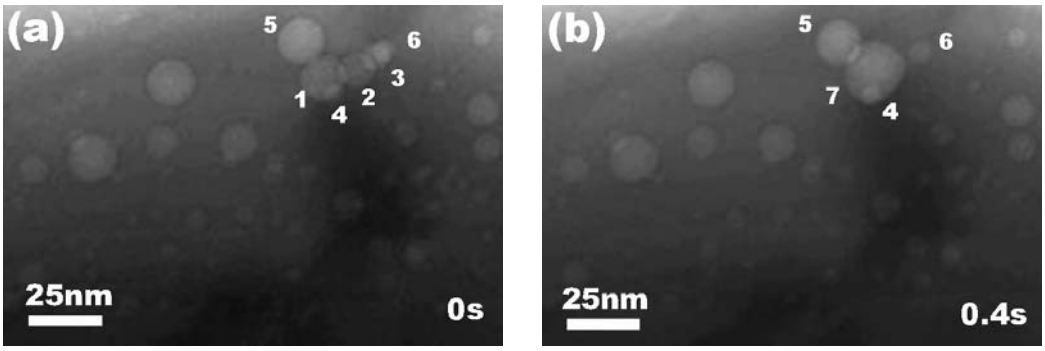

Figure 8.4 XTEM micrographs extracted from the digital video show another coalescence event examined in situ at 981K. (a) A cluster of 6 bubbles are labeled from 1 through 6. The diameters of interested bubbles, 1, 2 and 3, are 16.8, 12.5, 8.9 nm respectively. (2) During annealing, bubble 1, 2 and 3 coalesced into a new bubble, labeled as 7 with a diameter of 21.8 nm. The diameter and location of bubble 4, 5 and 6 remain unchanged during the coalescence.

Fig. 8.4 shows another coalescence event captured at 981K. This coalescence process is slightly different from the previous example as will be discussed later. Before coalescence, 6 bubbles were labeled in the region of interest in Fig. 8.4(a). Particular attentions were paid to three He bubbles, labeled as 1, 2 and 3, with a diameter of 16.8, 12.5, and 8.9 nm respectively. In 0.4 s, the three He bubbles coalesced into one larger bubble, marked as # 7 in Fig. 8.4(b), with a diameter of 21.8 nm. Also the shape of bubble 4 is not exactly spherical.

8.4.2.2 He bubbles′ Brownian motion and migration at higher temperature, ~ 1030 K

The Brownian motion of He bubbles was also recorded, and an example is given in Fig. 8.5(a) – (f), at an annealing temperature of ~ 1030 K. In Fig. 8.5(a), the bubble of interest, # 4, is marked by an arrow, and its diameter is ~ 13.2 nm. Bubble 1, 2 and 3 are references and they did not move during annealing. Fig. 8.5(a)-(e) captures the migration of He bubbles at different times. It is evident that bubble 4 moved back and forth toward bubble 3 a couple of times, but the overall direction of movement is towards the right of the images. Later, bubble 4 moved to a location overlapping with bubble 3 as shown in Fig. 8.5(e), and then escaped from the TEM foil (Fig. 8.5(f)). Fig. 8.5(g) illustrates the history of migration of He bubble 4. Given the overall migration distance of bubble 4 is ~ 18 nm, its average drift velocity is estimated to be ~ 0.08 nm/s.

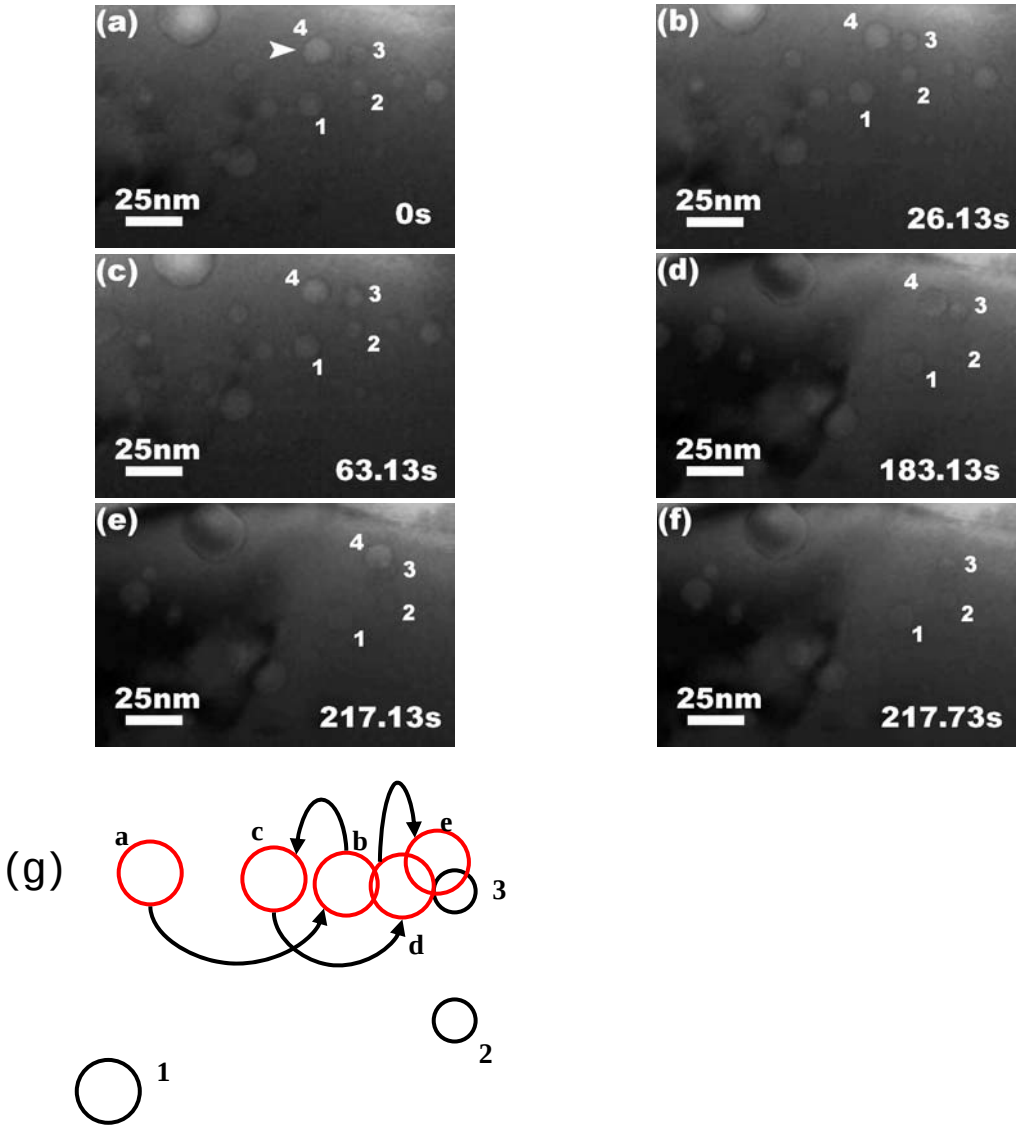

Figure 8.5 A series of snap-shots extracted from a digital video show the Brownian movement of a He bubble during in situ annealing at 1032 K. (a) Bubbles of interest are labeled as 1 through 4. Bubble 4 with a diameter of 13.2 nm, as indicated by an arrow, showed movement in the following snap shots. Bubble 4 moved right towards bubble 3 (b), and then moved backward to almost the original position as shown in (c). Bubble 4 moved towards 3 again (d), and their positions, along the normal direction of the specimen, overlapped as shown in (e). (f) Then almost instantaneously, bubble 4 escaped from the specimen leaving bubble 3 unchanged. (g) A illustration shows the movement history of He bubble 4. Its eventual migration distance is ~ 18 nm, and the drifty velocity of He bubble 4 is estimated to be ~ 0.08 nm/s.

8.5 Discussions

The growth mechanism can be deduced from the temperature dependent evolution of bubble diameters [226]. Fig. 8.6 shows the variation of He bubble diameters, ln D, where D is the diameter of He bubbles, vs. the inverse of annealing temperature, 1/T. At low to intermediate temperatures (300 - 670 K), the diameter of He bubble increases gradually and moderately. The activation energy of bubble growth is estimated by [227, 228]:

$$\ln(D)=\text{const.}-\frac{E_a}{kT} \quad (8.1),$$

where D is the diameter of He bubbles, E_a is the activation energy for bubble growth, (1) and k is the Boltzman's constant.

From the slope of linear fit in the range of 300 - 670K, we derive that the activation energy for bubble growth is ~ 0.02 eV. It has been argued that He bubble can grow through a dislocation loop punching mechanism, especially when the internal pressure of bubble is very high [45]. Bubble growth via dislocation loop punching mechanism has also been observed in He irradiated Mo films, and the authors suspect that such a mechanism could operate over a wide low to intermediate temperature range before vacancy diffusion mechanisms dominate at higher temperature [229]. The peak He concentration in this study is 2.9 at.%, and a large internal pressure due to He is expected especially when the bubble size is ~ 1 nm. Hence our study indicates the bubble growth

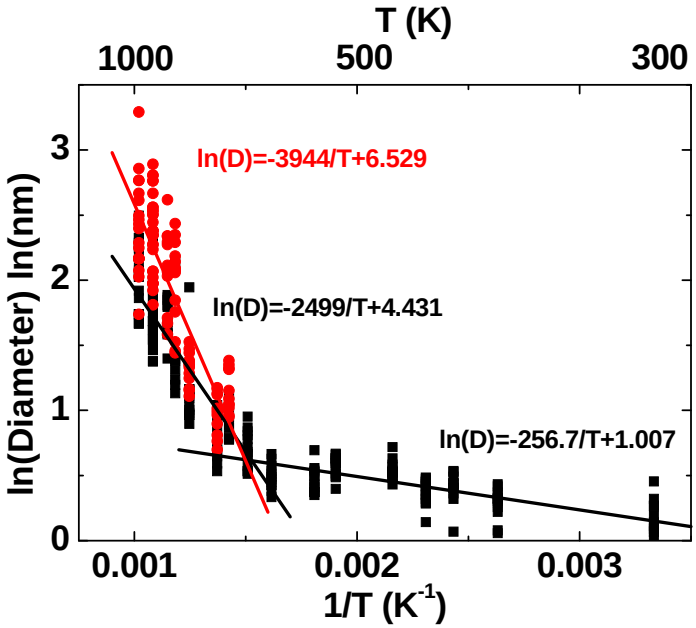

Figure 8.6 Evolution of the diameters, D, of He bubbles at different annealing temperatures is shown in the ln D vs. 1/T plot. The solid squares at higher temperature range indicate the diameter of He bubbles away from the surface region, whereas the solid circles show the diameters of He bubbles in the surface region. The diameters of He bubbles at lower temperature are similar in both regions and so only results taken away from the surface are shown by solid squares. Linear fits of the ln D vs. 1/T were obtained at low and higher temperature regime, and fitting results are shown inside the plot.

is controlled by dislocation loop punching mechanism over the temperature range of 0.22 - 0.5 T_m. Given the high internal pressure inside He bubbles, the activation energy for dislocation loop punching mechanisms in our study is very low, ~ 0.02 eV. Literature on the activation energy for bubble growth via dislocation loop punching mechanisms in fcc metal is scarce, and hence a comparison in general can not be made. At higher annealing temperature, greater than 670 K (≈ 0.5 T_m), the rate of bubble growth

increases significantly. And there is little evidence for the Ostwald ripening process up to 1030 K. At higher annealing temperature, solid squares in Fig. 8.6 show the evolution and distribution of He bubble diameters away from interface, whereas solid circles represent the diameters of He bubbles close to the outer surface of films. The activation energy of bubble growth is estimated to be ~ 0.22 eV away from interface, ~ 0.34 eV in the surface region. Both values are much greater than that at lower temperature. It was reported that the activation energy for bubble coalescence in FCC metal is typically ~ 0.25 eV (0.26 eV for gold - silver alloy, 0.23 eV for Ni) [227, 228]. Hence our study is consistent with those in the literature. The higher activation energy for bubble growth in surface region is likely to due to a reduced vacancy concentration as surface act as sinks for vacancy, whereas the sink density is much lower away from surface (inside lattices) given our Cu films are single crystals. A difference in activation energy for bubble growth close to and away from surface has also been observed elsewhere [228]. Our study reveals a clear transition of bubble coarsening mechanisms from dislocation loop punching at low-to-intermediate temperatures to bubble coalescence at higher temperatures.

Our in situ TEM studies (Fig. 8.3 and 8.4) show two typical examples of bubble coalescence. They appear similar with respect to the morphological evolution of bubbles, which is the coalescence of smaller bubbles into larger one. Furthermore we notice that

the coalescence of He bubbles typically occurs instantaneously and reach a new equilibrium configuration. However, the following analysis will show that there is indeed subtle difference in the two examples of coalescence events.

It has been shown that the stress acting on the surface of a bubble, σ, can be expressed by

$$\sigma = p - \frac{2\gamma_s}{r} \quad (8.2),$$

where p is the pressure of gas inside the bubble, γ_s is the surface energy, and r is the radius of the bubble [45]. Although the internal pressure of He gas could be greater than that of the surface energy term, for simplicity, we assume that the stress acting on the surface of bubbles is negligible during annealing at 945 - 980 K in the current study. The pressure of He at 0 – 300 K can be calculated by using a modified equation of state (EOS) for He. There are numerous discussions on experimental and theoretical calculations of EOS of He [162, 219, 220]. However, experimental determination of EOS at temperatures of current experiment is lacking. To simplify the analysis, we use the ideal gas law to estimate the pressure inside He bubble at the current temperature range, and obtain

$$p = \frac{3xkT}{4\pi r^3} \quad (8.3),$$

where x is the number of He atoms inside bubbles and other variables carry the same meaning as defined before. From Eq. 8.2 and 8.3, we derive that at equilibrium, the

relation between x and the radius of He bubbles is:

$$x = \frac{8\pi r^2 \gamma_s}{3kT} = Ar^2 \quad (8.4),$$

where A is a constant and $A = 8\pi\gamma_s/3kT$. In other words, the number of He atoms per bubble is proportional to r^2. By comparing the diameters of He bubbles involved in coalescence at 945K in Fig. 8.3, we obtain that $r_1^2+r_2^2+r_3^2 > r_5^2$. This implies the total number of He atoms before coalescence is greater than that afterwards at 945 K. He atoms could be redissolved in the crystal lattices. Also we point out that the overall surface energy of the bubbles is reduced after the coalescence. On the other hand, examination of coalescence at 981 K in Fig. 8.4 yields $r_1^2+r_2^2+r_3^2 \approx r_7^2$. Hence the overall He atoms and surface energy of the bubbles are essentially unchanged after the coalescence process. We also notice that the bubble generated by coalescence in Fig. 8.4 is not exactly spherical. As the bubble size gets larger, the pressure inside bubble decreases, and hence influence of crystal orientation on the morphology of bubbles becomes greater. For instance, the bubble growth could be limited by closed pack planes. Hence the magnitude of bubble growth will become anisotropic.

In this study there is little evidence for the Ostwald ripening process. The apparent activation energy of Ostwald ripening of bubbles is typically equal to the energy for He dissociation from bubbles, which is significantly higher than that for migration and coalescence [177]. For instance, the activation energy for Ostwald ripening of bubbles is

1.1 eV in Ni [230], ~ 3.5 eV in 316 stainless steel by experiment and ~ 3.8 eV by theory calculation [226]. However, in our study, the activation energy for migration and coalescence process is much smaller, ~ 0.22 eV, away from surface. Even in the surface region, the activation energy is ~ 0.34 eV. Hence the bubble growth mechanism in the current study appears to be dominated by the dislocation loop punching mechanisms at low-to-intermediate temperature, followed by coalescence at higher temperature.

At higher annealing temperature, we identify somewhat random hopping of He bubbles, similar to Brownian motion [224]. Previous studies show the speed of bubble migration could be very high, ~ 100 nm/s. Furthermore it was shown that bubbles tend to migrate toward certain direction with a driving force of 75 eV/nm due to the pulse heating induced temperature gradient [221]. Our in situ TEM study was performed under isothermal annealing condition for a prolonged period of time to ensure a thermal equilibrium is achieved within the specimens, and hence there is no temperature gradient in specimens. The Brownian movement observed in this study is likely due to the interaction of a He bubble with its neighboring bubbles and could also be driven by localized internal stress in the films. Also we notice that He bubbles typically hop rapidly to certain locations, and rest for an appreciable period of time before the occurrence of a next hopping event.

8.6 Conclusions

Our in situ annealing studies clearly unravel the He bubble growth mechanisms dominated by dislocation loop punching at low temperature, with an activation energy of 0.02 eV, followed by a transition to the bubble coalescence mechanism at higher temperature with much higher activation energy, ~ 0.22 eV away from surface and 0.34 eV close to surface. A variety of bubble migration events are captured in situ, including continuous movement, hopping, and Brownian motion.

CHAPTER IX

SUMMARY AND CONCLUSIONS

I Al/Nb multilayer films with individual layer thickness, h, varying from 1 to 200 nm were synthesized by magnetron sputtering at room temperature. The interface is of fcc/bcc type, with Kurdjumov-Sachs orientation relationship: {111}fcc // {110}bcc; <110>fcc // <111>bcc. I*n situ* nanoindentation studies reveal that (1) interfaces are the strong barriers for dislocation transmission and sinks for absorbing dislocations; and (2) dislocations can climb along the Al/Nb interfaces at a much higher velocity than in bulk lattices, the reason of which is due to a much lower vacancy formation energy at the interface. Such climb event facilitates the annihilation of dislocations along interfaces. These findings imply that Al/Nb interfaces play a crucial role in determining the deformation mechanisms for nanoscale multilayer films. Subject to 100 keV He ion irradiation, when h is greater than 25 nm, hardness of irradiated multilayers barely changes, whereas radiation hardening is more significant at smaller h. Intermetallic compound Nb_3Al has been generated along Al/Nb interface as a consequence of radiation induced intermixing. The composite model suggests that the trend of enhanced radiation hardening at smaller h can be rationalized by the formation of a much harder Nb_3Al intermetallic phase, the volume fraction of which increases at smaller h.

II In parallel, mechanical properties of sputter-deposited Fe/W multilayer films have been investigated. With individual layer thickness greater than 10 nm, Fe/W interface belong to incoherent bcc/bcc type interfaces, and distorted Fe and W crystal structures are observed at smaller individual layer thickness. The significant evolution of XRD profiles at smaller individual layer thickness is simulated well by using the Schuller's model, indicating strong constraints along layer interfaces. HRTEM studies reveal that layer interface in Fe/W 1 nm is semi-coherent with a few misfit dislocations at layer interfaces. Film hardness increases with decreasing h, and approaches a maximum of 12.5 GPa when h = 1 nm. After helium ion irradiation, helium bubbles, 1-2 nm in diameter, were observed inside Fe and W layers, and more so along layer interfaces. The magnitude of hardness variation after radiation depends on individual layer thickness. Radiation hardening is observed in specimens with individual layer thickness of ≥ 5 nm. At such length scales, analyses indicate that radiation hardening may originate from dislocation loops as well as helium bubbles. Hardness barely changes in irradiated Fe/W 1 nm specimens as a result of diminishing discreteness of layer interfaces due to intermixing.

III The evolution of microstructure of sputter-deposited Cu/Mo 5 nm multilayers with immiscible interface has also been investigated after helium ion irradiations. The immiscible Cu/Mo interface with Kurdjumov-Sachs orientation relation has strong

capacity to store radiation induced point defects and He interstitials. A large number of helium bubbles align along interface in regions with higher helium/vacancy ratio, whereas in regions with identical helium concentration but a lower helium/vacancy ratio, helium bubbles distribute uniformly throughout the layers. This study indicates that immiscible fcc/bcc interfaces can effectively reduce the concentration of radiation induced point defects. With the same Kurdjumov-Sachs orientation relation, interface with higher interface dislocation density possesses greater helium solubility.

IV Our in situ annealing studies in irradiated Cu (100) single crystal films clearly unravel the He bubble growth mechanisms dominated by dislocation loop punching at low temperature, with an activation energy of 0.02 eV, followed by a transition to the bubble coalescence mechanism at higher temperature with much higher activation energy, ~ 0.22 eV away from surface and 0.34 eV close to surface. A variety of bubble migration events are captured in situ, including continuous movement, hopping, and Brownian motion.

REFERENCES

[1] M.N. Baibich, J.M. Broto, A. Fert, F.N. Vandau, F. Petroff, P. Eitenne, G. Creuzet, A. Friederich, J. Chazelas, Phys. Rev. Lett. 61 (1988) 2472.

[2] K.P. Jayadevan, T.Y. Tseng, J. Mater. Sci. Mater. Electron. 13 (2002) 439.

[3] F. Hertlein, A. Oehr, C. Hoffmann, C. Michaelsen, J. Wiesmann, Part. Syst. Charact. 22 (2005) 378.

[4] B.X. Liu, W.S. Lai, Z.J. Zhang, Adv. Phys. 50 (2001) 367.

[5] BES Workshop Report Basic Research Needs for Advanced Nuclear Energy Systems. www.sciece.doe.gov/bes/reports/files/ANES_rpt.pdf.

[6] K.S. Kumar, H. Van Swygenhoven, S. Suresh, Acta Mater. 51 (2003) 5743.

[7] H. Van Swygenhoven, J.R. Weertman, Mater. Today 9 (2006) 24.

[8] A. Misra, H. Kung, Advd. Engng. Mater. 3 (2001) 217.

[9] A. Misra, J.P. Hirth, H. Kung, Philos. Mag. A 82 (2002) 2935.

[10] G. Kurdjumov, G. Sachs, Z. Phys. 64 (1930) 325.

[11] Z. Nishiyama, Sci. Rep. Res. Insts. Tohoku Univ. 23 (1934) 638.

[12] G. Wasermann, Arch. Eisenhutt Wes. 16 (1933) 647.

[13] W. Pitsch, Philos. Mag. 4 (1959) 577.

[14] E.C. Bain, Trans. Metall. Soc. A.I.M.E., 70 (1924) 25.

[15] M.J. Demkowicz, J. Wang, R.G. Hoagland, Dislocations in Solids, J.P. Hirth (Ed.)

Elsevier/North-Holland, Amsterdam, 2008, Vol. 14.

[16] M.J. Demkowicz, R.G. Hoagland, J. Nucl. Mater. 372 (2008) 45.

[17] W. Bollmann, Crystal Defects and Crystalline Interfaces, Springer-Verlag, New York, Heidelberg, Berlin, 1970.

[18] J.P. Hirth, J. Lothe, Theory of Dislocations, Wiley, New York, 1982.

[19] M.J. Demkowicz, R.G. Hoagland, J.P. Hirth, Phys. Rev. Lett. 100 (2008) 136102.

[20] A. Misra, M. Verdier, Y.C. Lu, H. Kung, T. E. Mitchell, M. Nastasi, J. D. Embury, Scripta Mater. 39 (1998) 555.

[21] J. McKeown, A. Misra, H. Kung, R.G. Hoagland, M. Nastasi, Scripta Mater. 46 (2002) 593.

[22] X. Zhang, A. Misra, H. Wang, T.D. Shen, M. Nastasi, T.E. Mitchell, J.P. Hirth, R.G. Hoagland, J.D. Embury, Acta Mater. 52 (2004) 995.

[23] S.P. Wen, R.L. Zong, F. Zeng, Y Gao, F. Pan, Acta Mater. 55 (2007) 345.

[24] B.J. Daniels, W.D. Nix, B.M. Clemens, Thin Solid Films 253 (1994) 218.

[25] R.R. Oberle, R.C. Cammarata, Scripta Metal. Mater. 32 (1995) 583.

[26] B.M. Clemens, H. Kung, S.A. Barnett, Mater. Res. Soc. Bull. 24 (1999) 20.

[27] H. Geisler, K.O. Schweitz, J. Chevallier, J. Bottiger, K. Samwer, Philos. Mag. A 79 (1999) 485.

[28] H. Huang, F. Spaepen, Acta Mater. 48 (2000) 3261.

[29] S.L. Lehoczky, J. Appl. Phys. 49 (1978) 5479.

[30] S.P. Baker, W.K. Nix, J. Mater. Res. 9 (1994) 3131.

[31] S.A. Barnett, M. Shinn, A. Rev. Mater. Sci. 24 (1994) 481.

[32] G.S. Was, T. Foecke, Thin Solid Films 286 (1996) 1.

[33] A. Misra, M.J. Demkowicz, J. Wang, R.G. Hoagland, JOM, 2008 April, 39.

[34] A. Misra, J.P. Hirth, R.G. Hoagland, Acta Mater. 53 (2005) 4817.

[35] M.A. Phillips, B.M. Clemens, W.D. Nix, Acta Mater. 51 (2003) 3157.

[36] J.D. Embury, J.P. Hirth, Acta Metall. Mater. 42 (1994) 2051.

[37] P.M. Anderson, T. Foecke, P.M. Hazzledine, MRS Bull. 24 (1999) 27.

[38] J.S. Koehler, Phys. Rev. B 2 (1970) 547.

[39] B.J. Daniels, W.D. Nix, B.M. Clemens, Mater. Res. Soc. Symp. Proc. 343 (1994) 549.

[40] R.G. Hoagland, R.J. Kurtz, C.H. Henager Jr., Scripta Mater. 50 (2004) 775.

[41] J. Wang, R.G. Hoagland, J.P. Hirth, and A. Misra, Acta Mater. 56 (2008) 3109.

[42] J. Wang, R.G. Hoagland, J.P. Hirth, A. Misra, Acta Mater. 56 (2008) 5685.

[43] J. Wang, R.G. Hoagland, A. Misra, Scripta Mater. 60 (2009) 1067.

[44] X. Chu, S.A. Barnett, J. Appl. Phys. 77 (1995) 4403.

[45] G. Was, Fundamentals of Radiation Materials Science, Springer, New York, 2007.

[46] L.R. Greenwood, J. Nucl. Mater. 216 (1994) 29.

[47] D.R. Olander, Fundamental Aspects of Nuclear Reactor Fuel Elements National Technical Information Service, Springfield, VA, 1976.

[48] W.E. King, K.L. Merkle, M. Meshii, J. Nucl. Mater. 117 (1983) 12.

[49] G.H. Kinchin, R.S. Pease, Rept. Prog. Phys. 18, 1.

[50] D.A. Thompson, Radiation Effects and Defects in Solids 56 (1981) 105.

[51] M. Nastasi, J.W. Mayer, J.K. Hirvonen, Ion-Solid Interactions: Fundamentals and Applications. Cambridge University Press, New York. 1996.

[52] J.A. Brinkman, Am. J. Phys. 24 (1956) 246.

[53] J.A. Brinkman, J. Appl. Phys. 25 (1954) 961.

[54] R. Schäublin, Z. Yao, N. Baluc, M. Victoria, Philos. Mag. 85 (2005) 769.

[55] Y. Dai, M. Victoria, Acta Mater. 45 (1997) 3495.

[56] Y. Matsukawa, Y.N. Osetsky, R.E. Stoller, S.J. Zinkle, Philos. Mag. 88 (2008) 581.

[57] M.L. Jenkins, Philos. Mag. 29 (1974) 813.

[58] S.J. Zinkle, L.L. Snead, J. Nucl. Mater. 225 (1995) 123.

[59] B.N. Singh, A. Horsewell, P. Toft, D.J. Edwards, J. Nucl. Mater. 224 (1995) 131.

[60] Y. Shimomura, R. Nishiguchi, Radiation Effects and Defects in Solids, 141 (1997) 311.

[61] T.D. Allen, Lecture of course NEEP 541, University of Wisconsin - Madison.

[62] R. Schaublin, Z. Yao, N. Baluc, M. Victoria, Philos. Mag. 85, (2005) 769.

[63] B.N. Singh, T. Leffers, Radiation effects 101 (1987) 73.

[64] J. Silcox, P. B. Hirsch, Phil. Mag. 4 (1959) 72.

[65] D.S. Gelles, in: Dislocation Modeling of Physical Systems, Ashby et al. (Eds.) Pergamon, New York, 1981.

[66] P.J. Maziasz, ORNL-6121, Oak Ridge National Laboratory (1985).

[67] G.E. Lucas, J. Nucl. Mater. 206 (1993) 287.

[68] G. Odette, J. Nucl. Mater. 85-86 (1979) 533.

[69] A.K. Seeger, On the Theory of Radiation Damage, Radiation Hardening, in: Proceedings of the Second United Nations International Conference on the Peaceful Uses of Atomic Energy, Geneva, United Nations, New York, 1958.

[70] J.J. Holmes, R.E. Robbins, J.L. Brimhall, B. Mastel, Acta Metall. 16 (1968) 955.

[71] G.L. Kulcinski, B. Mastel, H.E. Kissinger, Acta Metall. 19 (1972) 27.

[72] G.R. Odette, D. Frey, J. Nucl. Mater. 85-86 (1979) 817.

[73] F. Gamer, M. Hamilton, N. Panayotou, G. Johnson, J. Nucl. Mater. 103-104 (1981) 803.

[74] M. Grossbeck, P. Maziasz, A. Rowcliffe, J. Nucl. Mater. 191-194 (1992) 808.

[75] N. Yoshida, J. Nucl. Mater. 174 (1990) 220.

[76] A.L. Bement, Rev. Roum. Phys. 17(3) (1972) 361.

[77] G.I. Taylor, Proc. Roy. Sot. 145 (1934) 362.

[78] M. Victoria, N. Baluc, C. Bailat, Y. Dai, M.I. Luppo, R. Shaublin, B.N. Singh, J. Nucl. Mat. 276 (2000) 114.

[79] J. Wang, R.G. Hoagland, A. Misra, Appl. Phys. Lett. 94 (2009) 131910.

[80] F.R. de Boer, R. Boom, W.C.M. Mattens, A.R. Miedema, A.K. Niessen, Cohesion in Metal: Transition Metal Alloys, North Holland, Amsterdam, 1989.

[81] Y. Huang, Z. Xue, H. Gao, W.D. Nix, Z.C. Xia, J. Mater. Res. 15 (2000) 1786.

[82] N. Panich, Y. Sun, Surf. Coat Technol. 182 (2004) 34.

[83] ISO 14577-12002, Metallic Materials - Instrumented Indentation Test for Hardness and Materials Parameters, International Standard.

[84] D.B. Williams, C. B. Carter, Transmission Electron Microscopy, Plenum Press, New York.

[85] M.L. Jenkins, M.A. Kirk, Characterization of Radiation Damage by Transmission Electron Microscopy, Institute of Physics Publishing, Bristol, UK, 2001.

[86] W. Jager, M. Wilkens, Phys. Status Solidi. A 32 (1975) 89.

[87] C. Brown, in: Proceedings of EMAG 75, J.A. Venables (Ed.) Academic Press, New York, 1976, p 405.

[88] E.E. Fullerton, I.K. Schuller, Phys. Rev. B 45 (1992) 9292.

[89] I.K. Schuller, Phys. Rev. Lett. 44 (1980) 1597.

[90] M.D. Graef, M.E. McHenry, Structure of Materials: An Introduction to Crystallography, Diffraction and Symmetry, Cambridge University Press, New York, 2007.

[91] S.P. Baker, N. Burnham, MRS Fall Meeting Tutorial Program, Symposium Q: Fundamentals of Nanoindentation and Nanotribology, Dec. 2000, Boston MA.

[92] S.I. Bulychev, V.P. Alekhin, Zavodskaya Laboratoriya 53 (1987) 76.

[93] M.F. Doerner, W.D. Nix, J. Mater. Res. 1 (1986) 601.

[94] W.C. Oliver, G.M. Pharr, J. Mater. Res. 7 (1992) 1564.

[95] J.B. Pethica, W.C. Oliver, Physica Scripta T19 (1987) 61.

[96] T.J. Bell, M.V. Swain, Thin Solid Films, 220 (1992) 289.

[97] G. Shafirstein, Mater. Res. Soc. Symp. Proc. 356 (1995) 717.

[98] S.P. Baker, T.W. Barbee Jr, W.D. Nix, Mater. Res. Soc. Symp. Proc. 239 (1992) 319.

[99] W.D. Nix, H. Gao, J. Mech. Phys. Solids, 46 (1998) 411.

[100] A.P. Sutton, R.W. Balluffi, Interfaces in Crystalline Materials, Oxford University Press, U.K., 1995.

[101] R.G. Hoagland, J.P. Hirth, A. Misra, Philos. Mag. 86 (2006) 3537.

[102] J. Wang, J.P. Hirth, C.N. Tome, Acta Mater. 57 (2009) 5521.

[103] P. M. Derlet, P. Gumbsch, R. G. Hoagland, J. Li, D. L. McDowel, H. Van Swygenhoven, J. Wang, MRS Bull. 34 (2009) 184.

[104] J.Y. Huang, F. Ding, B.I. Yakobson, Phys. Rev. B 78 (2008) 155436.

[105] M.J. Mills, P. Stadelmann, Philos. Mag. A 60 (1989) 355.

[106] V.V. Bulatov, O. Richmond, M.V. Glazov, Acta Mater. 47 (1999) 3501.

[107] V. Yamakov, D. Wolf, M. Salazar, S.R. Phillpot, H. Gleiter, Acta Mater. 49 (2001) 2713.

[108] J. Wang, H. Huang, Appl. Phys. Lett. 85 (2004) 5983.

[109] X.Z. Liao, F. Zhou, E.J. Lavernia, S.G. Srinivasan, M.I. Baskes, D.W. He, Y.T. Zhu, Appl. Phys. Lett. 83 (2003) 632.

[110] X.Z. Liao, F. Zhou, E.J. Lavernia, D.W. He, Y.T. Zhu, Appl. Phys. Lett. 83 (2003) 5062.

[111] X.Z. Liao, S.G. Srinivasan, Y.H. Zhao, M.I. Baskes, Y.T. Zhu, F. Zhou, E.J. Lavernia, H.F. Xu, Appl. Phys. Lett. 84 (2004) 3564.

[112] V. Yamakov, D. Wolf, S.R. Phillpot, A.K. Mukherjee, H. Gleiter, Nature Mater. 1 (2002) 45.

[113] D. Caillard, Acta Metall. 32 (1984) 1483.

[114] W.D. Nix, R. Gasca-Neri, J.P. Hirth, Philos. Mag. 23 (1971) 1339.

[115] R.W. Balluffi, Phys. Stat. Sol. 31 (1969) 443.

[116] P. Shewmon, Diffusion in Solids, McGraw-Hill Book Co., New York, 1963.

[117] A.F. Jankowski, Nanostructured Mater. 6 (1995) 179.

[118] G. Li, J. Xu, L. Zhang, L. Wu, M. Gu, J. Vac. Sci. Technol. B, 19(1) (2001) 94.

[119] E. O. Hall, Proc. Phys. Soc. London Sect. B 64 (1951) 747.

[120] N. J. Petch, J. Iron Steel Inst. 173 (1953) 25.

[121] T. Foecke, D.S. Lashmore, Scripta Metall. Mater. 27 (1992) 651.

[122] S.I. Rao, P.M. Hazzledine, Philos. Mag, A 80(9) (2000) 2011.

[123] J.E. Krzanowski, Scripta Metall. 25 (1991) 1465.

[124] J.E. Krzanowski, Mat. Res. Soc. Symp. Proc. 239 (1992) 509.

[125] C.A. Volkert, J. Appl. Phys. 70 (1991) 3521.

[126] X. Zhang, A. Misra, J. Appl. Phys. 96 (2004) 7173.

[127] G.G. Stoney, Proc. R. Soc. London A, 82 (1909) 172.

[128] W.A. Bassett, E. Huang, Science 238 (1987) 780.

[129] V. Iota, J.P. Klepeis, C.S. Yoo, J. Lang, D. Haskel, G. Srajer, Appl. Phys. Lett. 90 (2007) 042505.

[130] K.E. Meyer, G.P. Felcher, S.K. Sinha, Ivan K. Schuller, J. Appl. Phys. 52 (11) (1981) 6608.

[131] Marc De Graef, Introduction to Conventional Transmission Electron Microscopy, Cambridge University Press, New York, 2003.

[132] R.E. Stoller, S.J. Zinkle, J. Nucl. Mater. 283-287 (2000) 349.

[133] J.G. Sevillano, in: Plastic Deformation and Fracture of Materials, H. Mughrabi (Ed.) Materials Science and Technology- A Comprehensive Treatment, Vol. 6, VCH, New York, 1993.

[134] F. Carsughi, H. Ullmaier, H. Trinkaus, W. Kesternich, V. Zell, J. Nucl. Mater. 212-1 (A) (1994) 336.

[135] H. Trinkaus, W.G. Wolfer, J. Nucl. Mater. 122 (1984) 522.

[136] H. Trinkaus, Rad. Eff. 78 (1983) 189.

[137] J.F. Stubbins, J. Nucl. Mater. 141-143 Vol.2 (1986) 748.

[138] T.R. Allen, J.I. Cole, in: Institution of Chemical Engineers Symposium Series, A. Kenik (Ed.), Hemisphere Pub Press, New York, no. 148, 2000.

[139] T. Schober, R. Lasser, C. Dieker, H. Trinkaus, J. Less-Common Met. 131 (1987) 293.

[140] H. Evans, A.V. Veen, L.M. Caspers, Scripta Metall. 15 (1981) 323.

[141] K. Morishita, T. Inoue, N. Yoshida, J. Nucl. Mater. 266 (1999) 997.

[142] H. Trinkaus, H. Ullmaier, J. Nucl. Mater. 212-1 (A) (1994) 303.

[143] X. Zhang, Nan Li, O. Anderoglu, H. Wang, J.G. Swadener, T. Hochbauer, A. Misra, R.G. Hoagland, Nucl. Meth. Phys. Res. B 261 (2007) 1129.

[144] T. Hochbauer, A. Misra, K. Hattar, R.G. Hoagland, J. Appl. Phys. 98 (2005)

123516.

[145] A. Misra, M.J. Demkowicz, X. Zhang, R.G. Hoagland, JOM 59 (2007) 62.

[146] N. Li, E.G. Fu, H. Wang, J.J. Carter, L. Shao, S.A. Maloy, X. Zhang, J. Nucl. Mater. 389 (2009) 233.

[147] E.G. Fu, J. Carter, G. Swadener, A. Misra, L. Shao, H. Wang, X. Zhang, J. Nucl. Mater. 385 (2009) 629.

[148] E.G. Fu, N. Li, A. Misra, R.G. Hoagland, H. Wang, X. Zhang, Mater. Sci. Eng. A, 493 (2008) 283.

[149] J.F. Ziegler, M.D. Ziegler, J.P. Biersack, The Stopping and Range of Ions in Solids, Pergamon, New York, 1985.

[150] K. Barmak, C. Michaelsen, S. Vivekanand, F. Ma, Philo. Mag. A, 77 (1998) 167.

[151] T.B. Massalski, J.L. Murray, L. H. Bennett, H. Baker, Binary Alloy Phase Diagrams, ASM International (OH) Publish, New York, 1990.

[152] K. Barmak, K.R. Coffey, D.A. Rudman, J. Appl. Phys. 67 (1990) 7313.

[153] K.R. Coffey, K. Barmak, D.A. Rudman, J. Appl. Phys. 72 (1992) 1341.

[154] L.S. Hung, M. Nastasi, J. Gyulai, J.W. Mayer, Appl Phys. Lett. 42 (1983) 672.

[155] M. Nastasi, J.W. Mayer, Materials Science Reports 6 (1991) 1.

[156] M. Nastasi, L.S. Hung, J.W. Mayer, Appl. Phys. Lett. 43 (1983) 831.

[157] X. Zhang, H. Wang, M. Kassem, J. Narayan, C. C. Koch, J. Mater. Res. 16 (2001)

3485.

[158] U. Himmler, H. Peisl, A. Sepp, W. Waidelich, H. Wenzl, Z. Angew. Phys. 23 (1967) 8.

[159] H. Wagner, F. Dworschak, W. Schilling, Phys. Rev. B 2 (1970) 3856.

[160] W. Donitz, W. Hertz, W. Waidelich, H. Peisl, K. Boning, Phys. Stat. Sol. 22 (1974) 501.

[161] S.I. Rao, C. R. Houska, K. Grabowski, G. Ice, C. J. Sparks, J. Appl. Phys. 69 (1991) 8104.

[162] H. Trinkaus, J. Nucl. Mater. 38 (2003) 234.

[163] G.R. Odette, D. Frey, J. Nucl. Mater. 85-86 (1979) 817.

[164] A.L. Bemment, in: Proceedings of the 2nd International Conference on the Strength of Metal and Alloys, ASM, Metals Park, OH, 1973.

[165] S.J. Zinkle, Y. Matsukawa, J. Nucl. Mater. 329-333 (2004) 88.

[166] J. Friedel, Dislocations, Pergamon, New York, 1964.

[167] F. Kroupa, P.B. Hirsch, Disc. Faraday Soc. 38 (1964) 49.

[168] A.K. Seeger, Phys. Lett. 8 (1964) 296.

[169] D. Rodney, G. Martin, Phys. Rev. Lett. 82 (1999) 3272.

[170] M. Grossbeck, P. Maziasz, A. Rowcliffe, J. Nucl. Mater. 191-194 (1992) 808.

[171] F. Garner, M. Hamilton, N. Panayotou, G. Johnson, J. Nucl. Mater. 103-104

(1981) 803.

[172] M. J. Caturla, N. Soneda, E. Alonso, B. D. Wirth, T. Díaz de la Rubia, J. M. Perlado, J. Nucl. Mater. 276 (2000) 13.

[173] D. Chung, M. Enoki, T. Kishi, Sci. Tech. Adv. Mater. 3 (2002) 129.

[174] J.G. Sevillano, Acta Metal. 34 (1986) 1473.

[175] F. Carsughi, H. Ullmaier, H. Trinkaus, W. Kesternich, V. Zell, J. Nucl. Mater. 212-1 (A) (1994) 336.

[176] E.V. Kornelsen, A.A. Van Gorkum, J. Nucl. Mater. 92 (1980) 79.

[177] H. Trinkaus, B.N. Singh, J. Nucl. Mater. 323 (2003) 229.

[178] J.D. Hunn, E.H. Lee, T.S. Byun, L.K. Mansur, J. Nucl. Mater. 282 (2000) 131.

[179] H.L. Heinisch, F. Gao, R.J. Kurtz, J. Nucl. Mater. 329-333 (2004) 924.

[180] R. Popescu, H.L. Meyerheim, D. Sander, J. Kirschner, Phys. Rev. B 68 (2003) 155421.

[181] P.A. Thorsen, J.B. Bilde-Sorensen, B.N. Singh, Scripta Mater. 51 (2004) 557.

[182] D. Rodney, G. Martin, Phys. Rev. Lett. 82 (1999) 3272.

[183] G.R. Odette, D. Frey, J. Nucl. Mater. 85-86 (1979) 817.

[184] D.G. Franklin, G.E. Lucas, A.L. Bement, Creep of Zirconium Alloys in Nuclear Reactors, ASM, Metals Park, OH, 1983.

[185] S.J. Zinkle, Y. Matsukawa, J. Nucl. Mater. 329-333 (2004) 88.

[186] F. Kroupa, P.B. Hirsch, Disc. Faraday Soc. 38 (1964) 49.

[187] A.S. Argon, Strengthening Mechanisms in Crystal Phasticity, Oxford University Press, New York, 2008.

[188] M. Grossbeck, P. Maziasz, A. Rowcliffe, J. Nucl. Mater. 191-194 (1992) 708.

[189] F. Garner, M. Hamilton, N. Panayotou, G. Johnson, J. Nucl. Mater. 103-104 (1981) 803.

[190] S.J. Zinkle, B.N. Singh, J. Nucl. Mater. 351 (2006) 269.

[191] H.L. Heinisch, F. Gao, R.J. Kurtz, E.A. Le, J. Nucl. Mater. 351 (2006) 141.

[192] A.J.E. Foreman, B.N. Singh, J. Nucl. Mater. 133-134 (1985) 451.

[193] A.A. Lucas, Physica B&C 127 (1984) 225.

[194] H. Ullmaier, Nucl. Fusion 24 (1984) 1039.

[195] S.J. Zinkle, B.N. Singh, J. Nucl. Mater. 199 (1993) 173.

[196] W.J. Phythian, R.E. Stoller, A.J.E. Foreman, A.F. Calder, D.J. Bacon, J. Nucl. Mater. 223 (1995) 245.

[197] F. A. Garner, B. Oliver, L.R. Greenwood, M.R. James, P.D. Ferguson, S.A. Maloy, W.F. Sommer, J. Nucl. Mater. 296 (2001) 66.

[198] B.M. Oliver, M.R. James, F.A. Garner, S.A. Maloy, J. Nucl. Mater. 307 (2002) 1471.

[199] I.I. Chernov, A.N. Kalashnikov, B.A. Kalin, S. Yu. Binyukova, J. Nucl. Mater.

323 (2003) 341.

[200] K. Hattar, M.J. Demkowicz, A. Misra, I.M. Robertson, R.G. Hoagland, Scr. Mater. 58 (2008) 541.

[201] M.J. Demkowicz, Y.Q. Wang, R.G. Hoagland, O. Anderoglu, Nucl. Meth. Phys. Res. B 261 (2007) 524.

[202] N. Li, M.S. Martin, O. Anderoglu, A. Misra, L. Shao, H. Wang, X. Zhang, J. Appl. Phys. 105 (2009) 123522.

[203] H.L. Heinisch, F. Gao, R.J. Kurtz, J. Nucl. Mater. 329-333 (2004) 924.

[204] L. Shao, X. Lu, X. Wang, I. Rusakova, J. Liu, W. Chu, Appl. Phys. Lett. 78 (2001) 2321.

[205] P.L. Lane, P.J. Goodhew, Philos. Mag. A 48 (1983) 965.

[206] H.J. von den Driesch, P. Jung, High Temp. High Pressures 2 (1980) 635.

[207] P.A. Thorsen, J.B. Bilde-Sørensen, B.N. Singh, Scripta Mater. 51 (2004) 557.

[208] W.G. Wolfer, Philos. Mag. A 58 (1988) 285.

[209] Y.G. Chen, B.X. Liu, J. Alloys Compd. 261 (1997) 217.

[210] M.J. Demkowicz, D. Bhattacharyya, I.O. Usov, A. Misra, Y.Q. Wang, M. Nastasi, in review.

[211] B.N. Singh, T. Leffers, J. Nucl. Mater. 125 (1984) 287.

[212] F. Carsughi, H. Ullmaier, H. Trinkaus, W. Kesternich, V. Zell, J. Nucl. Mater.

212-1 (A) (1994) 336.

[213] A.W. Thompson, Mater. Sci. Eng. 21 (1975) 41.

[214] H. Evans, A. van Veen, L.M. Caspers, Scripta Metall. 15 (1981) 323.

[215] K. Morishita, T. Inoue, N. Yoshida, J. Nucl. Mater. 266 (1999) 997.

[216] W.D. Wilson, M.I. Baskes, C.L. Bisson, Phys. Rev. B 13 (1976) 2470.

[217] W. D. Wilson, C.L. Bisson, M.I. Baskes, Phys. Rev. B 24 (1981) 5616.

[218] W.D. Wilson, Radiation Effects 78 (1983) 11.

[219] R.L. Mills, D. H. Liebenberg, J.C. Bronson, Phys. Rev. B 21 (1980) 5137.

[220] S.E. Donnelly, Radiation Effects 90 (1985) 1.

[221] R.S. Barnes, D. J. Mazey, Proceedings of the Royal Society A, 271, 47 (1963).

[222] S.K. Tyler, P.J. Coodhew, J. Nucl. Mater. 92 (1980) 201.

[223] K. Ono, S. Furuno, K. Hojou, T. Kino, K. Izui, O. Takaoka, N. Kubo, K. Mizuno, K. Ito, J. Nucl. Mater. 191-193 (1992) 1269.

[224] K. Ono, S. Furuno, S. Kanamitu, K. Hojou, Philo. Mag. Lett. 75 (1997) 59.

[225] J. Gittus, Irradiation Effects in Crystalline Solids, Applied Science Publishers LTD, London, 1978.

[226] J. Rothaut, H. Schroeder, H. Ullmaier, Philo. Mag. A 47 (1983) 781.

[227] T. Thome, R. I. Grynszpan, Radiation Effects & Defects in Solids 161 (2006) 347.

[228] V.N. Chernikov, H. Trinkaus, P. Jung, H. Ullmaier, J. Nucl. Mater. 170 (1990) 31.

[229] J.H. Evans, A. van Veen, L.M. Caspers, Scripta Metall. 15 (1981) 323.

[230] V.N. Chernikov, H. Trinkaus, H. Ullmaier, J. Nucl. Mater. 250 (1997) 103.

VITA

Nan Li received his Bachelor of Engineering degree in Materials Science and Engineering from Beijing University of Chemical Technology in 2003. He received his Master of Engineering degree in Materials Science and Engineering from Institute of Metal Research, Chinese Academy of Science in 2005. He entered the Department of Mechanical Engineering at Texas A&M University in Spring 2006 and received his degree of Doctor of Philosophy in May 2010. His research interests include mechanical properties and radiation tolerance of multilayer films.

Mr. Li may be reached at Department of Mechanical Engineering, Materials Science and Engineering Program, 3123 TAMU, College Station, TX 77843-3123. His email is willow07@gmail.com.